Univerzita Karlova v Praze

1. lékařská fakulta

Zobrazovací metody v lékařství



MUDr. Aaron Michael Rulseh

Application of Diffusion Tensor Imaging to Brain Gray and White Matter

Aplikace zobrazení difuzního tenzoru na mozkovou šedou a bílou hmotu

Disertační práce

Školitel: Prof. MUDr. Josef Vymazal, DSc.

Praha, 2013

Prohlášení:

Prohlašuji, že jsem závěrečnou práci zpracoval samostatně a že jsem řádně uvedl a citoval všechny použité prameny a literaturu. Současně prohlašuji, že práce nebyla využita k získání jiného nebo stejného titulu.

Souhlasím s trvalým uložením elektronické verze mé práce v databázi systému meziuniverzitního projektu Theses.cz za účelem soustavné kontroly podobnosti kvalifikačních prací.

V Praze, 15.06.2013

MUDr. Aaron M. Rulseh

© 2013 - MUDr. Aaron Michael Rulseh
All rights reserved.

Application of Diffusion Tensor Imaging to Brain Gray and White Matter

Abstract

In the present work we explore the gray and white matter applicability of diffusion tensor imaging (DTI). To evaluate effect of ferritin-bound iron on gray matter contrast in DTI, we created an *in vitro* model consisting of agarose gel phantoms doped with ferritin, and validated our results *in vivo* on 29 healthy volunteer subjects 19–80 years of age in the basal ganglia. We further explored the application of DTI to amyotrophic lateral sclerosis (ALS) and multiple system atrophy (MSA); neurodegenerative diseases with gray and white matter pathophysiological components. In the ALS study, 33 patients and 30 age- and sex-matched controls were recruited, while the MSA study included 20 probable MSA subjects (10 MSA-P, 10 MSA-C) and 20 age- and sex-matched controls.

We found that ferritin-bound iron may make a significant contribution to DTI scalars in gray matter regions of the brain, mediated by eigenvalue repulsion. This has important implications for DTI studies targeting gray matter regions, especially in adolescence and in diseases associated with altered brain-iron load. In ALS, we found altered diffusion in the corona radiata and callosal body, and changes in R_2 in the caudate nucleus and frontal white matter. In MSA, we observed widespread white matter changes associated with a positive clinical history of cerebellar manifestations, while altered DTI metrics in the putamen were associated with a positive clinical history of parkinsonian manifestations. The diagnostic potential of MRI in MSA may be greatly extended by applying DTI and evaluating changes primarily in the putamen and middle cerebellar peduncle, reaching very high sensitivities and specificities.

Keywords: magnetic resonance imaging, diffusion-weighted imaging, diffusion tensor imaging, multiple system atrophy, amyotrophic lateral sclerosis

Aplikace zobrazení difuzního tenzoru na mozkovou šedou a bílou hmotu

Abstrakt

V předložené práci zkoumáme použití zobrazení difuzního tenzoru (DTI) v mozkové šedé a bílé hmotě. K zhodnocení efektu superparamagnetického či antiferomagnetického železa na DTI kontrast v šedé hmotě jsme vytvořili in vitro model sestávající se z fantomu, vyplněného agarovým gelem s feritinem. Naše výsledky jsme poté zhodnotili na 29 zdravých dobrovolnících (39-80 let věku), a to v oblasti bazálních ganglií. Dále jsme zkoumali aplikace DTI u amyotrofické laterální sklerózy (ALS) a mnohočetné systémové atrofie (MSA), neurodegenerativních chorob, postihujících šedou i bílou hmotu mozkovou. V ALS studii 33 pacientů a 33 zdravých dobrovolníků srovnatelných pohlavím i věkem bylo vyšetřeno, zatímco u MSA bylo zahrnuto 20 pacientů s diagnózou pravěpodobné MSA (10 s MSA-P a 10 s MSA-C) spolu s 20 zdravými dobrovolníky, srovnatelnými pohlavím a věkem.

Zjistili jsme, že železo vázané ve ferritnu signifikantně ovlivňuje skalární veličiny DTI v šedé hmotě mozkové. Tento poznatek má důležitý význam pro DTI studie, zaměřené na oblasti šedé hmoty, a to zvláště u adolescentů a u osob trpícími nemocemi se změnami ukládání železa, jako například Huntingtonova choroba či MSA. U ALS jsme nalezli změněnou difuzi v oblasti corona radiata a těla corporis callosi, a to spolu se změnami v R_2 v caput ncl. caudati a ve frontální bílé hmotě. U MSA jsme pozorovali rozsáhlé změny v bílé hmotě spojené s pozitivním klinickým obrazem mozečkové manifestace, zatímco změněné DTI hodnoty v putamen byly propojeny s pozitivním obrazem parkinsonské manifestace. Diagnostický potenciál magnetické rezonance u MSA může být významně rozšířen aplikací DTI a sledováním změn zvláště v putamen a středním cerebellárním pedunculu, kde tyto změny dosahují vysoké senzitivity a specificity.

Klíčová slova: difúze, DTI, MSA, ALS, železo, šedá hmota, bílá hmota

Contents

1 Introduction **1**

2 Hypotheses and Objectives **19**

3 Materials and Methods **21**

4 Results **36**

5 Discussion **81**

6 Conclusions **90**

Refrences **92**

Appendix A **106**

Appendix B **125**

Listing of figures

1.1 Longitudinal and transversal magnetization 6

3.1 FA vs. *ex vivo* iron concentration in gray matter 22
3.2 Manual ROI placement in basal ganglia 26
3.3 *In vitro* diffusion data 26
3.4 ROI placement in ALS subjects and controls 30
3.5 MSA, qualitative MRI 35

4.1 *In vitro* dependence of R_2 on iron concentration 37
4.2 *In vitro* dependence of 1/SNR on iron concentration 37
4.3 *In vitro* dependence of 1/SNR on R_2 38
4.4 *In vitro*, eigenvalues (λ1–3) as a function of 1/SNR and R_2 . . . 39
4.5 *In vitro* dependence of FA on 1/SNR 39
4.6 *In vitro* dependence of FA on R_2 40
4.7 *In vitro*, MD as a function of 1/SNR and R_2 41
4.8 *In vivo*, linear dependence of 1/SNR and R_2 42
4.9 *In vivo*, eigenvalues as a function of 1/SNR and R_2 42
4.10 *In vivo*, linear dependence of FA on 1/SNR and R_2 43
4.11 *In vivo*, linear dependence of MD on 1/SNR and R_2 43
4.12 *In vivo*, linear dependence of R_2, FA and λ3 on PD 44
4.13 Dependence of DTI metrics on R_2 in the globus pallidus 44
4.14 Dependence of DTI metrics on age in the putamen 45
4.15 TBSS results, ALS 47
4.16 TBSS results, MSA 49

4.16 (continued) 50
4.17 TBSS results, MSA-P 52
4.17 (continued) 53
4.18 TBSS results, MSA-C 54
4.18 (continued) 55
4.19 TBSS results, MSA-C vs. MSA-P 56
4.19 (continued) 57
4.20 TBSS results, cMSA 59
4.20 (continued) 60
4.21 TBSS results, pMSA 61
4.21 (continued) 62
4.22 TBSS results, cMSA vs. pMSA 63
4.22 (continued) 64
4.23 MSA, ROC in left putamen, $\lambda 1$ 67
4.24 MSA, ROC in right putamen, $\lambda 1$ 68
4.25 MSA, ROC in left putamen, $\lambda 3$ 69
4.26 MSA, ROC in right putamen, $\lambda 3$ 70
4.27 MSA, ROC in left putamen, MD 71
4.28 MSA, ROC in right putamen, MD 72
4.29 MSA, ROC in left putamen, RD 73
4.30 MSA, ROC in right putamen, RD 74
4.31 MSA, ROC in the MCP, RD 76
4.32 MSA, ROC in the MCP, MD 77
4.33 MSA, ROC in the MCP, FA 78
4.34 MSA, ROC in the MCP, $\lambda 1$ 79

Acknowledgments

I would like to thank my advisor, Prof. MUDr. Josef Vymazal, DSc., for his guidance, support and encouragement throughout the production of this research and dissertation. I would also like to thank my committee members for their service on my dissertation committee. I am also indebted to many of my colleagues for their assistance and support over the years. And most of all, I would like to thank my family for their support, and especially my son, Joshua, for keeping me focused on the important things in life.

The journey of a thousand miles must begin with a single step.

Lao Tzu

1 Introduction

Magnetic resonance imaging (MRI) has become an invaluable tool in clinical and research medicine. The emergence and rapid development of MRI in recent years has made it competitive with, and in many cases preferable to, many existing invasive and non-invasive imaging technologies. Primarily a neuroradiological tool when first applied clinically, MRI has quickly become the imaging method of choice in many fields, with approximately 60 million MRI scans currently performed worldwide every year [123]. In general, MRI can be applied in the examination of almost all organs and systems. MRI is non-invasive, and since the electromagnetic energy applied in MRI is relatively weak, it carries no radiation burden. Therefore, after almost thirty years of the clinical use, MRI is considered a safe technique.

Historical perspective

Although the history of clinical MR imaging is relatively brief, there is a long evolutionary road leading to where we are today. Isidor Rabi is credited with the first observations of nuclear magnetic resonance (NMR), and was awarded the Nobel prize in physics in 1944 for his development of the atomic and molecular beam magnetic resonance method of observing atomic spectra [112]. Rabi was an Austrian native that worked in the Department of Physics at Columbia University in New York, where he studied the magnetic properties of crystals and atomic nuclei. He succeeded in advancing earlier work by Gerlach and Stern [37], applying electromagnetic oscillations in a magnetic field to determine the magnetic moments of atomic nuclei [98]. Rabi credited C.J. Gorter, a dutch contemporary that visited his lab in 1937, as providing methodological insight that allowed him to measure the nuclear magnetic moment. The term nuclear magnetic resonance is attributed to Rabi, and was publicly introduced in 1942 by C.J. Gorter [40].

The first successful NMR experiments were carried out in 1946 by two scientists working independently; Edward Purcell, working at Harvard University, and Felix Bloch, at Stanford University. They observed that when certain nuclei were placed in a magnetic field they absorbed energy in the electromagnetic spectrum and re-emitted this energy when the nuclei returned to their original state [15, 97]. The magnitude of the magnetic field and the radiofrequency were related according to the Larmor relationship (see Equation 1.1, where ω is precessional frequency (sometimes termed the Larmor frequency), γ is gyromagnetic ratio (a constant for a given nucleus), and B_o is the magnitude of the magnetic field). The Larmor relationship is important as it relates the frequency at which a nucleus will absorb energy, forming the basis of NMR. Purcell and Bloch shared the Nobel Prize in Physics in 1952 for their discovery.

$$\omega = \gamma B_o \tag{1.1}$$

The application of NMR for many years was focused on the analysis of often

microscopic, non-biological samples by small-bore magnets. NMR spectrometers at this time could provide certain information on the chemical characteristics of a sample, but no spatial information was available. Although imaging was not yet possible, some investigators recognized the potential for NMR in application to biology and medicine. In 1955, Erik Odeblad and Gunnar Lindström from Stockholm published the first description of relaxation-time differences in human tissue [87]. This was the first work to show that different tissues have differing relaxation times related to water content and chemical composition. In the following years a number other researchers began to examine biological samples. In 1965, C.B. Bratton reported *in vivo* T_1- and T_2-measurements of frog skeletal muscle [16] and in 1968, Jackson and Langham published the first NMR results obtained from a whole living animal [63]. The relaxation characteristics of human tissue was also explored further, first in skeletal muscle [26, 50, 51] and brain tissue [45].

In the early 1970's a great deal of interest arose in applying NMR to the characterization of pathological tissue. Raymond Damadian is probably the most well-known researcher of the this era that was focused on clinical applications of NMR. Damadian's group at Downstate Medical Center in Brooklyn investigated *ex-vivo* relaxation times of healthy and malignant rat tissue, and reported longer relaxation times in malignant tissue than in healthy tissue [30]. Although Damadian's findings generated a lot of interest in NMR, they were not reproducible by other scientists [59] and eventually came to be regarded as provocative, but of little scientific merit. Nevertheless, Damadian received a patent for his device in 1974, and has vigorously fought throughout his career to be recognized as the founder of MRI.

Magnetic resonance imaging was born in 1971, when Paul C. Lauterbur of the State University of New York at Stony Brook conceived of applying magnetic field gradients in all three dimensions to create NMR images. Two years later, Lauterbur published the first images of two tubes of water in the journal Nature [68] (famously, Nature initially the article because they didn't feel it would be of sufficient interest). Lauterbur called his imaging method zeugmatography, a term supplanted by NMR imaging and eventually MRI (the word "nuclear" was

eventually removed as it could suggest the presence of ionizing radiation to the uninformed). His discovery led the way from one-dimensional spectroscopic imaging to the multi-dimensional MR imaging used today. Concurrent to this work, Sir Peter Mansfield at the Department of Physics at the University of Nottingham independently considered the application of spatially-encoding gradients to allow MR imaging, and provided the mathematical basis for echo planar imaging. In a letter to the editor in 1973, Mansfield and Peter K. Grannell described the use of magnetic field gradients to acquire spatial information in NMR experiments [76]. For their contributions, Lauterbur and Mansfield were jointly awarded the 2003 Nobel Prize in Physiology or Medicine.

Following the initial development of MRI, a flurry of activity in human imaging ensued. In 1975, Mansfield and Andrew A. Maudsley proposed a line technique which, in 1977, led to the first image of *in vivo* human anatomy, a cross section through a finger. In 1977, Waldo Hinshaw, Paul Bottomley, and Neil Holland successfully produced an image of a wrist [55], and Damadian et al. published a cross section of a human chest [31]. The first transverse MR images through a human head were presented in 1978 by Hugh Clow and Ian R. Young, working at the British company EMI, and two years later, William Moore and colleagues presented the first coronal and sagittal images through a human head.

Principles of magnetic resonance imaging

An MRI system works by applying three cooperating magnetic fields to induce and detect subtle changes in the imaging subject: a static magnetic field, gradient magnetic fields, and radio frequency (RF) fields. The static magnetic field (B_0) of an MRI system remains constant and is present at all times, even when no examination is taking place. The magnetic flux density of this field is denoted in Tesla (T; 1T = 10,000 gauss), with most clinical scanners presently in use being 1.5T or 3T (as a comparison, the magnetic flux density of the earth is approximately 50 μT, or 0.5 gauss). The source of this field is a coil, made of a specific alloy that when cooled to a temperature close to absolute zero loses

nearly all electrical resistance. This condition is called superconductivity, and it enables the static magnetic field to remain on at all times, without the requirement of an external electric current. Another advantage of superconductive coils is their ability to provide a very homogeneous field, which is necessary for MR imaging.

Magnetic resonance imaging is proton imaging. Hydrogen nuclei (protons) in different local magnetic environments and conditions are imaged. Protons posses a quantum property termed spin, which is the total angular momentum of its constituent parts, as well as a magnetic dipole moment. When a subject is placed in the B_0 field, the protons (synonymously termed "spins" in MR literature) attempt to align with the B_0 field to minimize free energy. However, the protons are not able to align completely due to quantum forces, and experience torque which results in the precession of their magnetic dipole moments. The usual analogy to help visualize precession is the wobble of a spinning top. The frequency of precession is proportional to the magnetic field magnitude as stated by the Larmor relationship (see Equation 1.1), and is sometimes termed Larmor precession.

Magnet field gradients are provided by the three paired, orthogonal gradient coils, being superimposed on the static (B_0) field. The gradients are applied in short pulses and vary in amplitude, time and direction, allowing slice selection, frequency encoding, and phase encoding. Two critical properties of gradient coils that affect image quality and have important safety implications are the gradient strength and the gradient slew rate. Gradient strength (amplitude) is the change in field strength per unit distance, and is given in mT/m. The gradient slew rate is the rate of ascent or descent of a gradient from zero to its maximum amplitude, and is given in mT/m/msec, or more often in T/m/s.

Radio frequency (RF) pulses are used to excite the protons so that meaningful data can be captured and used for imaging. An RF pulse is a magnetic field oscillating at the Larmor frequency. RF pulses are used to change the spin state of protons precessing at the same frequency by the process termed resonance. The result of this process is a change in energy state of the proton in the same

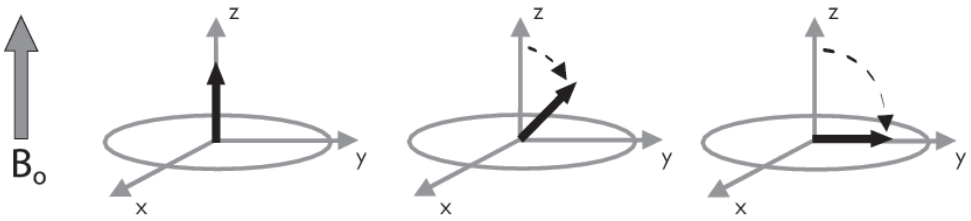


Figure 1.1: Decrease in longitudinal magnetization and concurrent development of transversal magnetization.

direction as the B_0 field (a decrease in longitudinal magnetization), and the development of precessional phase coherence (development of transversal magnetization; see Figure 1.1). Precessional phase coherence results in a vector of magnetization transverse to the B_0 field that, in the absence of phase coherence, is canceled out. Since this vector is not in the same plane as the B_0 field, it is not obscured by the B_0 field and can be detected.

The protons quickly return to a lower energy state after cessation of the RF pulse in a process called relaxation. Transversal relaxation (spin-spin relaxation, T_2 relaxation) results from the loss of precessional phase coherence (dephasing) as protons exchange energy with nearby nuclei. The efficiency by which this occurs is dependent on the local environment, and its interval (T_2 relaxation time, a constant) may be used to create a unique contrast in MR imaging (T_2-weighted images). Longitudinal relaxation (spin-lattice relaxation, T_1 relaxation) is the return of net magnetization to equilibrium along the z-axis (in the same plane as the B_0 field). The efficiency of longitudinal relaxation is also dependent on the local environment, and its interval (T_1 relaxation time, a constant) may also be used to create a unique contrast (T_1-weighted images). Spin-lattice relaxation results in the transfer of thermal energy to the surrounding environment, and is the basis for an important safety consideration, the specific absorption rate (SAR).

MR imaging is remarkable in that it can deliver images with superb soft tissue contrast while exposing the patient to very little risk. In contrast to the stochastic effects of ionizing radiation used in many radiological modalities, e.g., X-ray or

computerized tomography (CT) examinations, the effects of the magnetic fields used in MR systems on biological tissues follow a deterministic model, related to the transfer of thermal energy to tissues due to spin-lattice relaxation. Therefore, the magnitude of the effect is dependent on parameters related to exposure and can be predicted, allowing the establishment of appropriate safety thresholds. SAR is defined as the RF power absorbed per unit mass of an object, measured in watts per kilogram. SAR is dependent on many factors, some of the more salient being the B_0 field magnitude, gradient field characteristics, RF power, characteristics of the pulse sequences employed during the examination, characteristics of the transmitter-coil, and patient mass. In controlling the SAR during an MRI examination, undesirable thermal effects can be minimized and maintained within a safe level.

The response of matter to an applied external field is described by magnetic susceptibility (χ). In the context of MR imaging materials are generally classified as diamagnetic, paramagnetic, superparamagnetic or ferromagnetic. Diamagnetism is present in all materials and is the weakest property of the those listed. When other types of magnetism are not present, diamagnetism is the dominant property and the material is said to be diamagnetic. The electrons in these materials are covalently bound and balanced in magnetic moment. In the presence of an external magnetic field, the orbital motion of electrons is altered, inducing a magnetic field that opposes the applied field. Most biological tissues are diamagnetic. In paramagnetic materials, the magnetic moments of electrons do not balance completely and individual atoms have a permanent dipole moment. In the absence of an external magnetic field, the dipoles do not interact and are randomly orientated, resulting in zero net moment. However, in the presence of an external magnetic field the dipoles align and produce a field in the same direction as the B_0 field. Examples of paramagnetic materials include gadolinium, deoxyhemoglobin and methemoglobin. Paramagnetism is stronger than diamagnetism, and when present in a material it overpowers its inherent diamagnetic properties. Superparamagnetism is intermediate between paramagnetism and ferromagnetism, and is present when the material consists of small crystallites (1–10 nm). Superparamagnetic materials behave similar to

those that are paramagnetic, however, in the presence of an external magnetic field the magnetic moment of the entire crystallite tends to align with the external field (as opposed to the alignment of individual atoms in paramagnetic materials). Examples of superparamagnetic materials include iron oxide particles, ferritin and hemosiderin. Finally, ferromagnetic materials have domains in which the magnetic moments of unpaired electrons align parallel to each other. The domains are arranged in random orientations, but in the presence of an external field the domains become aligned and the material is said to be magnetized. In ferromagnetic materials, all magnetic ions make a positive contribution to net magnetization (compare to ferrimagnetic, where some ions subtract from net magnetization, and antiferromagnetic, where ions anti-align resulting in zero net magnetization). Ferromagnetism is several orders of magnitude stronger than paramagnetism. Iron, cobalt and nickel are typical ferromagnetic materials.

Principles of diffusion imaging

Diffusion is a naturally-occurring process that involves the mass transport or mixing of matter without the requirement of bulk motion. Diffusion may be explained by Fick's first law [36] (see Equation 1.2, where J is the net diffusion flux, D is the diffusion coefficient, ∇ is the gradient operator, and φ is the particle concentration), which states that particles in a medium diffuse along a concentration gradient from more populated to less populated zones, i.e., toward dispersion equilibrium.

$$J = -D\nabla\varphi \tag{1.2}$$

In 1828, Robert Brown published the first (indirect) observations of diffusion [19], as he observed by simple light microscopy the seemingly animate motion of pollen granules suspended in solution. Nearly one-hundred years later, Brown's observations were explained by Einstein [35], who reconciled them with the diffusion principles outlined by Fick. Einstein realized that the motion of pollen granules observed by Brown were due to the underlying thermokinetic energy of water molecules in the solution. This motion of particles due to the random

bombardment of molecules in the surrounding medium is now termed Brownian motion. To explain Brownian motion, Einstein introduced the concept of a displacement distribution, quantifying the fraction of particles that will traverse a certain distance within a particular interval (see Equation 1.3, where $\overline{X^2}$ is the mean-squared displacement, D is the diffusion coefficient and t is the diffusion time). Thus, Brownian displacement of a particle is proportional to the square root of the diffusion time.

$$\overline{X^2} = 2Dt \tag{1.3}$$

Erwin Hahn first proposed that MRI may be sensitive to diffusion in 1950 [43]. Hahn explained T_2 signal attenuation in his original experiment by the loss of phase coherence of spins in an inhomogeneous environment. He suggested that if the external magnetic field were spatially dependent, then molecular diffusion would be apparent. Hahn employed two 90° RF pulses to obtain spin echoes, which was later improved upon by Carr and Purcell [21], who proposed the use of a 90° RF pulse followed by a train of 180° RF pulse echoes. However, in the presence of RF imperfections not all spins experience a perfect 180° pulse and the spins rapidly dephase. This technical problem was overcome by Meiboom and Gill a few years later [79], by applying the 180° pulses with phases shifted in quadrature with respect to the initial 90° RF pulse (the Meiboom-Gill phase condition). This is now known as the Carr-Purcell-Meiboom-Gill (CPMG) sequence. Carr and Purcell further proposed the application of a magnetic field gradient for the purpose of measuring molecular diffusion [21]. They realized that spins subjected to a magnetic field gradient acquire location-dependent phase, with stronger gradients allowing greater phase differences across a sample and, therefore, greater sensitivity to diffusion. Thus, MR signal within the framework proposed by Carr and Purcell is related to molecular diffusion, as the net phase shift of spins is related to the net displacement of spins within the gradient field.

Further advance in diffusion imaging was made by Stejskal and Tanner in 1965 [121], when they introduced the pulsed gradient spin-echo (PGSE) sequence. This concept replaced the constant field gradient introduced by Carr and Purcell

with strong, symmetrically-placed pulsed gradient lobes on either side of the 180° refocusing pulse. This approach overcame the problems related to increased bandwidth and slice-selection inherent in with use of a constant field gradient. Like the constant field approach employed by Carr and Purcell, the gradient lobes enhance spin dephasing and therefore signal attenuation, being related the gradient amplitude, duration of gradient lobe application and their temporal separation. Taken together, these factors determine the degree of diffusion weighting, which is commonly referred to as the b-factor, and for PGSE sequences is given by the Stejskal-Tanner expression (see Equation 1.4, where γ is the gyromagnetic ratio, G is the amplitude of the magnetic field gradient pulses, δ is the duration they are applied, Δ is their temporal separation).

$$b = \gamma^2 G^2 \delta^2 \left[\Delta - \frac{\delta}{3} \right] \tag{1.4}$$

Another critical advancement in the development of diffusion imaging was the advent of echo planar imaging (EPI), first proposed by Sir Peter Mansfield in 1977 [75, 77]. Although limited to the laboratory setting at the time due to technological limitations, EPI promised the ability to acquire images hundreds of times faster than contemporary techniques. EPI has become ubiquitous in clinical and research MR imaging, being a key component of not only DWI, but also other imaging techniques such as functional MRI and dynamic susceptibility contrast MRI. EPI employs a series of bipolar readout gradients to generate a train of gradient echoes, being essentially an add-on to existing sequences. For example, the application of EPI to a gradient-echo sequence results in a gradient-echo EPI (GE-EPI) sequence, whereas application to a spin-echo sequence results in a spin-echo EPI (SE-EPI) sequence. SE-EPI remains the most commonly employed sequence in diffusion imaging. Typically the entirety of k-space is sampled by the gradient echo train under a single spin echo, termed single-shot SE-EPI (SSSE-EPI). Although EPI sequences have a number of unique advantages, they are also prone to a variety of artifacts. Typically these artifacts, such as ghosting, chemical shift artifacts or susceptibility artifacts, are greatest in the phase-encode direction [64], as the effective bandwidth in the

read-encode direction is greater by a factor equal to the number of phase-encode lines [99]. It is for this reason that EPI sequences in the brain are acquired with an anterior-posterior phase-encode direction, so that any artifacts that arise will be balanced on the left and right sides of the brain, thereby limiting the introduction any an artifactual differences in laterality.

In applying diffusion imaging to biological tissue, we seek to gain an understanding of the morphology or function of the target. The apparent diffusion coefficient (ADC) is one useful measure that can be calculated from diffusion-weighted imaging data. As stated by the Einstein equation (see Equation 1.3), we know that the diffusion coefficient in an isotropic (Gaussian diffusion profile) medium varies with the mean square of the displacement. In diffusion imaging we may infer the diffusion coefficient from our measurement of net displacement in an interval. However, biological tissue never exhibits a truly Gaussian diffusion profile, as there are a number of obstacles to the free diffusion of water such as macromolecules and cell membranes. Therefore, the calculated mean squared displacement will always *appear* to be somewhat lower than the diffusion coefficient expected in an isotropic medium, hence the term the apparent diffusion coefficient [69]. To calculate the ADC, one needs only two data sets that differ by a known b-factor (see Equation 1.5, where I_1 is signal intensity measured at a lower b-value, I_2 is signal intensity measured at a higher b-value, and ADC is the apparent diffusion coefficient).

$$\frac{I_1}{I_2} = exp\left(-b.ADC\right) \tag{1.5}$$

Diffusion-weighted imaging (DWI) was enthusiastically embraced in the neuroimaging community, as even subtle changes in the micro-environment of the imaging target may affect net diffusion. DWI thus provided a unique imaging contrast that was complementary to tradition imaging sequences. One of the first (and still most common applications) of DWI in clinical imaging was in the evaluation of acute ischemia. It was observed that in the early stages of ischemia, restricted diffusion could be detected while conventional images were still negative [81]. This manifests as decreased signal attenuation on DW images, and

therefore hypointensity on ADC maps. At the same, some investigators noted that the observed ADC in brain white matter appeared to be dependent on the direction in which it is was measured [22, 80]. These observations reflected the application of a limited number of gradient encoding directions to a highly-ordered tissue compartment. For example, in larger white matter tracts such as in the corpus callosum, the orientation of the fiber bundles is uniform across the voxel and we may expect that diffusion in this voxel will be highly anisotropic, i.e., diffusion will be greatest in directions parallel to the fiber bundles, and lowest antiparallel. We may assume then that if our diffusion-sensitizing gradient is applied parallel to the orientation of the fibers, we will observe greater diffusion, with the opposite being true in applying the diffusion-sensitizing gradient in more perpendicular directions. Therefore, the ADC is insufficient in characterizing diffusion characteristics in the more ordered regions of the brain.

Diffusion tensor imaging (DTI) is the next more complex model available to characterize Gaussian diffusion. The diffusion tensor is a $3x3$ covariance matrix that characterizes net displacement in three dimensions, with diagonal elements corresponding to the diffusivities along three orthogonal axes (see Equation 1.6) [13]. As the matrix is symmetric, there are only six unknown elements. Therefore, a minimum of six diffusion-weighted images (and additionally one without diffusion weighting) are required to estimate the tensor. The unknown elements are estimated from a series of diffusion-weighted images acquired with diffusion-sensitizing gradients applied in non-collinear and non-coplanar directions [12, 13]. The three eigenvalues of the diffusion tensor ($\lambda 1$, $\lambda 2$ and $\lambda 3$) correspond to the three diffusivities along the principal axes of the diffusion tensor. The orientation of the principal axes is given by the three orthogonal eigenvectors ($\varepsilon 1$, $\varepsilon 2$ and $\varepsilon 3$).

$$D = \begin{bmatrix} D_{xx} & D_{xy} & D_{xz} \\ D_{xy} & D_{yy} & D_{yz} \\ D_{xz} & D_{yz} & D_{zz} \end{bmatrix} \tag{1.6}$$

A number of metrics may be derived from the diffusion tensor, and have found wide application in clinical and research imaging. The trace of the tensor (see Equation 1.7) is the sum of the three eigenvalues while the mean diffusivity (MD) is their mean (see Equation 1.8). Additional anisotropy indices may be derived from the diffusion tensor, having the advantage of rotational invariance [95]. Fractional anisotropy (FA) is the most common of these indices, which represents the fraction of the tensor that can be assigned to anisotropic diffusion. FA is the variance of the eigenvalues about their mean, with a scaling factor applied to maintain values approximately between 0 and 1 (see Equation 1.9).

$$trace = D_{xx} + D_{yy} + D_{zz} \tag{1.7}$$

$$MD = \frac{D_{xx} + D_{yy} + D_{zz}}{3} \tag{1.8}$$

$$FA = \sqrt{\frac{3}{2}} \frac{\sqrt{(\lambda_1 - MD)^2 + (\lambda_2 - MD)^2 + (\lambda_3 - MD)^2}}{\sqrt{\lambda_1^2 + \lambda_2^2 + \lambda_3^2}} \tag{1.9}$$

FA and MD are probably the most commonly assessed DTI metrics in clinical and research settings. Although they are sensitive in detecting alterations in diffusion characteristics, they do not have any specific histopathological correlate. Radial diffusivity (RD) and axial diffusivity (AD) may be derived from the diffusion tensor, and have been shown to correspond to myelin and axonal integrity, respectively [117, 118, 119]. While AD is simply the primary eigenvalue ($\lambda 1$), RD is the mean of the second and third eigenvalues (see Equation 1.10).

$$RD = \frac{\lambda 2 + \lambda 3}{2} \tag{1.10}$$

Applications of diffusion imaging

Diffusion tensor imaging has become an invaluable tool in probing the morphological and functional characteristics of the brain in both clinical and research settings. DTI studies most often target the white matter of the brain due to its highly anisotropic structure, and have shown clinical utility in monitoring disease progression and improving the diagnostic process [e.g., 52, 96, 103]. DTI has also shown great promise in application to processes that primarily affect the gray matter with secondary white matter association, such as in neurodegenerative diseases where Wallerian degeneration follows neuronal cell death [94, 122].

The gray matter of the brain is relatively isotropic on the voxel scale, and therefore DTI is not particularly suited to characterize proton diffusion in this tissue. However, some investigators have reported changes in gray matter DTI metrics and have proposed various mechanisms to explain their observations involving hypothetical structural changes [e.g., 6, 29, 32, 47, 48, 70, 102, 132, 134, 139, 140]. Examples include the loss of myelinated fibers passing through gray matter structures [32, 102], neuronal and dendrite elimination with age [48] and the targeted loss of certain dendrite connections leading to increased anisotropy [47], as well as tissue compaction and gliosis associated with aging [134]. The presence of iron in the gray matter has also been suggested to affect DTI measurements [65, 92].

Healthy gray matter is characterized by age-related iron accumulation, with the greatest accrual occurring before 30 years of age [44]. The highest amount of iron per tissue weight is found in the globus pallidus. Other gray matter regions high in iron, in decreasing order, are the red nucleus, substantia nigra, putamen, dentate nucleus, caudate nucleus, thalamus, and various cortical regions [42, 44]. Iron is also found in the white matter in amounts comparable to or less than cortical regions [44] and is not distributed evenly, but aggregated in patches of iron-rich cells myelinating the subcortical U-fibers at the border of the cortex and white matter [25]. In addition to changes associated with healthy aging, the

concentration and form of iron may change in several chronic neurological diseases, most notably in those of neurodegenerative origin [130, 138]. Abnormal brain-iron status has also been observed in other diseases such as multiple sclerosis [141], restless legs syndrome [33], and attention deficit hyperactivity disorder [27].

Ferritin-bound iron is the principal storage form of physiologic brain iron [126], and exhibits predominantly superparamagnetic behavior at room and body temperatures [18]. Ferritin is a large water-soluble molecule with a molecular weight of approximately 450,000 g/mol, and is a spherical assembly of 24 peptide subunits approximately 80 Å in diameter. One molecule of ferritin is able to scavenge up to 4500 atoms of iron (the loading factor). The loading factors *in vivo* are usually lower at approximately 2500 atoms of iron. Ferritin is found primarily in oligodendrocytes, and to a lesser extent in microglia, astrocytes, and neurons [24, 25]. The degradation product of ferritin is hemosiderin, which is water-insoluble and can be distinguished from ferritin to a certain extent by MRI [131].

MRI is sensitive to the presence of superparamagnetic iron as it shortens T_2 relaxation time. This effect, which is dependent on the magnitude of a given field, has been exploited for many years to quantify brain iron. The CPMG sequence and the field dependent R_2 ($1/T_2$) increase (FDRI) [7] are two such methods used in clinical and research settings that take advantage of the effect of iron on T_2 relaxation time. As SE-EPI is T_2-weighted, the attenuation of signal in iron-rich areas of the brain can be readily appreciated in these images by visual inspection.

Amyotrophic lateral sclerosis

Motor neuron diseases (MND) are a group of neurological disorders which selectively affect upper and lower motor neurons, with amyotrophic lateral sclerosis (ALS) being the most common. Traditionally, ALS has been described as a neurodegenerative disorder primarily affecting motor neurons in the anterior

horns of the spinal cord, bulbar nuclei and cerebral motor cortex [86], with secondary degeneration of the emerging tracts of both the central and peripheral nervous systems [57]. Clinically, two forms of ALS may be distinguished according to the site of dominant involvement: a limb-onset and a bulbar-onset form. During the course of the disease, both forms include progressive muscle weakness, including the muscles needed for speech, swallowing and breathing.

Based on recent studies [82, 93], the perspective regarding ALS has evolved to include the broader involvement of central nervous system regions beyond the motor system. Frontal lobe involvement has been detected in ALS, and together with the cognitive impairment of approximately one-third [100] to one-half [82, 93] of patients, a link between ALS and frontotemporal lobar degeneration (FTLD) has been made. Following the discovery of the CHMP2B gene mutation in both FTLD and ALS, some authors [73] have suggested that ALS and FTLD may be part of a pathological continuum and the term FTLD-MND has been introduced.

The diagnosis of ALS is primarily clinical and is confirmed by the demonstration of lower motor neuron loss on electromyography (EMG). It often takes months to establish the final clinical diagnosis of ALS and to merely express suspicion of this disease is a stressful event for the patient and his family, as well as for the physician. Therefore, any technique that supports or opposes the diagnosis of ALS or helps to improve the understanding of its origin and development is highly desirable.

Standard MR imaging of ALS patients has not revealed any unique imaging features apart from cortical atrophy, which is also characteristic of other neurodegenerative diseases. Some MR characteristics, such as increased signal intensity on FLAIR (fluid attenuated inversion recovery) and T_2-weighted images in the corticospinal tract (e.g., in the posterior limb of the internal capsule, PLIC) [23, 39, 57] and T_2 hypointensity in the motor cortex (precentral gyrus, "low signal rim") [23, 86], have been attributed to ALS but their diagnostic relevance is equivocal.

Multiple system atrophy

Multiple system atrophy (MSA) is a sporadic, progressive neurodegenerative disease characterized by autonomic dysfunction with varying degrees of parkinsonian and/or cerebellar features. The onset of MSA is defined by the manifestation of motor dysfunction and occurs on average at fifty-five years of age, with a mean survival of only nine years [38]. Two forms of MSA are currently recognized: a parkinsonian form (MSA-P, formerly striatonigral degeneration) characterized by parkinsonian features poorly responsive to L-dopa, and a cerebellar form (MSA-C, formerly olivopontocerebellar atrophy) with predominant cerebellar ataxia. Overlap between these two divisions may be evident, both clinically and pathologically, with designation to one group determined by the predominant features at evaluation. MSA-P and MSA-C are further classified as definite, probable, or possible, reflecting the degree of certainty in the diagnosis, with a definite diagnosis of MSA requiring neuropathological confirmation. A purely autonomic form of MSA (MSA-A, or Shy-Drager syndrome) was once considered as a possible separate entity, but is not included in the current consensus criteria [38]. MSA-A likely represents MSA-P/MSA-C at an early stage of development as autonomic dysfunction is common to both.

MSA is currently considered an α-synucleinopathy, and the presence of glial cytoplasmic inclusions (GCIs) containing α-synuclein fibers and other proteins is a primary requirement for definite diagnosis. Although the precise pathogenesis of the disease remains elusive, early and widespread oligodendrocyte involvement characterized by GCI accumulation and demyelination has been documented [91, 120]. As these events correlate topographically and temporally with neuronal degeneration, it has been postulated that MSA is a primary oligodendrogliopathy [61, 136]. However, the disease process remains poorly understood and the diagnosis of MSA continues to be challenging.

MRI plays an important role in the work-up and diagnosis of MSA. Qualitative radiological signs that may be appreciable on standard MR imaging sequences are routinely used in the evaluation patients with MSA or patients suspected to have

MSA. Signal changes occurring in a cruciate pattern in the pons ("hot cross bun" sign) and signal changes in the lateral putamen are commonly sought [60]. The hot cross bun sign is associated with the selective depletion of pontine neurons and myelinated transverse pontocerebellar fibers [2, 109], while signal changes in the lateral putamen are associated with the accumulation of iron and gliosis [109, 110, 130]. These changes however are not particularly sensitive nor specific in establishing the diagnosis. The hot cross bun sign may manifest in conditions associated with pontine atrophy such as spinocerebellar ataxia [72], and correspondingly shows low specificity and only variable sensitivity in MSA-C [20, 78, 84]. Additionally, signal changes in the lateral putamen have been shown to have only variable specificity and low sensitivity in MSA-P [67, 71, 109, 111]. Therefore, DTI has the potential to greatly enhance the radiological evaluation of MSA, considering that DTI is sensitive to changes in the white matter, and these changes are generally not appreciable on standard imaging sequences. Furthermore, as MSA has been postulated to be a primary oligodendropathy, changes in RD and AD may be especially useful in elucidating the origin of white matter changes in the disease process.

Previous DTI studies in MSA have primarily used ROI [66, 113], tractography [62, 85, 124], and VBM-based [89, 125, 133] approaches. Tract-based spatial statistics (TBSS) is a newer method that is better suited to examine global DTI characteristics in brain white matter. TBSS projects the DTI data of all subjects onto a mean white-matter tract skeleton derived from the whole data set before applying voxelwise cross-subject statistics. TBSS was developed to overcome problems inherent in applying VBM to the white matter, such as partial voluming and the effects of arbitrary spatial smoothing, and improves the sensitivity, objectivity and interpretability of analyses in multi-subject diffusion imaging studies.

I'm astounded by people who want to "know" the universe
when it's hard enough to find your way around Chinatown.

Woody Allen

2

Hypotheses and Objectives

The primary objective of the present work was to demonstrate the applicability of DTI to the gray and white matter of the brain. We aimed to characterize the those factors that affect DTI metrics in brain gray matter, concurrent with our hypothesis that superparamagnetic, ferritin-bound iron makes an important contribution to DTI measurements in the these regions. This hypothesis was driven by the observation that DTI measurements in the iron-rich extrapyramidal nuclei correlate roughly with iron levels reported in postmortem studies (see Figure 3.1) [65]. To test this hypothesis, we created an *in vitro* model consisting of agarose gel phantoms doped with ferritin, and validated our results *in vivo* on healthy volunteers.

The application of DTI to neurodegenerative diseases may improve the diagnostic process and may further advance understanding of the underlying pathophysiology. We endeavored to apply DTI to ALS and MSA for that

purpose. Recent studies [28, 106] have shown the potential of DTI to improve the diagnostic process of ALS. Additionally, MSA is currently considered to be primarily a white matter disease [61, 136] with a potentially separate gray matter component [90], ideal for the application of DTI. Furthermore, these pathologies are not completely understood and have yet to be thoroughly investigated. We therefore investigated ALS and MSA for the purpose of improving the diagnostic process and advancing our understanding of the underlying pathophysiology, applying DTI as well as evaluating standard qualitative and quantitative measures.

The notes I handle no better than many pianists. But the pauses between the notes - ah, that is where the art resides.

Artur Schnabel

3

Materials and Methods

Application to gray matter

Agarose Phantom Preparation

To explore the potential effect of superparamagnetic iron on diffusion tensor indices in brain gray matter, we created an *in vitro* model of brain gray matter using agarose gel, to which we added varying amounts of superparamagnetic ferritin. Brain gray matter is a highly cellular, ordered environment, however, at the voxel scale (2.2 mm isotropic in the present data) both agarose gel and the gray matter of the brain are very homogeneous. To determine the value of fractional anisotropy in brain gray matter free of iron, we plotted the fractional anisotropy in twenty-three healthy subjects (15 men, 7 women, mean age 15.4 years $\pm$ 17.6) in the caudate nucleus, putamen and globus pallidus and frontal

gray matter as a function of expected iron content [44]. In healthy subjects, the iron content in these nuclei is highest in the globus pallidus and lowest in the frontal gray matter [44], and average values obtained in our subjects suggested a linear dependence of FA on iron content (Figure 3.1). We the took y-intercept as the value of FA we may expect in gray matter free of iron (FA $\approx$ 0.1).

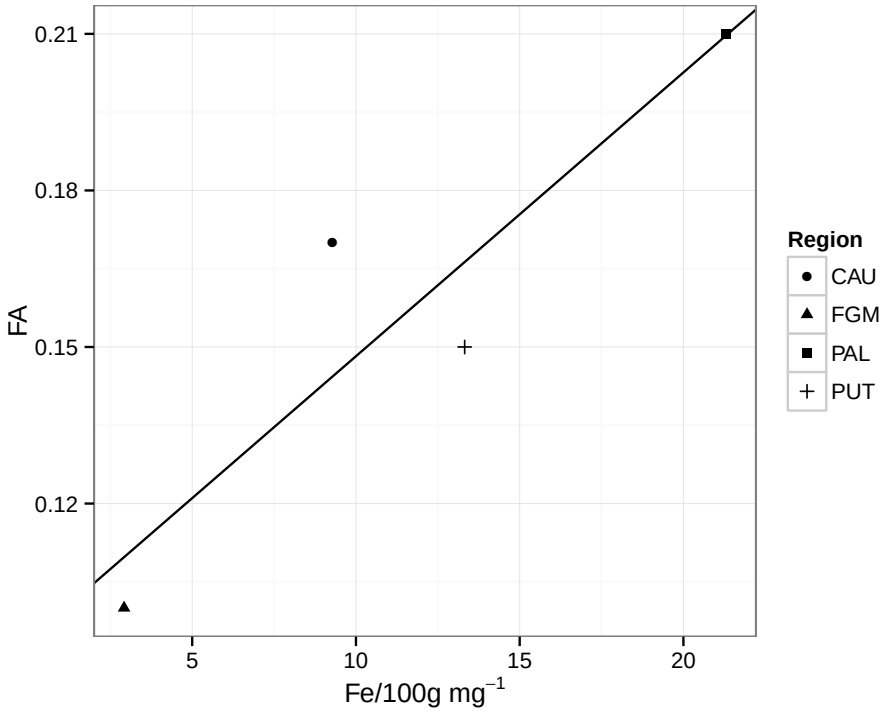


Figure 3.1: Fractional anisotropy plotted as a function of reported iron content in four gray matter regions. Regions with higher reported iron content showed correspondingly higher fractional anisotropy. Fe, iron; Cau, caudate; Put, putamen, Pal, globus pallidus; FGM, frontal gray matter.

To determine the corresponding concentration of agarose with similar diffusivity characteristics, we first constructed a series of 40-mL agarose gels at various concentrations of agarose (0.3-1.9%) prepared at physiologic pH (7.4). Agarose (Serva, Germany) was dissolved when boiled in a 50-mM Tris-HCL buffer (pH 7.4) in individual falcon tubes 115 mm in length and 26 mm in diameter. The gel

phantoms were then allowed to cool to room temperature. When imaged, the phantoms were positioned perpendicular to the B_0 field and scanned in a climate-controlled environment at 23° Celsius. ROIs were then placed in imageJ [74]. We observed a linear dependence of FA on agarose concentration, with a 1.1% concentration of agarose corresponding to an FA of approximately 10%.

An additional series of 40-mL agarose phantoms were then constructed using a 1.1% concentration of agarose at physiologic pH (7.4). Agarose (Serva, Germany) was dissolved when boiled in a 50-mM Tris-HCL buffer (pH 7.4) in individual falcon tubes 115 mm in length and 26 mm in diameter as previously. As the gels cooled to 50° Celsius, horse-spleen ferritin (Sigma-Aldrich, St. Louis, MO) was added to the individual falcon tubes and allowed to distribute evenly. Ferritin was added in 5 mg iron/100 mL increments up to 50 mg iron/100 mL, covering and exceeding those concentrations normally found within healthy human gray matter (composition of ferritin solution: 56 mg/mL ferritin, 7.1 mg/mL iron). One gel was left as a control and was allowed to cool without the addition of ferritin. The phantoms were positioned perpendicular to the B_0 field and scanned in a climate-controlled environment at 23° Celsius as previously.

Volunteer Subjects

A total of 29 volunteer subjects, 19–80 years of age (14 male, 15 female; mean age 53.2 years $\pm$ 17 SD) were included in the study. All volunteers were recruited from the community and were determined to be free of neurological disease, with no lesions detected on standard structural MR images. The study was approved by the local ethics committee and all participants provided signed, informed consent.

MR Protocol

In vitro images were acquired on Siemens Avanto 1.5T and Siemens Trio 3T systems equipped with Quantum gradients (Erlangen, Germany), using a standard 12-channel head coil. SSSE-EPI data were collected in 30 non-collinear gradient directions at 1.5T (b = 1100 s/mm^2; repetition time [TR] = 8800 ms, echo time [TE] = 98 ms; number of excitations [NEX] = 2; matrix = 128 x 128; field of view [FOV] = 280 x 280 mm; phase encode direction = AP/PA; bandwidth = 1345 Hz/px; parallel acquisition [GRAPPA] acceleration factor = 2; voxel size 2.2 mm isotropic) and 3T (b = 1100 s/mm^2; TR = 10100 ms, TE = 98 ms; NEX = 1; matrix = 146 x 146; FOV = 253 x 252 mm; phase encode direction = AP/PA; bandwidth = 1370 Hz/px; parallel acquisition [GRAPPA] acceleration factor = 2; voxel size 1.9 mm isotropic). The voxel size in the 3T SSSE-EPI sequence was reduced to compensate for higher signal-to-noise ratio (SNR) at 3T. *In vivo* SSSE-EPI was performed on the same 1.5T system with the parameters stated above, but only data in the AP phase encode direction were collected. Structural MR images were acquired in volunteer subjects using standard T_2-weighted, FLAIR, and T_2*-weighted sequences, and were used to exclude pathology.

All volunteers and phantoms were also scanned with a single-slice CPMG sequence (32 interecho times of 12.5, 25.0, 37.5 to 400.0 ms; TR = 3000 ms; in-plane resolution 0.9 x 0.9 mm; slice thickness 4 mm). In volunteer subjects placement was guided by the slice position of the whole-head T_2 sequence, and the CPMG slice was placed in the axial plane approximately parallel to the plane passing through the anterior/posterior commissures to optimally cover the basal ganglia. In phantoms the slice was placed in approximately the middle of the tube, perpendicular to the long axis.

Post-processing and Dara Evaluation

All diffusion weighted images were processed offline in FSL 4.1 (FMRIB Software Library, [116]). *In vivo* data were subjected to EPI correction, followed

by brain extraction using BET (brain extraction tool, [114]). Dtifit was then used to calculate the tensor scalars by the default least squares method, producing λ1-3, FA, and MD volumes that were used in further analyses. A single-slice CPMG image of corresponding TE was used for 2D coregistration of CPMG to T_2. The raw T_2 image without diffusion weighting generated by dtifit was then linearly coregistered to the whole- head T_2, and the transform was applied to the tensor maps created by dtifit. A single slice (corresponding to CPMG) was then extracted from the resulting volumes. This approach produced single coregistered slices (λ1-3/FA/MD/T_2/CPMG). In FSLView, masks of the globus pallidus, putamen, and caudate were placed on the CPMG data well within the nuclei to avoid partial-volume effects (Figure 3.2). In one subject the caudate nuclei, and in seven subjects the globus pallidi were not sufficiently covered by the CPMG slice and were, therefore, not included. The average signal data for each echo time were stored, generating 32 intensity values for each mask. We performed nonlinear regression of CPMG data selected by each mask using a plateau followed by monoexponential decay model for average signal intensity and interecho time with GraphPad Prism 5 (GraphPad Software Inc., La Jolla, CA). The masks created on the CPMG data were also projected to the coregistered λ1-3/FA/MD maps. Proton density (PD) was calculated for each echo-time 0 per ROI. SNR was determined on a per-ROI basis by dividing mean intra-ROI signal intensity by the SD in a noise ROI, and multiplying by 0.655 to correct for the Rician distribution of noise in magnitude images [34]. ROIs were evaluated in both hemispheres and then averaged.

In vitro SSSE-EPI data were corrected by applying a displacement field generated by estimating the displacement in each voxel from data acquired in opposite phase-encode directions [58]. Dtifit was then used to calculate the tensor scalars and produce λ1-3/FA/MD maps as above (Figure 3.3). Measurements were performed in ImageJ viewer [74], with ROIs of equal size placed directly on the diffusion-weighted and CPMG data, selecting a narrow column in the center of the tube. ROIs created on the diffusion-weighted data were then projected on the λ1-3/FA/MD maps, and SNR was determined as above. CPMG measurements

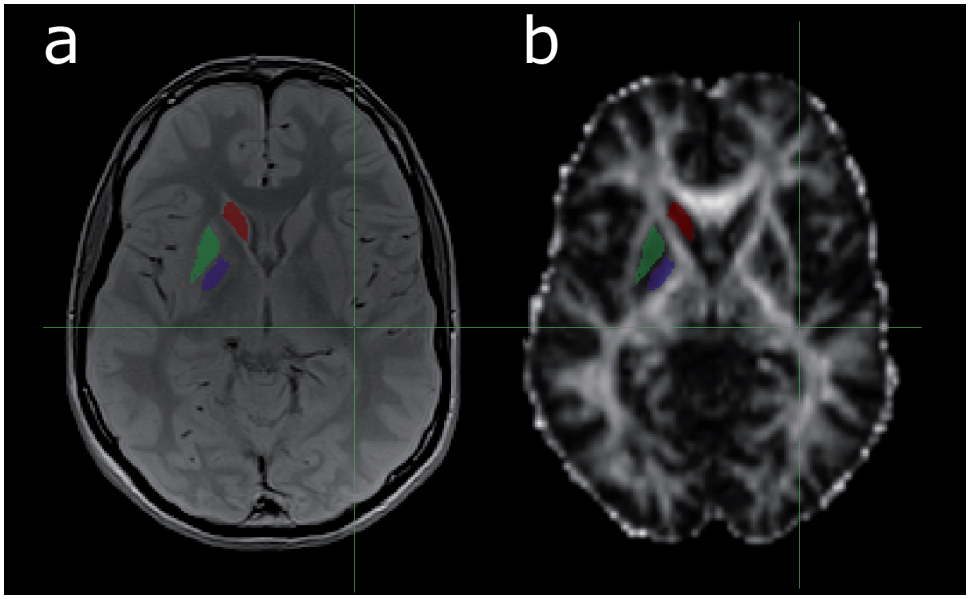


Figure 3.2: Images from one healthy volunteer showing ROIs placed in the right caudate, putamen and globus pallidus on a) CPMG data and b) corresponding coregistered FA data. CPMG, Carr-Purcell-Meiboom-Gill sequence, FA, fractional anisotropy.

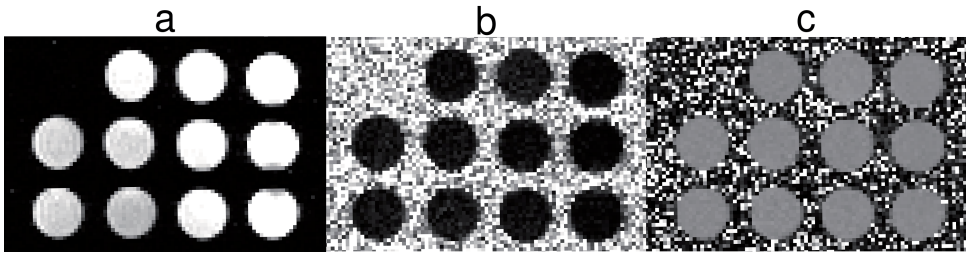


Figure 3.3: *In vitro* (1.5T) images: a) B_0, b) fractional anisotropy and c) mean diffusivity maps.

were processed in the same manner as *in vivo*.

Statistical Analyses

Statistical analyses were performed in R (www.r-project.org). No differences in laterality were detected in the *in vivo* data (t-test), therefore the mean of right and left measurements was used in the *in vivo* analyses. The Šidak correction for multiple comparisons (D/AP procedure [107], see also Appendix B) was applied to maintain an alpha level of 0.05 (all reported P-values are corrected unless otherwise stated). A power analysis was performed to ensure statistical power of at least 80%. A reciprocal transformation was applied to SNR data to achieve a linear relationship with other variables, and was used in all analyses. The Wilcoxon rank-sum test was used to examine gender differences.

Application in ALS

Subjects

A total of thirty-three subjects fulfilling the El-Escorial criteria [17] for clinically definite ALS were included in the study (18 men, 15 women; mean age 62.0 $\pm$ 8.0 SD; disease duration 3–59 months); twenty subjects diagnosed with a limb-onset form of ALS, and thirteen diagnosed with a bulbar-onset form (see Table 3.1). Disease severity was assessed with the ALS Functional Rating Scale (ALS-FRS), producing a score between 0 (greatest severity) and 40 (least severity) [1]. As the total ALS-FRS score results from a mixture of both bulbar and limb origin impairment, we elected to split the scale to limb and bulbar components to allow the correlation of motor system morphology with clinical signs of motor disability. All subjects were further evaluated for the presence or absence of dementia by a series of neuropsychological tests [105]. Nineteen subjects exhibited a predominantly frontal-type cognitive impairment and behavioral disturbances consistent with FTLD, while twelve subjects were found

to be cognitively normal. The results of neuropsychological examination were not available for two subjects. Thirty healthy, age-matched volunteers (16 men, 14 women; mean age 59.7 $\pm$ 10.0 SD) were also included in the study as a control group. All volunteers underwent an examination to exclude neurological disease. The study was approved by the local ethics committee and all participants provided signed informed consent.

MR protocol

Imaging was performed on a Siemens Symphony 1.5T System (Erlangen, Germany). Structural MR images were acquired using a T1-weighted magnetization-prepared rapid acquisition gradient echo (MP-RAGE) sequence (TR = 2140 ms, TE = 3.93 ms, flip angle = 15 degrees, TI = 1100 ms, 160 axial slices, 1.65mm slice thickness, x–y resolution 0.9 × 0.9 mm, FOV 238 mm) and a standard TSE T_2-weighted sequence covering the entire brain and cerebellum. T_2 relaxometry data were acquired by a single slice CPMG sequence (32 interecho times of 14.4, 24.8, 37.2 to 396.8 ms; TR = 3000 ms; in-plane resolution 0.89 × 0.89 mm; slice thickness 4 mm) in the region of the basal ganglia. Diffusion data were obtained using a Siemens work in progress package with b-factors of 0, 400, and 1100 measured along 30 non-collinear gradient directions (TR = 7900 ms, TE = 101 ms, 70 axial slices, NEX = 2, 1.25 × 1.25 × 2.5 mm).

Post-processing and data evaluation

T_2-weighted images covering the whole brain as well as raw data for quantitative analysis were evaluated to exclude other significant pathologies. T_2 relaxometry was performed in thirty-one subjects (16 men, 15 women; mean age 61.6 ± 8.0 SD). The CPMG data were affected by artifacts in two subjects and were excluded from the analyses.

T_2 relaxometry data were analyzed using ImageJ viewer [74], placing circular ROIs measuring twenty-one square millimeters in the bilateral frontal white

Table 3.1: ALS patient demographics

Sub	Age (y)	Sex	FRS	FRS-L	FRS-B	Form	Dem	Dur (m)	Pro
1	66.1	M	31	18	13	limb	yes	13	R
2	58.5	M	31	15	16	limb	yes	7	R
3	67.5	M	33	24	9	bulbar	yes	13	R/D
4	39.5	M	32	18	14	limb	yes	54	R/D
5	56.6	M	37	21	16	limb	no	9	R
6	76.2	M	36	24	12	limb	yes	21	R
7	67.1	F	35	24	11	bulbar	yes	24	R
8	68.8	M	31	15	16	limb	yes	13	R
9	61	F	24	9	15	limb	yes	14	R
10	61.9	F	33	20	13	bulbar	yes	8	R
11	49.2	M	37	21	16	limb	no	9	R/D
12	65.6	M	38	24	14	bulbar	yes	4	R
13	68.4	M	36	23	13	bulbar	yes	7	R/D
14	65.5	F	36	24	12	bulbar	yes	17	R
15	56.7	M	38	24	14	bulbar	no	21	R
16	61.1	M	30	15	15	limb	yes	8	R
17	63.3	F	30	16	14	limb	yes	12	R
18	58.9	M	29	13	16	limb	yes	11	R
19	59	F	39	24	15	bulbar	no	8	R
20	52	F	34	21	13	bulbar	no	9	R
21	59.7	F	37	24	13	bulbar	no	12	R
22	52.9	M	38	22	16	limb	no	59	R/D
23	66.1	F	32	16	16	limb	yes	15	R
24	64.8	M	40	24	16	limb	NR	5	R
25	70.9	M	37	21	16	limb	yes	14	R/D
26	47.3	F	32	19	13	limb	no	8	R
27	53	M	38	24	14	bulbar	no	13	R
28	78.6	F	36	24	12	bulbar	yes	14	R/D
29	73.3	F	33	24	9	bulbar	no	25	R/D
30	60.3	M	39	23	16	limb	no	29	D
31	65.2	F	37	21	16	limb	yes	25	R/D
32	71.6	M	38	22	16	limb	no	41	D
33	57.6	M	31	22	9	limb	NR	13	R/D

Table 3.1: Demographic characteristics of all ALS patient participants. ALS, Amyotrophic lateral sclerosis; Sub, subject; y, years; FRS, functional rating scale; FRS-L, limb component of FRS; FRS-B, bulbar component of FRS; Dem, dementia; Dur, duration; Pro, protocol; R, relaxometry; D, diffusion tensor imaging; NR, not reported.

matter (FWM), frontal grey matter (FGM, cingulate gyrus) and posterior limb of the internal capsule (PLIC). The basal ganglia (head of caudate nucleus, putamen, globus pallidus) were manually outlined bilaterally using freehand selection (Figure 3.4). ROI placement was determined on the highest contrast T_2 image, and the average signal data for each echo time were stored, generating 32 intensity values for each ROI. We performed nonlinear regression for each ROI using a monoexponential decay model for average signal intensity and interecho time with GraphPad Prism 4 (GraphPad Software Inc., La Jolla, CA, USA). PD values were individually calculated for echo time 0 in each ROI. T_2 relaxation rate (R_2) and PD signal were statistically analyzed using R (www.r-project.org).

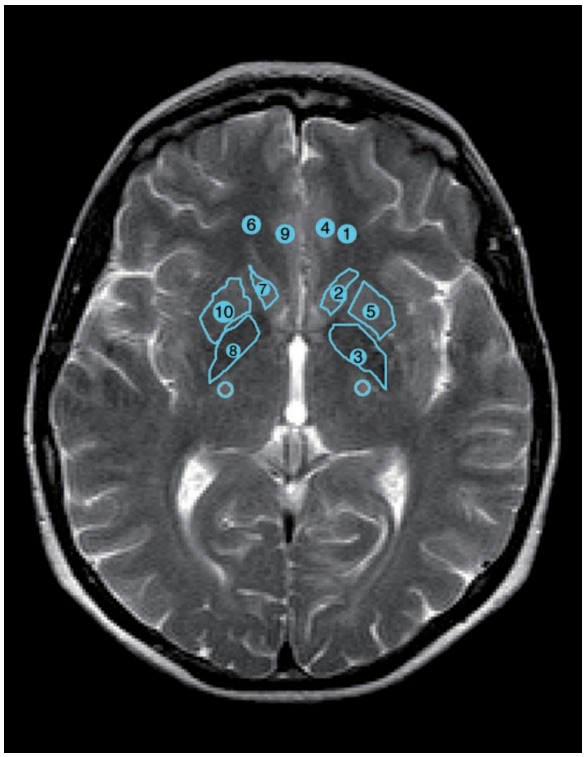


Figure 3.4: ROI placement in ALS subjects and controls: frontal white matter (1,6), frontal grey matter (4, 9), head of caudate nucleus (2,7), putamen (5,10), globus pallidus (3, 8), and internal capsule (not numbered)

Twelve subjects (9 men, 3 women; mean age 62.97 $\pm$ 11.0 SD) and twelve healthy

volunteers (9 men, 3 women; mean age 63.22 $\pm$ 10.7 SD) were included in the DTI study. Diffusion weighted images were processed off-line in FSL [116]. After eddy-current and motion correction, brain extraction was performed using BET [114] and dtifit was then used to calculate the scalar invariants of the tensor [116]. Dtifit generates 3D images at the same matrix size and resolution as the original diffusion images, including a raw T_2-signal image with the same distortions as the diffusion weighted images. FA and MD were measured using ImageJ viewer [74], using circular ROIs measuring twenty-one square millimeters as placed on the relaxometry data. When analyzing the corticospinal tract (CST), ROIs were placed directly on the FA and MD maps. All other ROIs were placed directly on the T_2 maps created by dtifit, and then projected on the corresponding FA and MD maps. To validate the ROI approach, voxelwise statistical analyses of the FA data was carried out using TBSS (Tract-Based Spatial Statistics, [115]). For this analysis, only the upper slab covering the brain from the vertex to mesencephalon was used. The skeleton was built using an FA threshold > 0.3. An unpaired t-test was then used to compare FA values in the patient and control group.

Statistical analyses

Normality was tested by the Shapiro test at a P-value threshold of < 0.05. Linear regression analysis of R_2 over age and ALS-FRS was performed. As normality of R_2 in patients and controls was not confirmed by the Shapiro test in any region, a single-tailed Wilcoxon two-sample test was used for intergroup comparisons using an *a priori* hypothesis of decreased R_2 in the patient group. The Bonferroni correction for multiple comparisons was applied to maintain an alpha level of 0.05. The same methodology was used to evaluate the correlation between FA/MD, age, and clinical scale.

Application in MSA

Subjects

Twenty subjects diagnosed as probable MSA were recruited for the study (10 male, 10 female, 60.9 Y $\pm$ 7 SD), including ten patients diagnosed as probable MSA-P (4 male, 6 female, mean age 62.0 Y $\pm$ 9 SD) and ten patients diagnosed as probable MSA-C (5 male, 5 female, mean age 59.9 Y $\pm$ 4 SD). Demographic characteristics of the MSA group are presented in Table 3.2. Twenty healthy volunteer subjects (9 male, 11 female, mean age 61.3 Y $\pm$ 7 SD) were additionally included as controls. The study was approved by the local ethics committee and all participants provided signed, informed consent.

MRI protocol and post-processing

Imaging was performed on a Siemens Avanto 1.5T scanner fitted with a 12-channel 4-segment head coil (Erlangen, Germany). Structural MR images acquired using standard PD-weighted, T1-weighted, T_2-weighted, FLAIR and T_2*-weighted sequences were used to exclude pathology in control subjects and to evaluate the presence/absence of radiological signs typically associated with MSA; signal changes in the lateral putamen associated with the accumulation of iron and gliosis [109, 110, 130] (Figure 3.5a), and signal changes occurring in a cruciate pattern in the pons ("hot cross bun" sign) associated with the selective depletion of pontine neurons and myelinated transverse pontocerebellar fibers [109] (Figure 3.5b). Radiological signs were assessed by two experienced observers (JV, AR), and any discrepancies resolved by consensus.

Diffusion-weighted data were acquired in 12 non-collinear gradient directions using a standard SSSE-EPI sequence (b=1100; TR=8839 ms, TE=95 ms; NEX=2; 2.2 mm isotropic voxel). Diffusion data were processed offline in FSL [116] and subjected to eddy-current and motion correction, followed by brain

Table 3.2: MSA Patient demographics

Subject	Sex	Age (y)	Park	Cerebellar Sx	LRP Sx	HCB Sx	Dur (y)	Dx
01	F	59.6	−	+	−	+	4	MSA-C
02	F	69.4	+	+	−	+	2	MSA-P
03	F	63.3	+	+	+	+	3	MSA-C
04	M	65.7	+	−	+	−	2	MSA-P
05	M	58.7	+	+	+	+	5	MSA-C
06	F	49.7	+	+	+	+	4	MSA-C
07	M	68.3	+	−	+	−	2	MSA-P
08	M	65.3	+	+	+	−	10	MSA-C
09	F	80.3	+	+	+	+	3	MSA-P
10	M	61.5	+	+	+	+	6	MSA-C
11	F	55.0	+	+	+	+	8	MSA-P
12	M	62.9	−	+	−	+	2	MSA-C
13	F	60.2	−	+	−	+	5	MSA-C
14	F	56.3	+	+	+	+	2	MSA-C
15	M	59.0	+	−	+	+	3	MSA-P
16	M	55.1	+	−	+	−	5	MSA-P
17	F	53.4	+	+	+	−	2	MSA-P
18	F	53.6	+	−	+	−	1	MSA-P
19	F	60.2	+	−	+	+	6	MSA-P
20	M	61.1	−	+	+	−	2	MSA-C

Table 3.2: Demographic characteristics of all MSA patient participants. Parkinsonism was considered positive in the presence of bradykinesia and rigidity, while cerebellar signs were documented as positive in the presence of gait ataxia, cerebellar dysarthria, limb ataxia, or cerebellar oculomotor dysfunction. y, years; Park, Parkinsonism; Sx, sign/signs; LRP, lateral rim of the putamen; HCB, hot cross bun; Dur, duration; dx, diagnosis; F, female; M, male; MSA-C, multiple system atrophy, cerebellar subtype; MSA-P multiple system atrophy, parkinsonian subtype.

extraction [114]. DTIFit was then used to calculate the scalar invariants of the tensor, and FA, MD, RD and AD maps were generated. Voxelwise statistical analyses of the diffusion-weighted data were carried out using TBSS [115]. A study-specific mean FA template was created and used in transforming all subjects to standard 1x1x1 mm MNI152 space. The white matter skeleton was thresholded at FA > 0.4 and statistical tests were performed using 10,000 permutations. The results were thresholded using threshold-free cluster enhancement at the $P < 0.05$ level of significance.

Automated ROI analyses were additionally performed in template space in the basal ganglia (caudate nucleus, putamen, globus pallidus). The ROIs were created by separating the stated masks from the Harvard-Oxford subcortical structural atlas (thr50), transforming them to study space and finally twice eroding to minimize partial volume effects. The ROIs were then projected against the diffusion tensor data (FA/MD/RD/λ1/λ3). The ROI data were then further processed in R (www.r-project.org). The Šidák correction for multiple comparisons (D/AP procedure [107], see also Appendix B) was applied to maintain an alpha level of 0.05 (all reported P-values are corrected unless otherwise stated). A one-way analysis of variance (ANOVA) test was used to test for group differences, followed by the Tukey-Kramer procedure in those regions and metrics that reached significance. The pROC package [101] was used for receiver operating characteristic (ROC) analyses of ROI data. The MCP was also the target of ROC analysis. This ROI was extracted from the Johns Hopkins University (JHU)-white-matter labels [88], transformed to study space, and then skeletonized against the mean-FA skeleton.

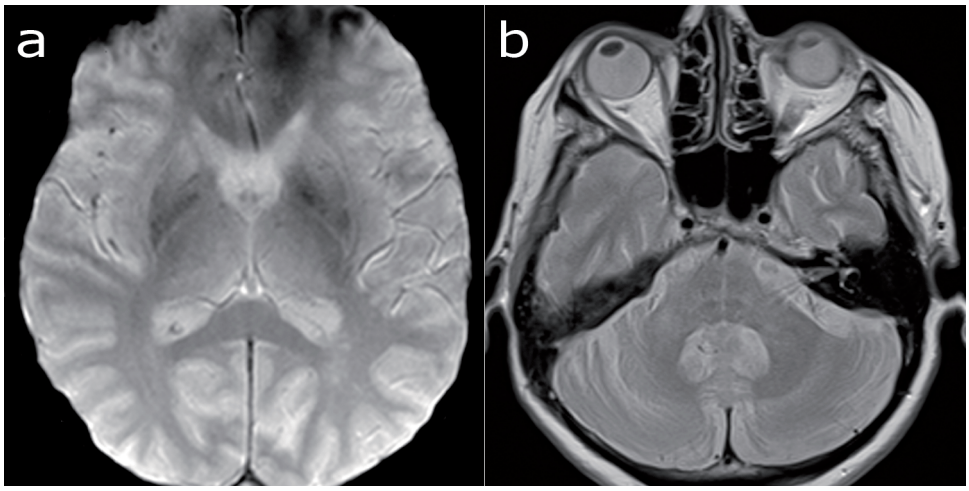


Figure 3.5: Qualitative radiological signs typically associated with MSA. a) Signal changes visible on T_2*-weighted sequence in the lateral putamen. The patient was diagnosed as MSA-C. b) Incipient signal changes occurring in a cruciate pattern in the pons ("hot cross bun" sign) seen on PD-weighted sequence. The patient was diagnosed as MSA-P.

When you meet a master swordsman, show him your sword. When you meet a man who is not a poet, do not show him your poem.

Lin-Chi

4

Results

Application to gray matter

A linear dependence of R_2 (1/T2) on ferritin-bound iron concentration was observed in vitro at 1.5T (Figure 4.1a; $R^2 = 0.99$, $P < 0.001$) and at 3T (Figure 4.1b; $R^2 = 0.99$, $P < 0.001$). The relationship between SNR and R_2 was found to be reciprocal, therefore reciprocal SNR (1/SNR) was used in all further analyses to achieve linearity. 1/SNR was observed to increase linearly (SNR decreased) with increasing iron concentration at both 1.5T (Figure 4.2a; $R^2 = 0.79$, $P = 0.002$) and at 3T (Figure 4.2b; $R^2 = 0.84$, $P < 0.001$), and also increased linearly (SNR decreased) with increasing R_2 at 1.5T (Figure 4.3a; $R^2 = 0.80$, $P = 0.001$) and 3T (Figure 4.3b; $R^2 = 0.86$, $P < 0.001$).

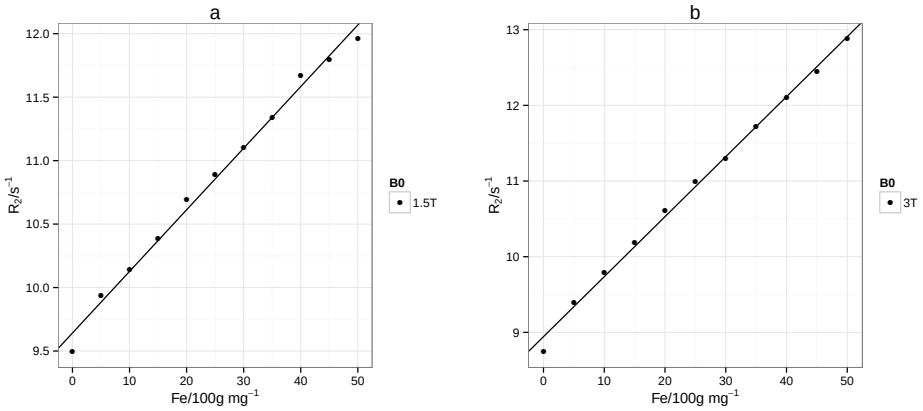


Figure 4.1: *In vitro* results: Linear dependence of R_2 on ferritin-bound iron at a) 1.5T ($R^2 = 0.99$, $P < 0.001$) and b) 3T ($R^2 = 0.99$, $P < 0.001$). Fe, ferritin-bound iron; R_2, $1/T_2$.

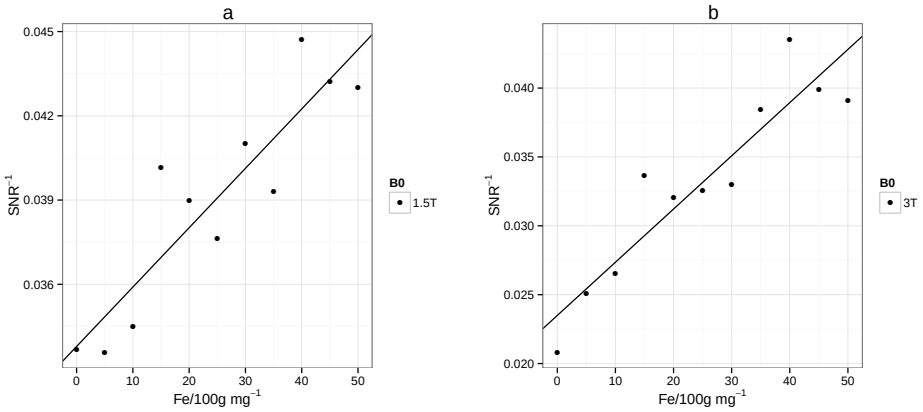


Figure 4.2: *In vitro* results: Linear dependence of 1/SNR on ferritin-bound iron at a) 1.5T ($R^2 = 0.79$, $P = 0.002$) and b) 3T ($R^2 = 0.84$, $P < 0.001$). Fe, ferritin-bound iron; SNR, signal-to-noise ratio.

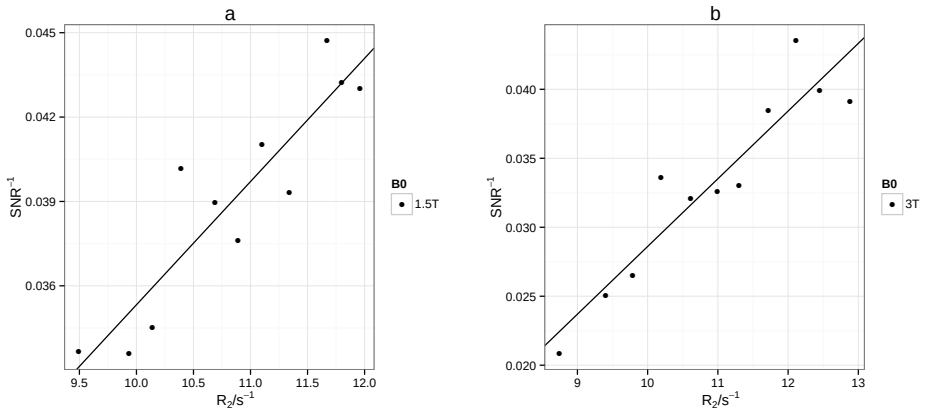


Figure 4.3: *In vitro* results: Linear dependence of 1/SNR on R_2 at a) 1.5T ($R^2 = 0.80$, $P = 0.001$) and b) 3T ($R^2 = 0.86$, $P < 0.001$). R_2, $1/T_2$; SNR, signal-to-noise ratio.

In examining the linear relationship between the Eigenvalues (λ1–3) and 1/SNR (Figure 4.4a), only the fit between λ3 and 1/SNR at 3T was significant ($R^2 = 0.92$, $P < 0.001$), although there was a trend between λ1 and 1/SNR at 3T ($R^2 = 0.49$, $P = 0.08$). Correlation between the Eigenvalues and R_2 was similar (Figure 4.4b), with the fit between λ3 and R_2 significant at 3T ($R^2 = 0.70$, $P = 0.006$) and a trend between λ1 and R_2 at 3T ($R^2 = 0.53$, $P = 0.06$). A linear correlation was observed between FA and 1/SNR at 1.5T (Figure 4.5a; $R^2 = 0.74$, $P = 0.004$) and 3T (Figure 4.5b; $R^2 = 0.84$, $P < 0.001$). The fit between FA and R_2 did not reach significance at 1.5T (Figure 4.6a; $R^2 = 0.40$, $P = 0.17$), but was significant at 3T (Figure 4.6b; $R^2 = 0.76$, $P = 0.002$). No changes in MD were detected (Figure 4.7).

A linear dependence of 1/SNR on R_2 was observed in vivo ($R^2 = 0.67$, $P < 0.001$). The Eigenvalues decreased linearly with increasing R_2 (Figure 4.9a; λ1: $R^2 = 0.10$, $P = 0.03$; λ2: $R^2 = 0.36$, $P < 0.001$; λ3: $R^2 = 0.58$, $P < 0.001$), and a similar pattern was seen between the Eigenvalues and 1/SNR, although the fit with λ1 was not significant (Figure 4.9b; λ1: $R^2 = 0.02$, $P = 0.56$; λ2: $R^2 = 0.17$,

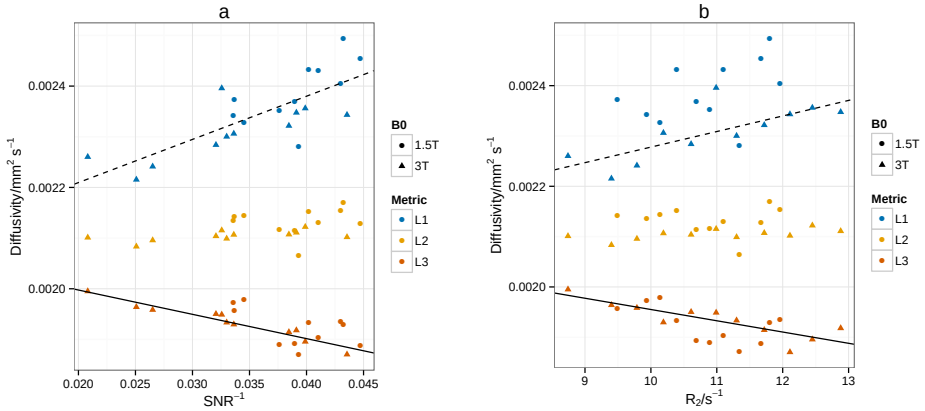


Figure 4.4: *In vitro* results: Eigenvalues (λ1–3) plotted as a function of a) 1/SNR (3T, λ3: $R^2 = 0.92$, $P < 0.001$; 3T, λ1: $R^2 = 0.49$, $P = 0.08$) and b) R_2 (3T, λ3: $R^2 = 0.70$, $P < 0.006$; 3T, λ1: $R^2 = 0.53$, $P = 0.06$). R_2, $1/T_2$; SNR, signal-to-noise ratio.

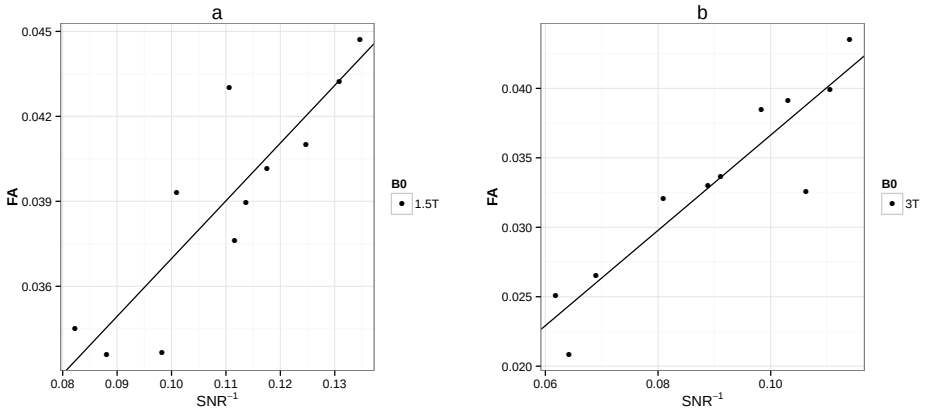


Figure 4.5: *In vitro* results: Linear dependence of FA on 1/SNR at a) 1.5T ($R^2 = 0.74$, $P = 0.004$) and b) 3T ($R^2 = 0.84$, $P < 0.001$). FA, fractional anisotropy; SNR, signal-to-noise ratio.

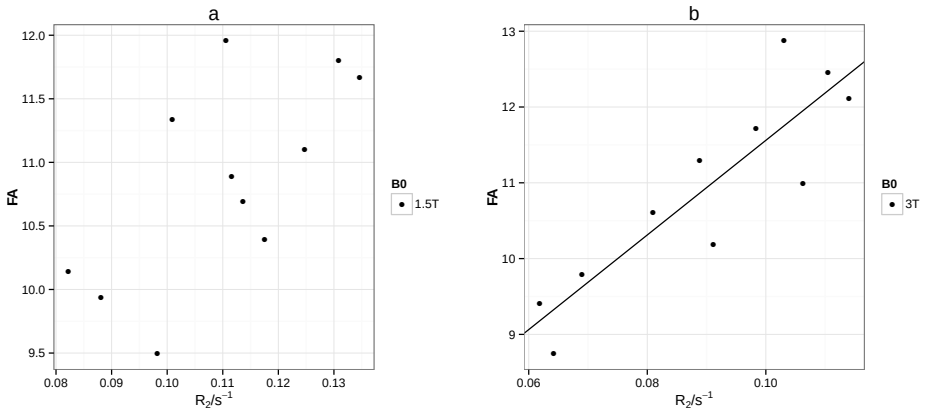


Figure 4.6: *In vitro* results: FA plotted as a function of R_2 at a) 1.5T and b) 3T ($R^2 = 0.76$, $P = 0.002$). FA, fractional anisotropy; R_2, $1/T_2$.

$P < 0.001$; $\lambda 3$: $R^2 = 0.34$, $P < 0.001$).

As in vitro, FA increased with increasing 1/SNR (Figure 4.10; $R^2 = 0.34$, $P < 0.001$) and R_2 (Figure 4.10; $R^2 = 0.51$, $P < 0.001$), with stronger correlation between FA and R_2. MD decreased with increasing 1/SNR ($R^2 = 0.19$, $P < 0.001$) and R_2 (Figure 4.11; $R^2 = 0.39$, $P < 0.001$), again with stronger correlations between MD and R_2. PD correlated only weakly with R_2 ($R^2 = 0.15$, $P = 0.003$), FA ($R^2 = 0.22$, $P < 0.001$), and $\lambda 3$ ($R^2 = 0.13$, $P = 0.006$).

In individual nuclei, correlations were observed in the globus pallidus between the eigenvalues and R_2 (Figure 4.13a; $\lambda 1$: $R^2 = 0.46$, $P = 0.004$; $\lambda 2$: $R^2 = 0.39$, $P = 0.013$; $\lambda 3$: $R^2 = 0.43$, $P = 0.006$). No correlation was found between FA and R_2 in the globus pallidus (Figure 4.13b; $R^2 = 0.17$, $P = 0.31$), however, a linear dependence between MD and R_2 was seen (Figure 4.13c; $R^2 = 0.53$, $P < 0.001$). Correlation between age and tensor-derived scalars was only observed in the putamen. A linear relationship between $\lambda 1$, $\lambda 2$ and age was detected (Figure 4.14a; $\lambda 1$: $R^2 = 0.42$, $P = 0.001$; $\lambda 2$: $R^2 = 0.25$, $P = 0.036$; $\lambda 3$: $P = 0.051$), as well as between MD and age (Figure 4.14c; $R^2 = 0.29$, $P = 0.019$). No correlation between FA and age was observed in the putamen (Figure 4.14b; $P = 0.35$). No

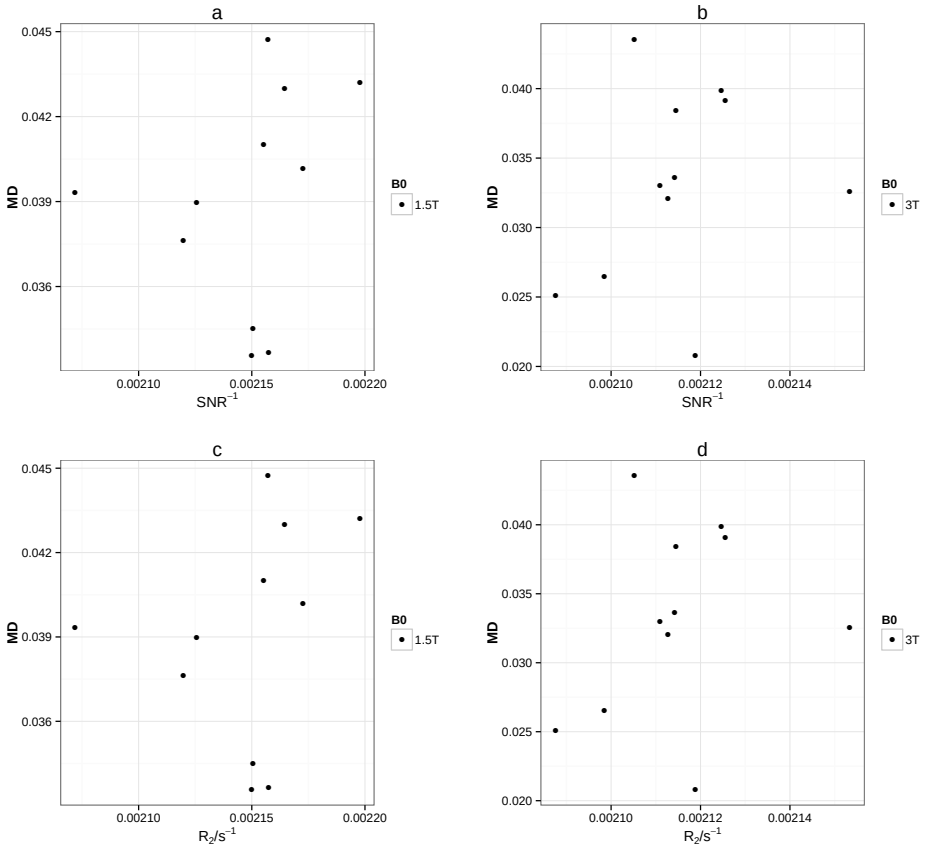


Figure 4.7: *In vitro* results: MD plotted as a function of 1/SNR at a) 1.5T and b) 3T, and as a function of R_2 at c) 1.5T and d) 3T. MD, mean diffusivity; SNR, signal-to-noise ratio; R_2, $1/T_2$.

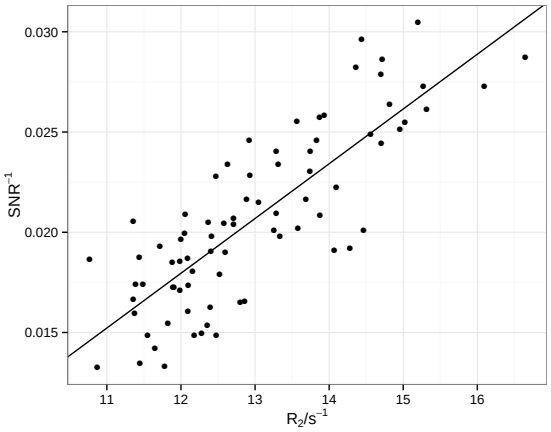


Figure 4.8: *In vivo* results: Linear dependence of 1/SNR on R_2 ($R^2 = 0.67$, $P < 0.001$). SNR, signal-to-noise ratio; R_2, $1/T_2$.

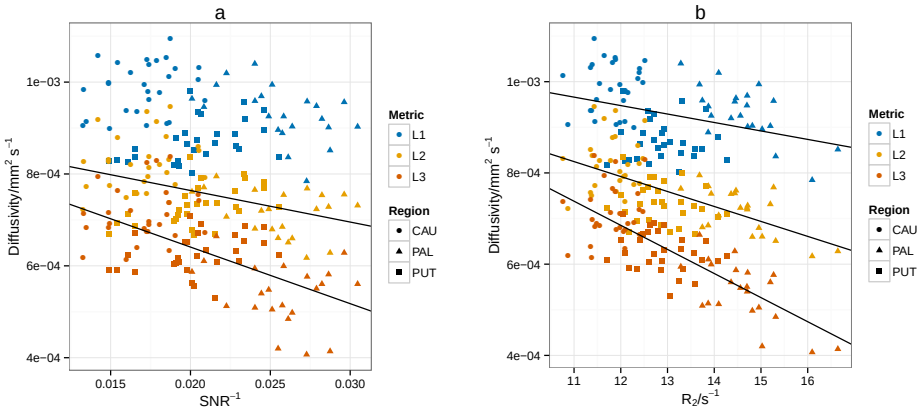


Figure 4.9: *In vivo* results: Eigenvalues plotted as a function of a) 1/SNR ($\lambda 2$: $R^2 = 0.17$, $P < 0.001$; $\lambda 3$: $R^2 = 0.34$, $P < 0.001$) and b) R_2 ($\lambda 1$: $R^2 = 0.10$, $P = 0.03$; $\lambda 2$: $R^2 = 0.36$, $P < 0.001$; $\lambda 3$: $R^2 = 0.58$, $P < 0.001$). SNR, signal-to-noise ratio; R_2, $1/T_2$.

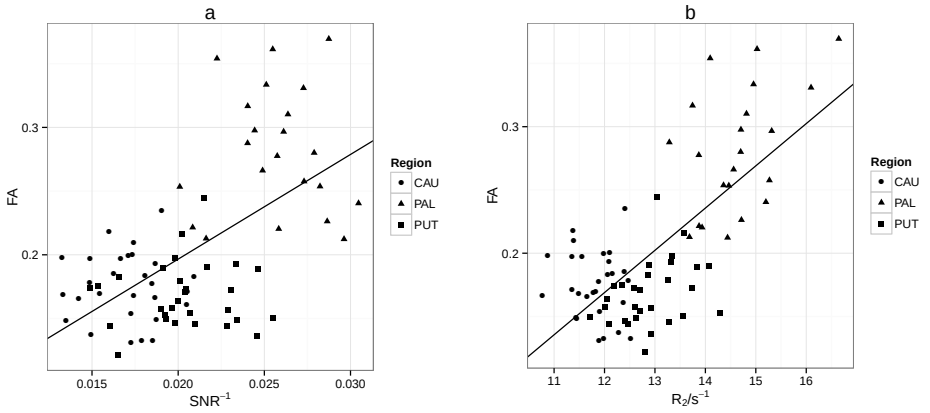


Figure 4.10: *In vivo* results: Linear dependence of FA on a) 1/SNR ($R^2 = 0.34$, $P < 0.001$) and b) R_2 ($R^2 = 0.51$, $P < 0.001$). FA, fractional anisotropy; SNR, signal-to-noise ratio; R_2, $1/T_2$.

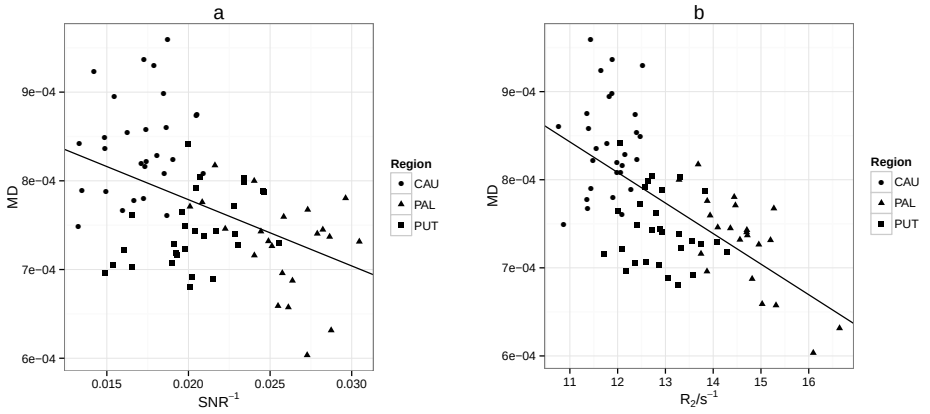


Figure 4.11: *In vivo* results: Linear dependence of MD on a) 1/SNR ($R^2 = 0.19$, $P < 0.001$) and b) R_2 ($R^2 = 0.39$, $P < 0.001$). MD, mean diffusivity; SNR, signal-to-noise ratio; R_2, $1/T_2$.

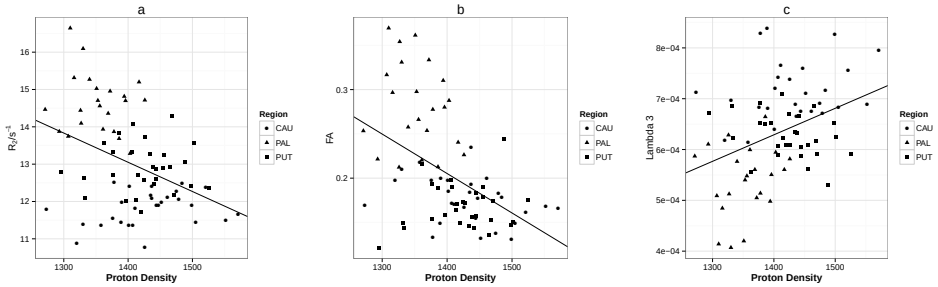


Figure 4.12: *In vivo* results: Linear dependence of a) R_2 ($R^2 = 0.15$, $P = 0.003$), b) FA ($R^2 = 0.22$, $P < 0.001$) and c) $\lambda 3$ ($R^2 = 0.13$, $P = 0.006$) on proton density. R_2, $1/T_2$; FA, fractional anisotropy.

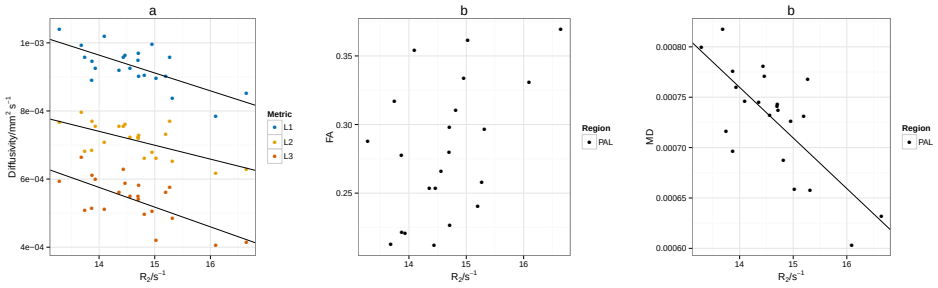


Figure 4.13: *In vivo* results, globus pallidus: Linear dependence of a) the eigenvalues on R_2 ($\lambda 1$: $R^2 = 0.46$, $P = 0.004$; $\lambda 2$: $R^2 = 0.39$, $P = 0.013$; $\lambda 3$: $R^2 = 0.43$, $P = 0.006$), FA plotted as a function of R_2 ($P = 0.31$), and c) linear dependence of MD on R_2 ($R^2 = 0.53$, $P < 0.001$). FA, fractional anisotropy, MD, mean diffusivity; R_2, $1/T_2$.

correlations between age and other covariates were observed in pooled data, nor were any group-wise differences between genders detected.

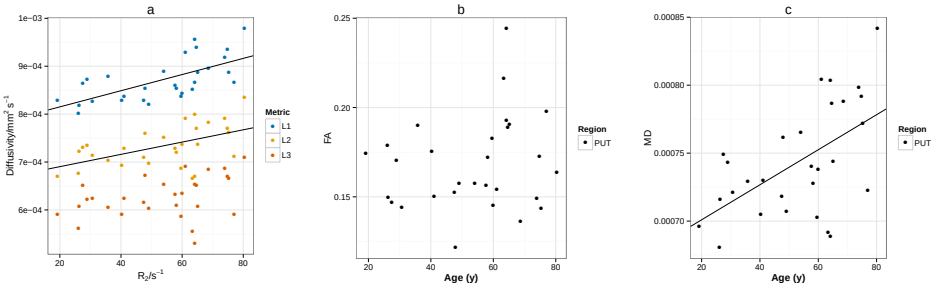


Figure 4.14: *In vivo* results, putamen: Linear dependence of a) $\lambda 1$ and $\lambda 2$ on age ($\lambda 1$: $R^2 = 0.42$, $P = 0.001$; $\lambda 2$: $R^2 = 0.25$, $P = 0.036$; $\lambda 3$: $P = 0.051$), FA plotted as a function of age ($P = 0.35$), and c) linear dependence of MD on age ($R^2 = 0.29$, $P = 0.019$). FA, fractional anisotropy, MD, mean diffusivity; y, years.

Application in amyotrophic lateral sclerosis

We detected significantly decreased R_2 in the head of the left caudate nucleus ($P = 0.002$, uncorrected) in ALS subjects in comparison with healthy volunteers (Table 4.1). No dependence of R_2 on disease duration was observed. Lower R_2 was also present in the deep FWM in ALS patients in comparison with controls (left, $P = 0.002$ uncorrected; right, $P = 0.004$ uncorrected). R_2 in the FWM also correlated negatively with age in both patients and controls. No relaxometric differences in the head of the caudate nuclei or FWM were found between ALS subgroups with or without cognitive deficit.

No relaxometric differences between ALS and control subjects were detected in the PLIC, a region suspected of signal intensity changes in ALS [23, 39, 57]. T_2 hyperintensity in the PLIC was qualitatively appreciated at least unilaterally in all patients and controls. Using an ROI-based approach, no correlation between clinical scale or age and FA or MD was observed in the PLIC. Furthermore, no differences in FA were detected between patients and healthy volunteers in the PLIC or FWM. We therefore elected to perform TBSS on the upper slab of

Table 4.1: T_2 relaxometry results

Region	ALS	SD	Controls	SD	P-value
Head CN, L	99.7	6.4	95.6	3.4	0.002*
Head CN, R	99	7.1	96.6	4.5	0.023
FWM, L	88.8	7.8	84	4.9	0.002*
FWM, R	88.2	6.3	84.4	4.5	0.004*
GP, L	72	5.4	73	5.7	
GP, R	72.2	5.9	73.7	6.6	
Cingulate, L	107.9	8.6	107.1	4	
Cingulate, R	105.2	10.6	107.6	5.4	
Putamen, L	88.8	5.9	87.8	5.6	
Putamen, R	88.4	6.9	88.7	6.3	
CST, L	107.3	7	106.5	4.4	
CST, R	107.6	6.6	108	5.2	

Table 4.1: T_2 relaxometry results (in milliseconds) in ALS and control subjects. P-values are uncorrected, significant differences after correction for multiple comparisons are marked with an asterisk (*). ALS, amyotrophic lateral sclerosis; SD, standard deviation; L, left; R, right; CN, caudate nucleus; FWM, frontal white matter; GP, globus pallidus; Cingulate, cingulate gyrus; CST, corticospinal tract.

diffusion data. No correlation with FRS was found, but decreased FA in ALS patients was present in the bilateral corona radiata (Figure 4.15).

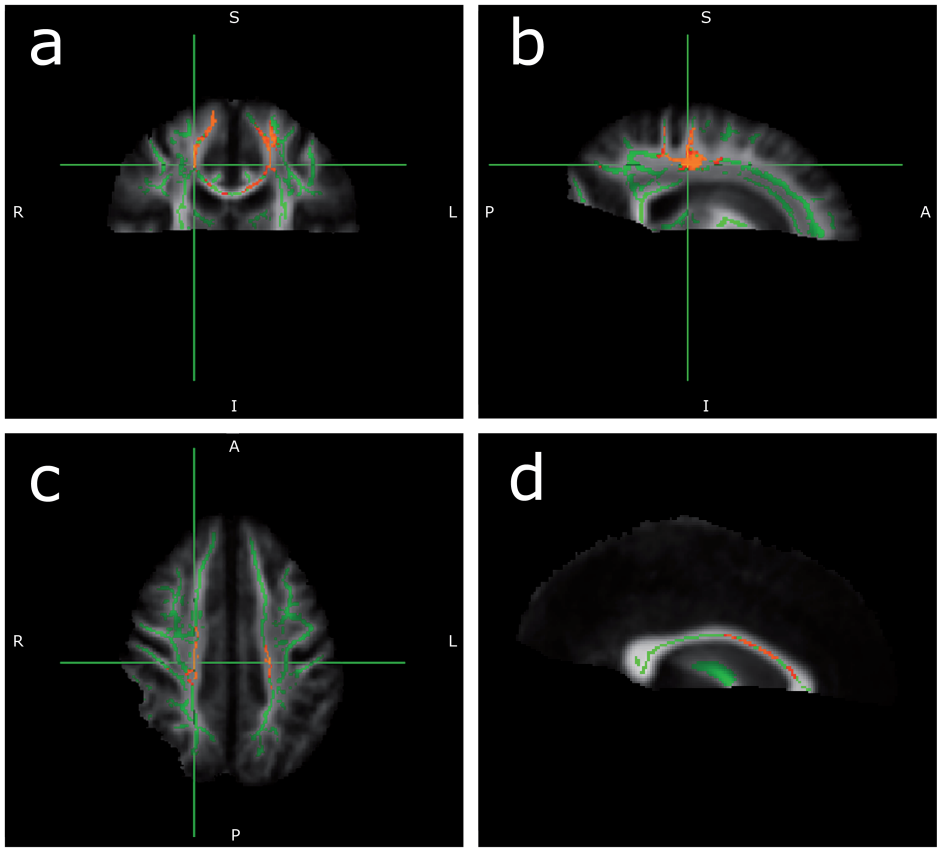


Figure 4.15: Voxels demonstrating significant ($P < 0.05$) differences in FA between all patients and controls (patients $<$ controls) in the a) coronal, b) sagittal, c) axial and d) mid-sagittal planes.

Application in multiple system atrophy

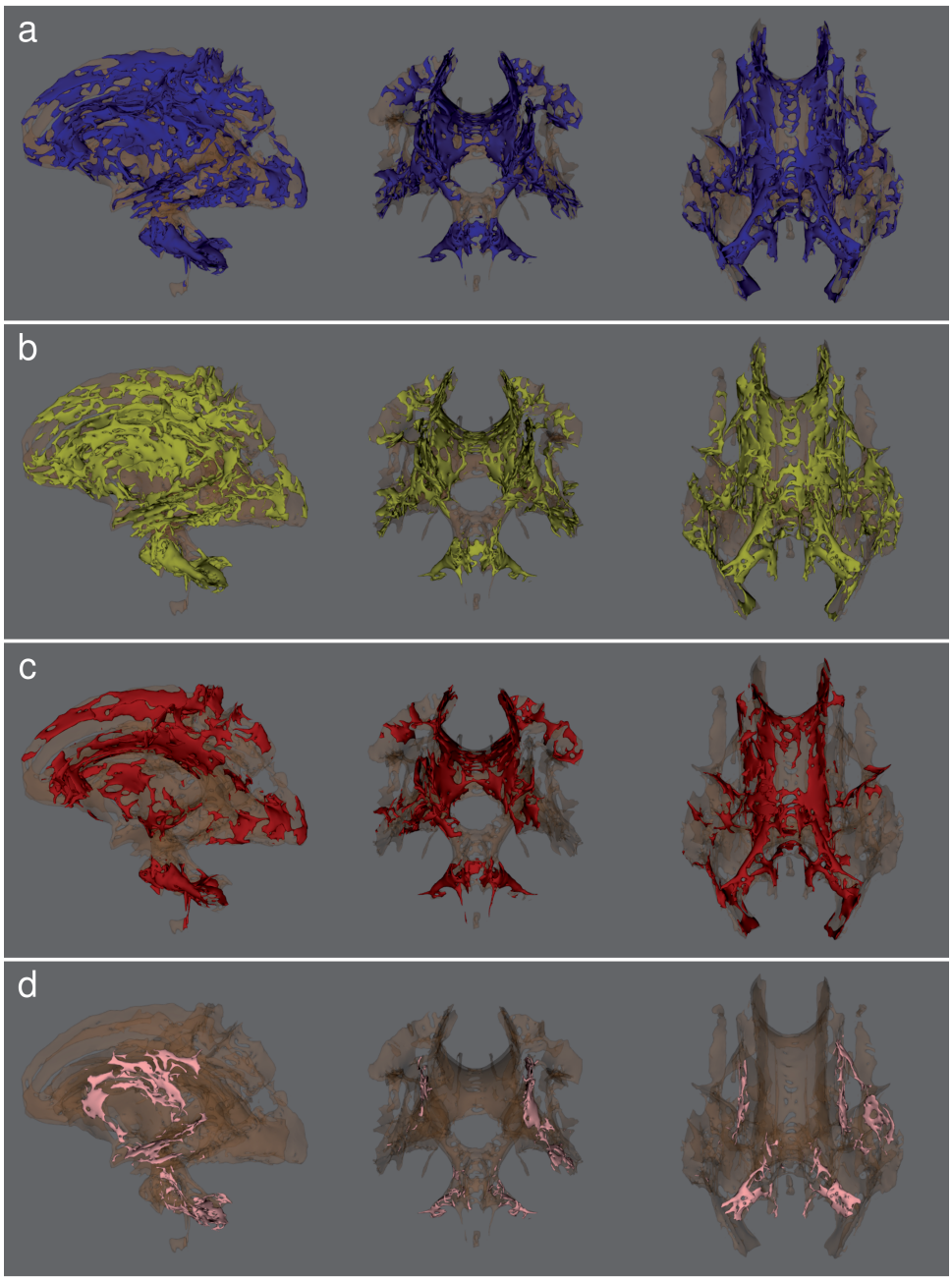
In examining differences between all MSA and control subjects reported by TBSS, we observed widespread differences in RD and MD, with changes in FA and AD following but in fewer voxels (Figure 4.16). RD and MD were increased and FA reduced in the superior cerebellar peduncles (SCP), middle cerebellar peduncles (MCP) and inferior cerebellar peduncles (ICP) bilaterally (Figure 4.16a-c), with a smaller volume of increased AD in the bilateral MCP and ICP (Figure 4.16d). No differences in AD between patients and controls were observed in the SCP.

Changes in RD and MD were also more widespread supratentorially, being increased throughout the corona radiata and commissural fibers bilaterally, in the body and genu of the corpus callosum in the midline, and in many subcortical areas, primarily frontal (Figure 4.16a,b). RD and MD were also increased in the internal and external capsules bilaterally, including parts of the bilateral CST. Supratentorially, reduced FA followed a similar pattern but was observed in fewer voxels, with no differences detected in the left temporal subcortical white matter (Figure 4.16c). Increased AD was primarily observed in a small number of voxels in the more central portions of the corona radiata and in the left external capsule (Figure 4.16d). These voxels generally demonstrated increased RD and MD, but no changes in FA.

We further explored differences between controls and the MSA-P and MSA-C diagnostic subgroups by TBSS. In MSA-P, only supratentorial differences were observed in comparison with controls (Figure 4.17), following a similar pattern as in all MSA patients versus controls, but in fewer voxels. RD and MD were again increased throughout the corona radiata and the internal capsules bilaterally, in the body of the corpus callosum and in a number of subcortical regions (Figure 4.17a,b). No changes in MD were observed in the subcortical white matter of the bilateral occipital lobes (Figure 4.17b). Decreased FA was detected in the body of the corpus callosum, in the rostral commissural fibers

Figure 4.16: TBSS results: voxels demonstrating significant ($P < 0.05$) differences between all patients and controls. a) Radial diffusivity (patients > controls), b) mean diffusivity (patients > controls), c) fractional anisotropy (patients < controls), and d) axial diffusivity (patients > controls). TBSS, tract-based spatial statistics; MSA, multiple system atrophy.

Figure 4.16: (continued)



bilaterally, in the right genu of the internal capsule, in the bilateral corona radiata, and in the frontal subcortical white matter, primarily on the right (Figure 4.17c). Differences in AD were similar to all MSA versus controls, occurring primarily in the left hemisphere (Figure 4.17d).

In MSA-C, differences were again similar to those detected between all MSA subjects and controls (Figure 4.18). RD, MD and AD were increased and FA decreased in the SCP, MCP, and ICP bilaterally, with RD and MD differences present in the greatest number of voxels, and AD differences in the fewest (Figure 4.18a-d). Supratentorial differences in RD and MD were similar to those between all MSA subjects and controls, however subcortical white matter differences were primarily frontal (Figure 4.18a,b). FA again followed a similar pattern but in fewer voxels. Notably, no FA differences were detected in the left internal and bilateral external capsules and subcortical differences were limited to the frontal white matter (Figure 4.18c). Supratentorial differences in AD were limited to the right corona radiata (Figure 4.18d). No differences were detected between the MSA-C and MSA-P diagnostic subgroups (Figure 4.19).

Figure 4.17: TBSS results: voxels demonstrating significant ($P < 0.05$) differences between all MSA-P patients and controls. a) Radial diffusivity (patients > controls), b) mean diffusivity (patients > controls), c) fractional anisotropy (patients < controls) and d) axial diffusivity (patients > controls). TBSS, tract-based spatial statistics; MSA-P, multiple system atropy, traditional parkinsonian subtype.

Figure 4.17: (continued)

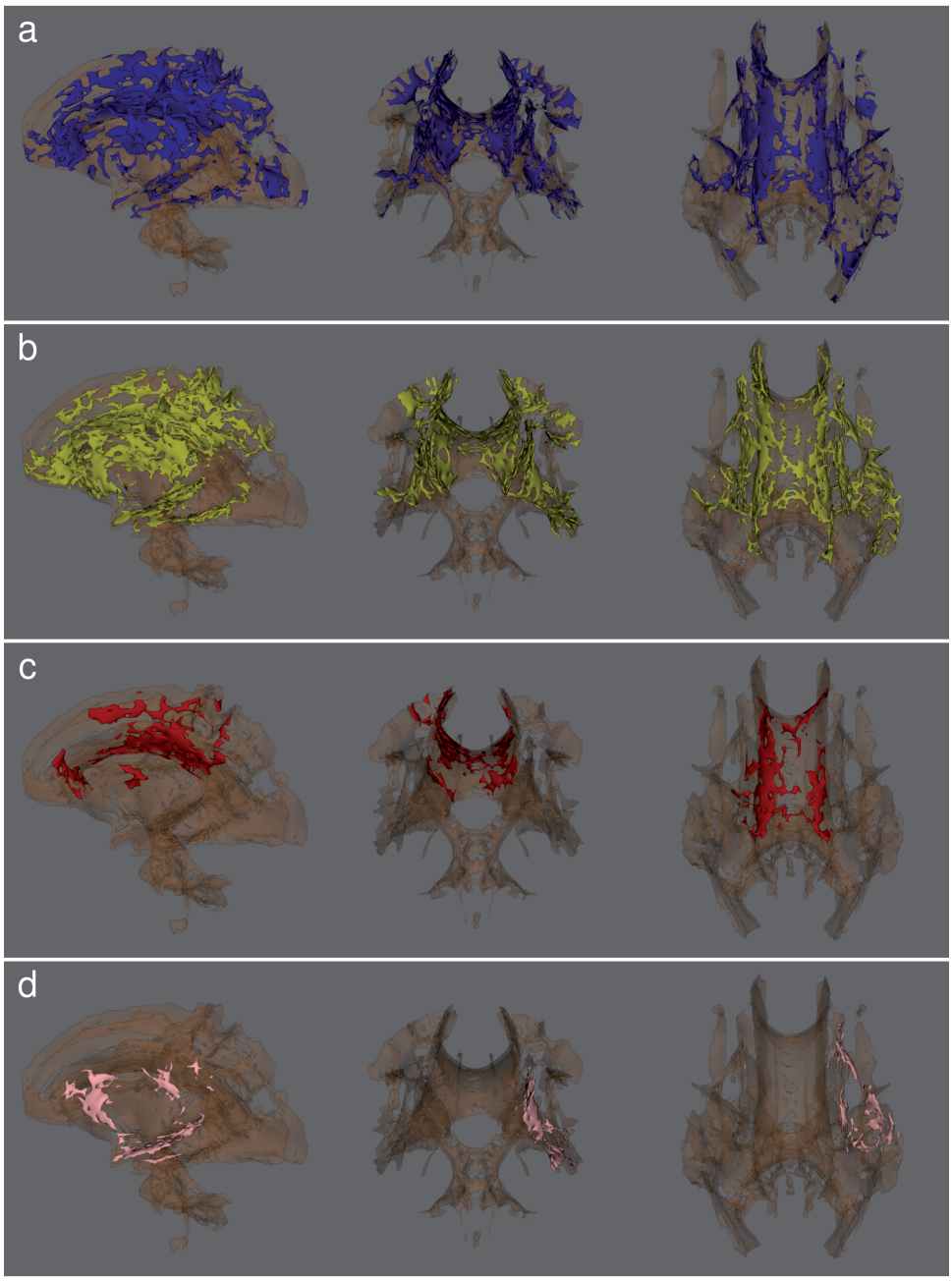


Figure 4.18: TBSS results: voxels demonstrating significant ($P < 0.05$) differences between all MSA-C patients and controls. a) Radial diffusivity (patients > controls), b) mean diffusivity (patients > controls), c) fractional anisotropy (patients < controls) and d) axial diffusivity (patients > controls). TBSS, tract-based spatial statistics; MSA-C, multiple system atrophy, traditional cerebellar subtype.

Figure 4.18: (continued)

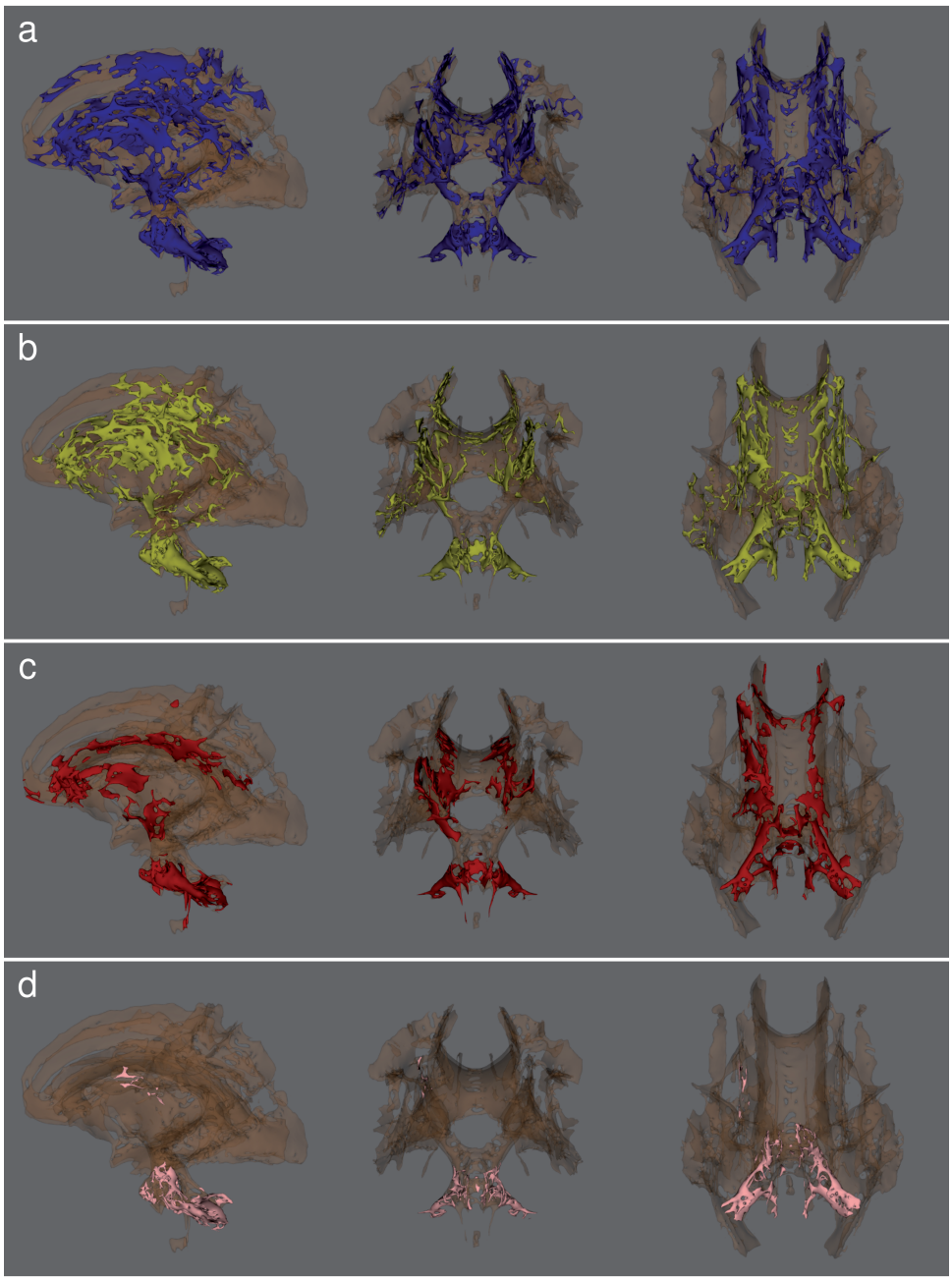
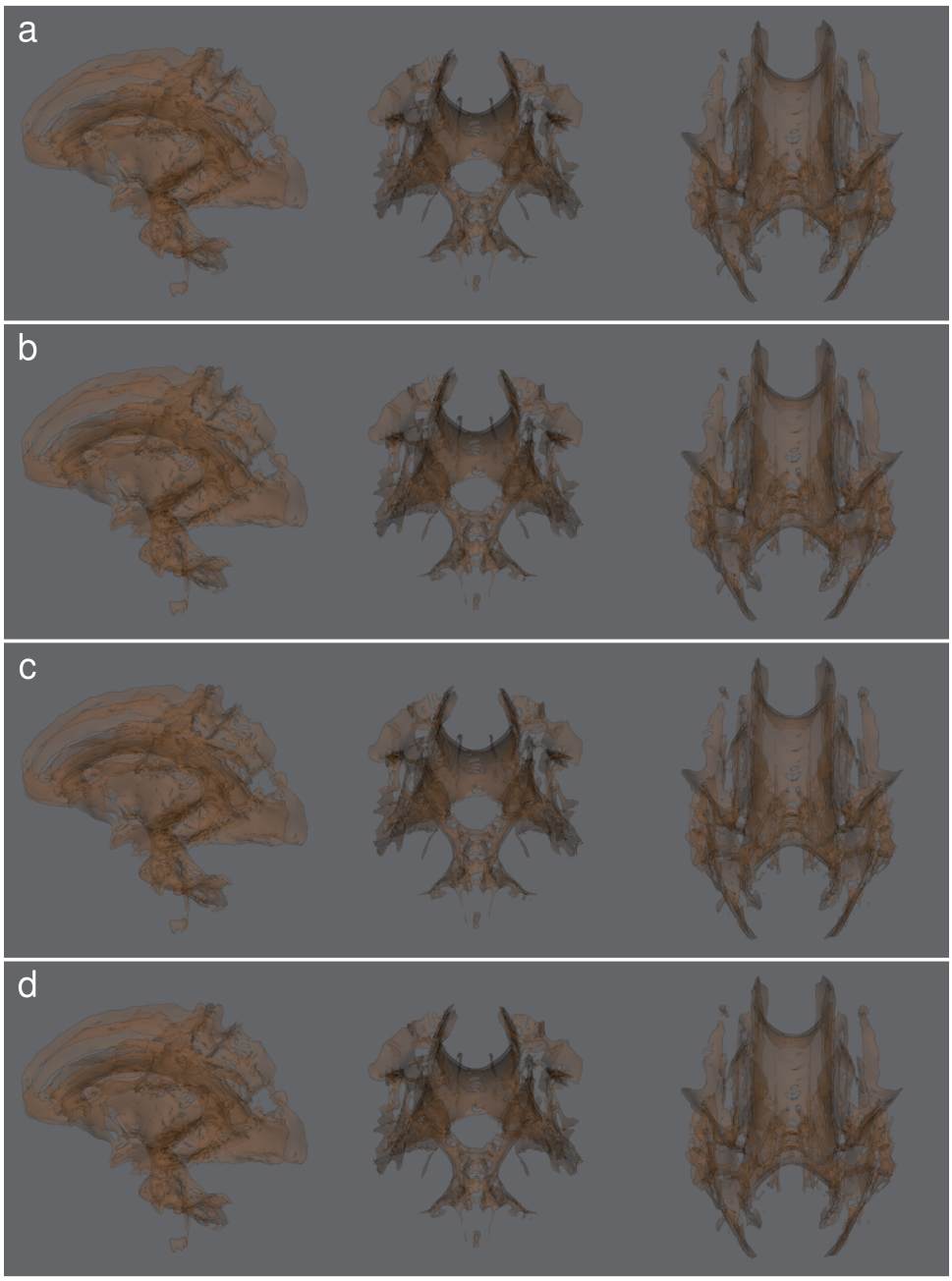


Figure 4.19: TBSS results: no significant ($P < 0.05$) differences detected between all MSA-C and MSA-P patients. a) Radial diffusivity, b) mean diffusivity, c) fractional anisotropy and d) axial diffusivity. TBSS, tract-based spatial statistics; MSA-C, multiple system atrophy, traditional cerebellar subtype; MSA-P, multiple system atrophy, traditional parkinsonian subtype.

Figure 4.19: (continued)



Considering the surprising result that no differences between the MSA-C and MSA-P diagnostic subgroups were detected by TBSS (Figure 4.19), we hypothesized that this negative result may be due to overlap between the patient groups. To explore this possibility further, the MSA group was reclassified according to phenotype into three subgroups: cMSA (cerebellar positive), pMSA (parkinsonian positive), and mMSA (mixed, both cerebellar and parkinsonian positive). Those subjects in the mMSA subgroup exhibited both cerebellar and parkinsonian signs, whereas those in the cMSA or pMSA groups exhibited only cerebellar or parkinsonian signs, respectively. After reclassification, further TBSS analyses were conducted between the cMSA group and controls, between the pMSA group and controls, and between the cMSA and pMSA groups. In the cMSA group, we observed widespread changes supratentorially in RD and MD similar to all MSA patients versus controls (Figure 4.20a,b), with changes in FA only present in the corona radiata on the left (Figure 4.20c). There were no supratentorial differences in AD (Figure 4.20d). Infratentorially, changes in RD and MD were present in the SCP, MCP and ICP (Figure 4.20a,b), changes in FA in the MCP and ICP bilaterally and in the SCP on the right (Figure 4.20c), and changes in AD in the bilateral MCP only (Figure 4.20d). No differences between pMSA and controls were detected by TBSS (Figure 4.21). In examining TBSS results between cMSA and pMSA patients, differences were detected primarily infratentorially in RD and MD in the SCP, MCP and ICP bilaterally (Figure 4.22a,b). Differences in AD were detected in the bilateral MCP only (Figure 4.22d). Supratentorially, only subtle differences were detected in the PLIC and corticospinal tract in RD on the left (Figure 4.22a), and in MD in the para-medial coronal fibers on the left (Figure 4.22b). No significant differences in FA were detected either supra- or infratentorially (Figure 4.22c). No supratentorial differences in AD were detected (Figure 4.22d).

Figure 4.20: TBSS results: voxels demonstrating significant ($P < 0.05$) differences between all cerebellar-positive, parkinsonian-negative MSA patients (cMSA) and controls. a) Radial diffusivity (patients $>$ controls), b) mean diffusivity (patients $>$ controls), c) fractional anisotropy (patients $<$ controls) and d) axial diffusivity (patients $>$ controls). TBSS, tract-based spatial statistics; MSA, multiple system atrophy.

Figure 4.20: (continued)

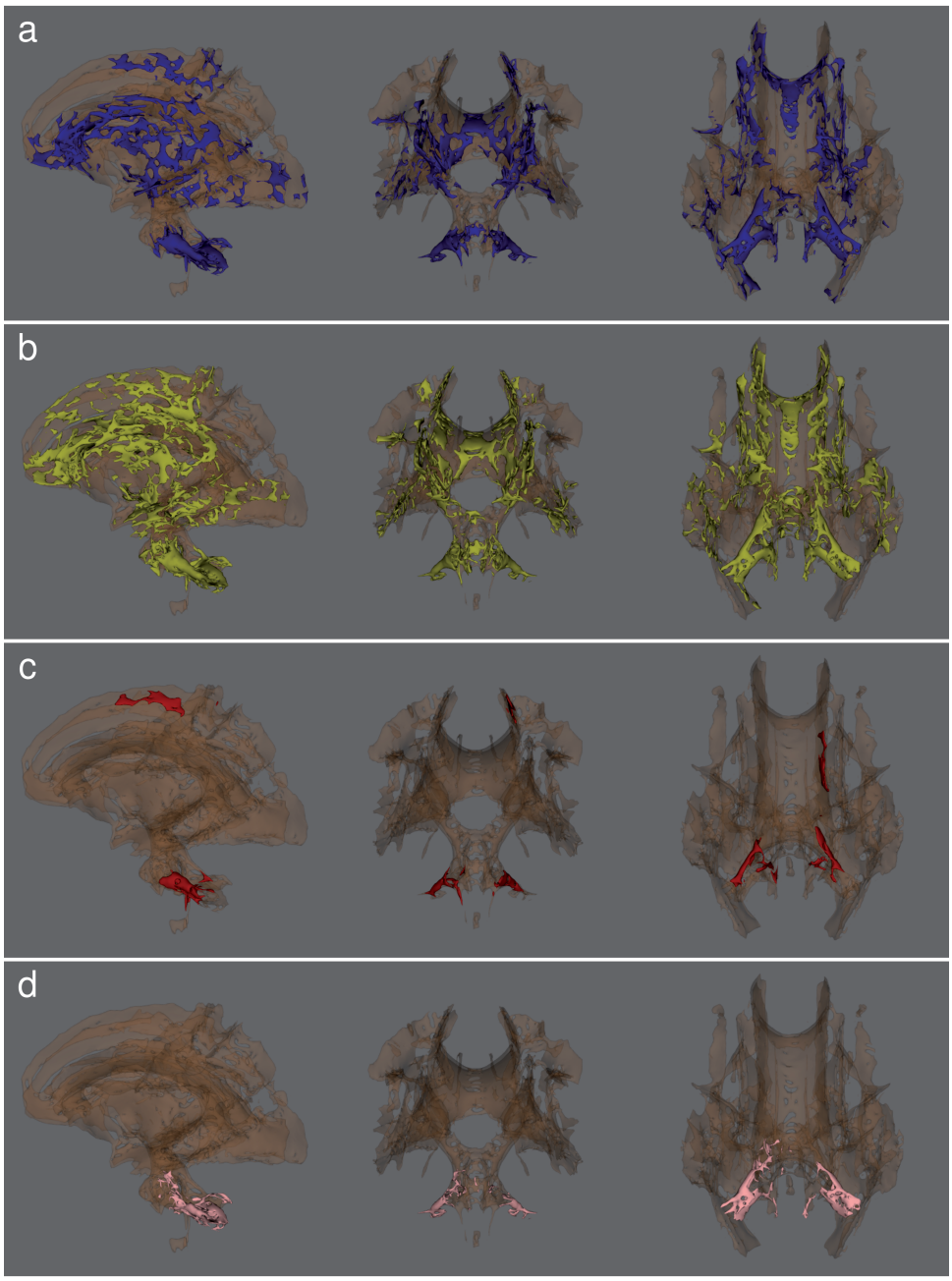


Figure 4.21: TBSS results: no significant ($P < 0.05$) differences detected between all parkinsonian-positive, cerebellar-negative MSA patients (pMSA) and controls. a) Radial diffusivity, b) mean diffusivity, c) fractional anisotropy and d) axial diffusivity. TBSS, tract-based spatial statistics; MSA, multiple system atrophy.

Figure 4.21: (continued)

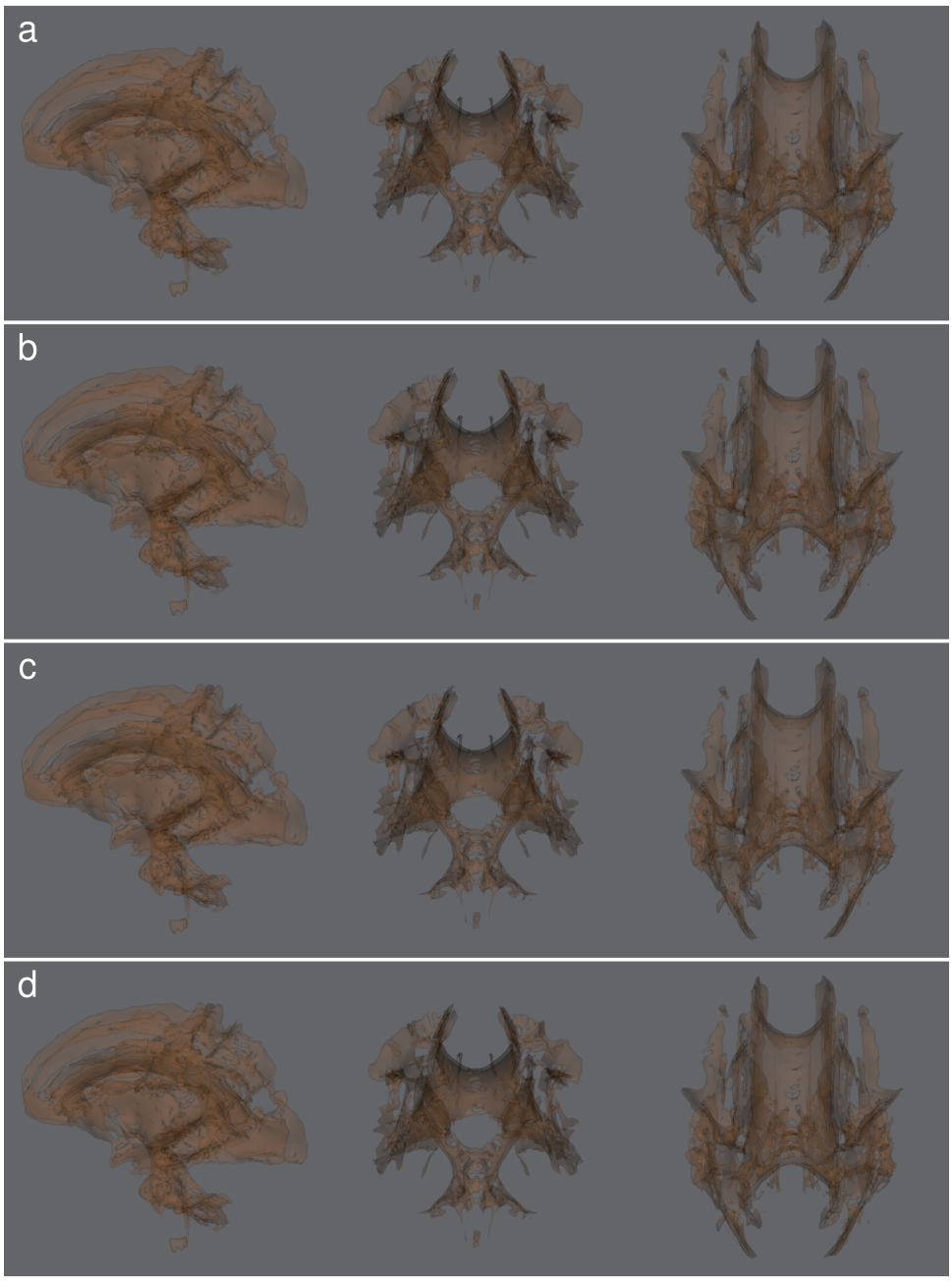
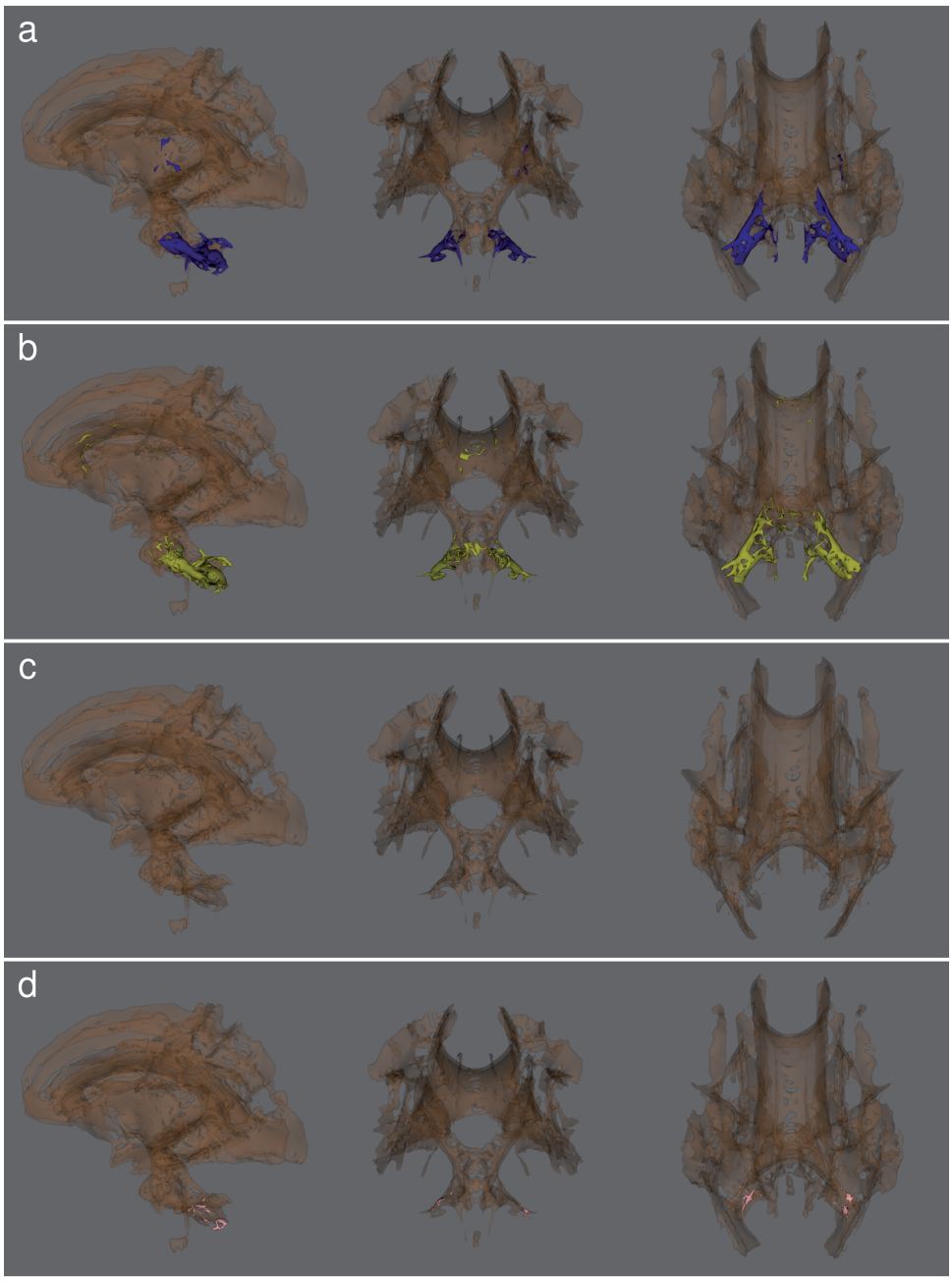


Figure 4.22: TBSS results: voxels demonstrating significant ($P < 0.05$) differences between all cerebellar-positive, parkinsonian-negative MSA patients (cMSA) and parkinsonian-positive, cerebellar-negative MSA patients (pMSA). a) Radial diffusivity (cMSA $>$ pMSA), b) fractional anisotropy, C) mean diffusivity (cMSA $>$ pMSA) and D) axial diffusivity (cMSA $>$ pMSA). TBSS, tract-based spatial statistics; MSA, multiple system atrophy.

Figure 4.22: (continued)



We further explored the DTI characteristics in the basal ganglia (caudate nucleus, putamen, globus pallidus) of MSA and control subjects, additionally adding $\lambda 3$ to the analysis. The addition of $\lambda 3$ was made to help characterize any changes in diffusion metrics observed [104]. Adjustment for multiple comparisons was made as described in Methods. We first investigated differences in laterality in the basal ganglia in the stated diffusion metrics, and found that FA in the caudate nucleus differed between the left and right side ($P = 0.002$). Therefore, we elected to analyze the left and right sides separately. We then explored group differences using a one-way analysis of variance (ANOVA) test, followed by the Tukey-Kramer procedure in those regions and metrics that reached significance. These tests were performed using different patient classifications: between the traditional MSA subgroups (MSA-C, MSA-P) and controls (traditional), between parkinsonian-positive MSA subjects (pPOS), and between parkinsonian-negative MSA subjects (pNEG) and controls (phenotypic). The data were reclassified in an attempt to improve the classification ability and diagnostic utility of DTI in MSA, as we expected that patients with parkinsonian manifestations would likely have detectable changes in diffusion indices in the basal ganglia, while those without parkinsonian manifestations would likely not. We found significant differences in the bilateral putamen only, in $\lambda 1$, $\lambda 3$, MD and RD (see Table 4.2). No differences in FA in the putamen were detected. ROC analyses in those metrics reaching significance indicated that $\lambda 1$ and MD provide the best potential classification ability in the bilateral putamen under both patient classifications (Table 4.3). Reclassification of the data by phenotype resulted in generally greater area between the two ROC curves, (see Table 4.3, Figures 4.23-4.30).

Table 4.2: ANOVA results in the bilateral putamen

Traditional				Phenotypic			
Side	Metric	F-value	P-value	Side	Metric	F-value	P-value
L	FA	$F(2,37) = 2.7185$	$P = 0.82$	L	FA	$F(2,37) = 1.6619$	$P = 0.99$
L	$\lambda 1$	$F(2,37) = 12.636$	$P = 0.001$	L	$\lambda 1$	$F(2,37) = 10.364$	$P = 0.006$
L	$\lambda 3$	$F(2,37) = 9.3191$	$P = 0.011$	L	$\lambda 3$	$F(2,37) = 8.4826$	$P = 0.019$
L	MD	$F(2,37) = 11.674$	$P = 0.002$	L	MD	$F(2,37) = 9.9842$	$P = 0.007$
L	RD	$F(2,37) = 10.575$	$P = 0.005$	L	RD	$F(2,37) = 9.3218$	$P = 0.011$
R	FA	$F(2,37) = 2.0814$	$P = 0.96$	R	FA	$F(2,37) = 0.2823$	$P = 0.99$
R	$\lambda 1$	$F(2,37) = 15.833$	$P < 0.001$	R	$\lambda 1$	$F(2,37) = 12.451$	$P = 0.002$
R	$\lambda 3$	$F(2,37) = 11.688$	$P = 0.002$	R	$\lambda 3$	$F(2,37) = 10.993$	$P = 0.004$
R	MD	$F(2,37) = 14.196$	$P < 0.001$	R	MD	$F(2,37) = 12.153$	$P = 0.002$
R	RD	$F(2,37) = 12.786$	$P = 0.001$	R	RD	$F(2,37) = 11.543$	$P = 0.003$

Table 4.2: Results of ANOVA analyses of ROI data in the bilateral putamen. L, left; R, right; FA, fractional anisotropy; MD, mean diffusivity; RD, radial diffusivity

Table 4.3: ROC results in the bilateral putamen

Traditional				Phenotypic			
		AUC				AUC	
Side	Metric	Con vs MSA-C	Con vs MSA-P	Side	Metric	Con vs pNEG	Con vs pPOS
L	$\lambda 1$	0.75	0.95	L	$\lambda 1$	0.61	0.90
L	$\lambda 3$	0.74	0.82	L	$\lambda 3$	0.51	0.84
L	MD	0.78	0.93	L	MD	0.62	0.92
L	RD	0.80	0.89	L	RD	0.64	0.90
R	$\lambda 1$	0.87	0.92	R	$\lambda 1$	0.85	0.90
R	$\lambda 3$	0.86	0.87	R	$\lambda 3$	0.79	0.88
R	MD	0.87	0.90	R	MD	0.82	0.90
R	RD	0.87	0.87	R	RD	0.82	0.88

Table 4.3: Results of ROC analyses of ROI data in the bilateral putamen between patients and controls. AUC, area under curve; MSA-C, multiple system atrophy, traditional cerebellar subtype; MSA-P multiple system atrophy, traditional parkinsonian subtype; pNEG, parkinsonian-negative; pPOS, parkinsonian-positive; L, left; R, right; MD, mean diffusivity; RD, radial diffusivity.

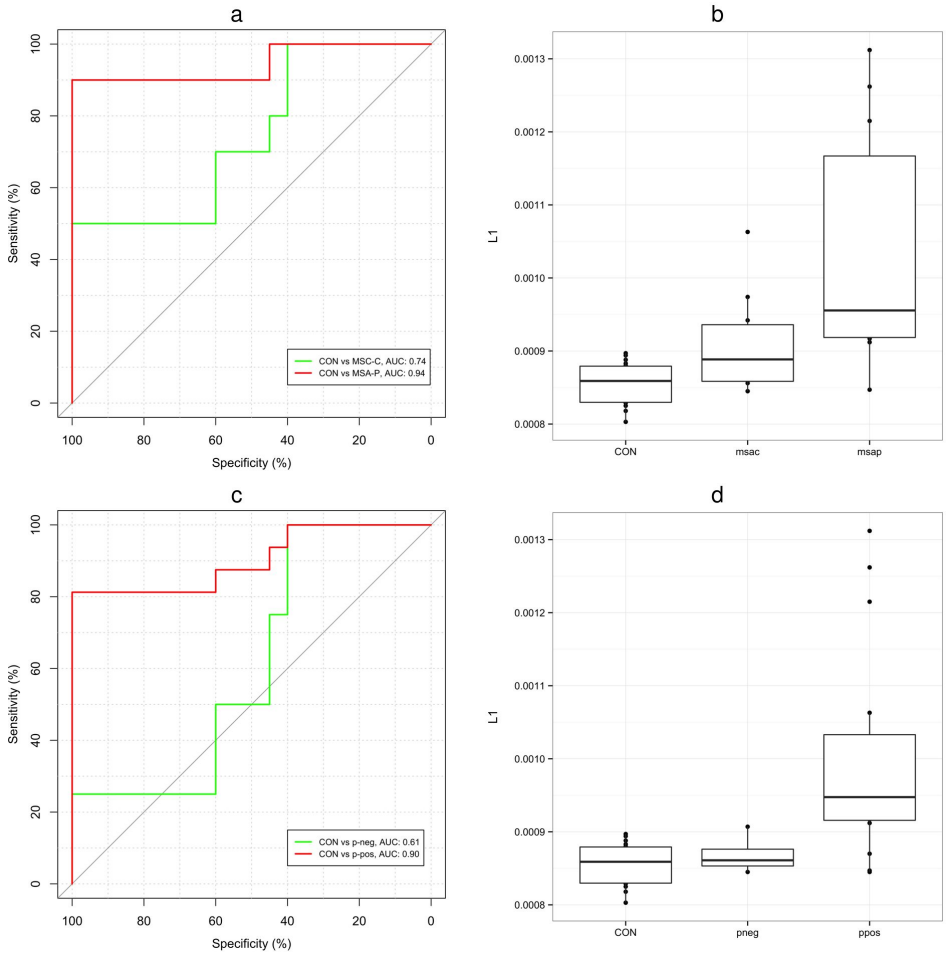


Figure 4.23: ROC results in the left putamen between patients and controls in $\lambda 1$: a) ROC curves between traditional MSA subgroups and controls, b) boxplot representation of the same data, c) ROC curves between phenotypic MSA subgroups and controls, d) boxplot representation of the same data.

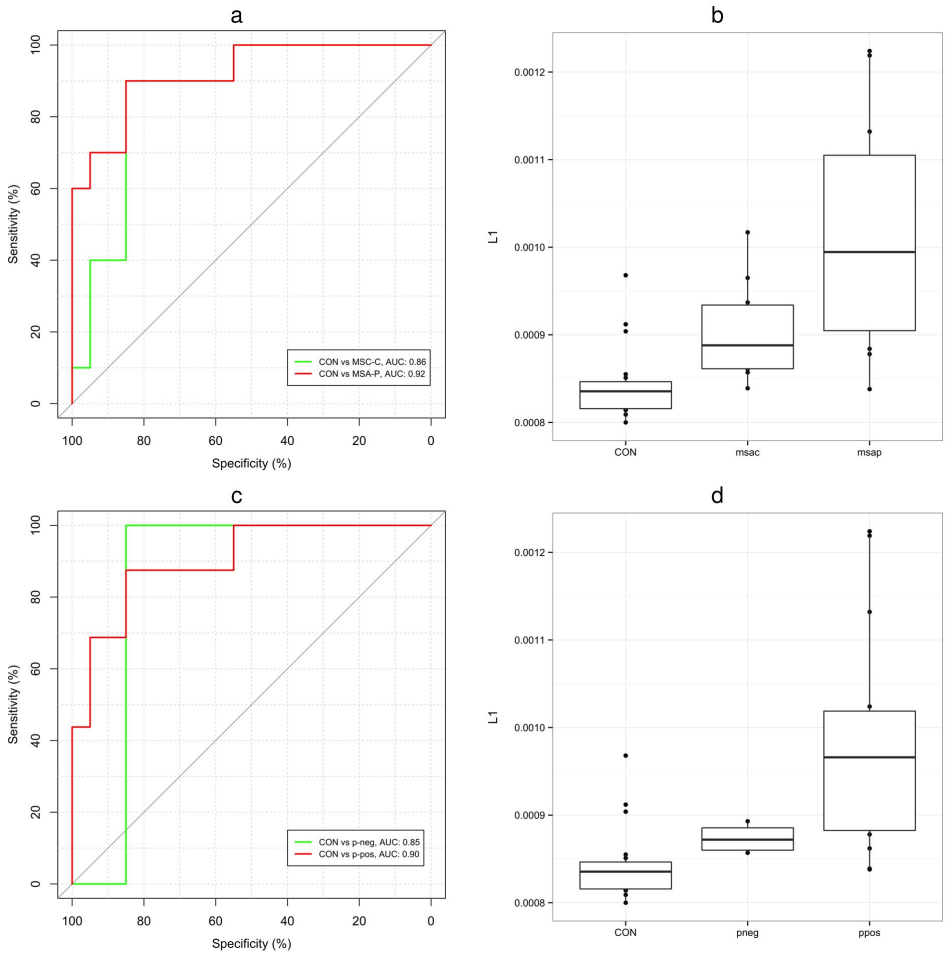


Figure 4.24: ROC results in the right putamen between patients and controls in $\lambda 1$: a) ROC curves between traditional MSA subgroups and controls, b) boxplot representation of the same data, c) ROC curves between phenotypic MSA subgroups and controls, d) boxplot representation of the same data.

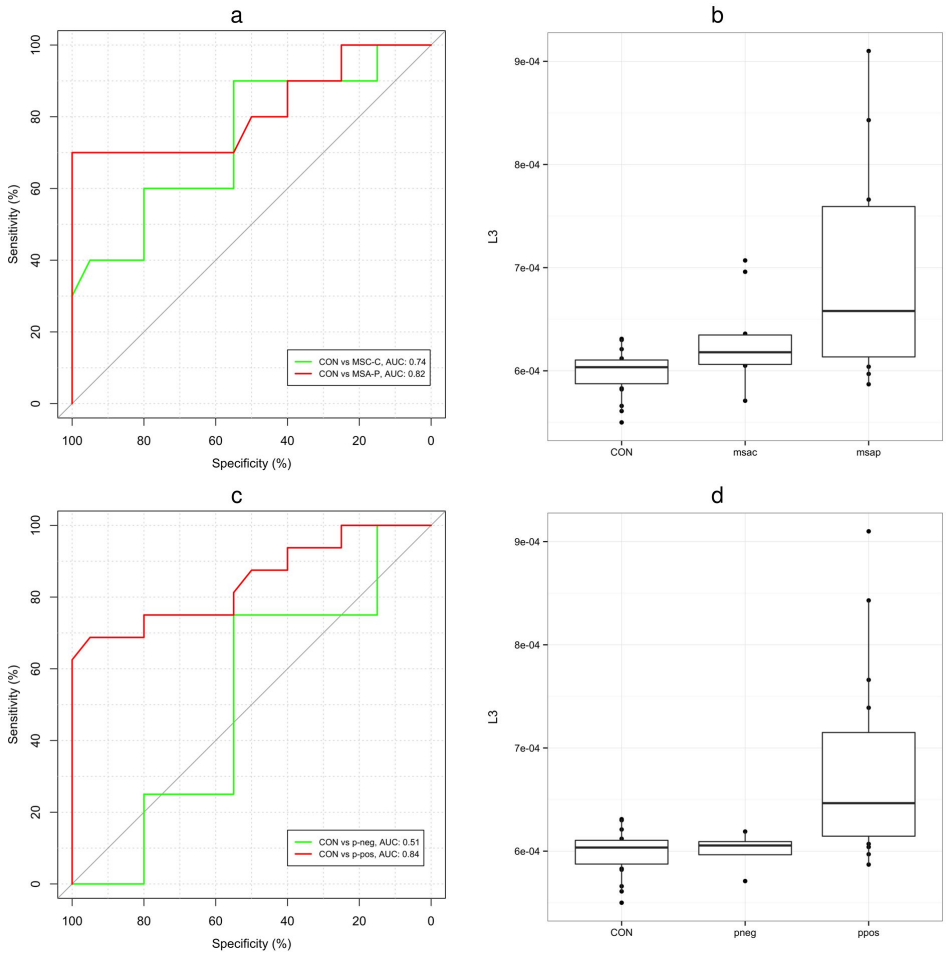


Figure 4.25: ROC results in the left putamen between patients and controls in $\lambda 3$: a) ROC curves between traditional MSA subgroups and controls, b) boxplot representation of the same data, c) ROC curves between phenotypic MSA subgroups and controls, d) boxplot representation of the same data.

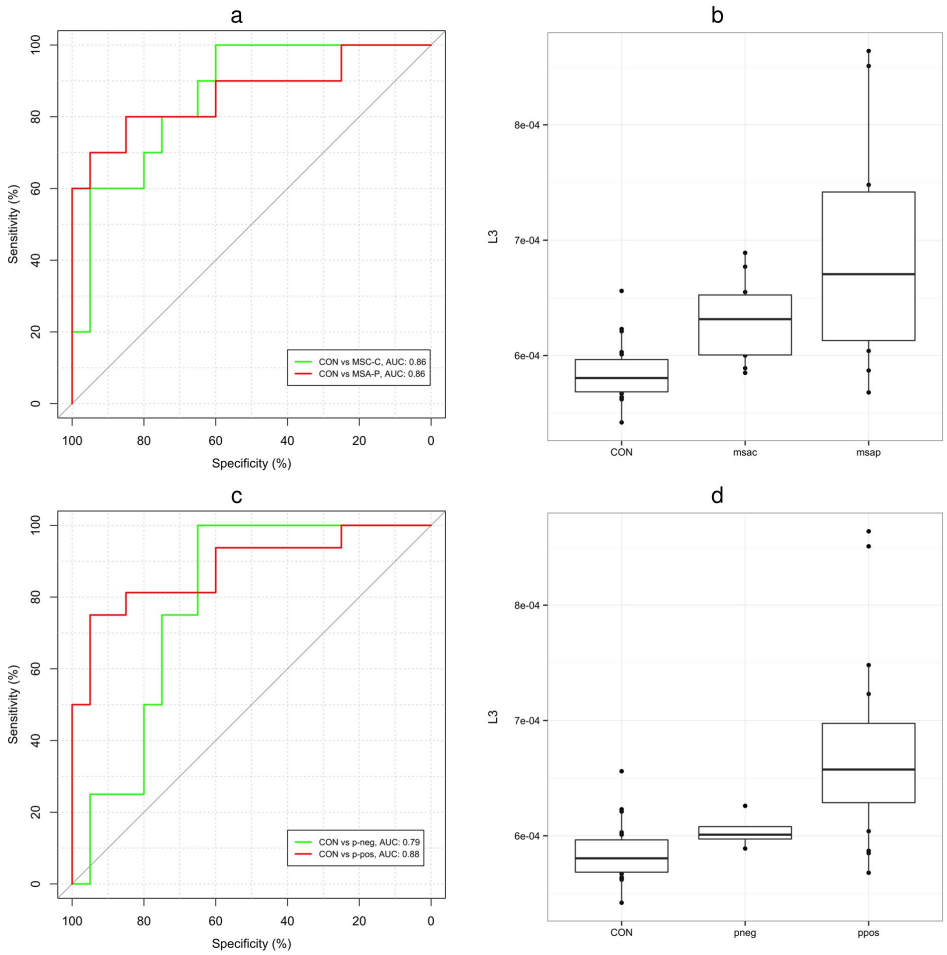


Figure 4.26: ROC results in the right putamen between patients and controls in $\lambda 3$: a) ROC curves between traditional MSA subgroups and controls, b) boxplot representation of the same data, c) ROC curves between phenotypic MSA subgroups and controls, d) boxplot representation of the same data.

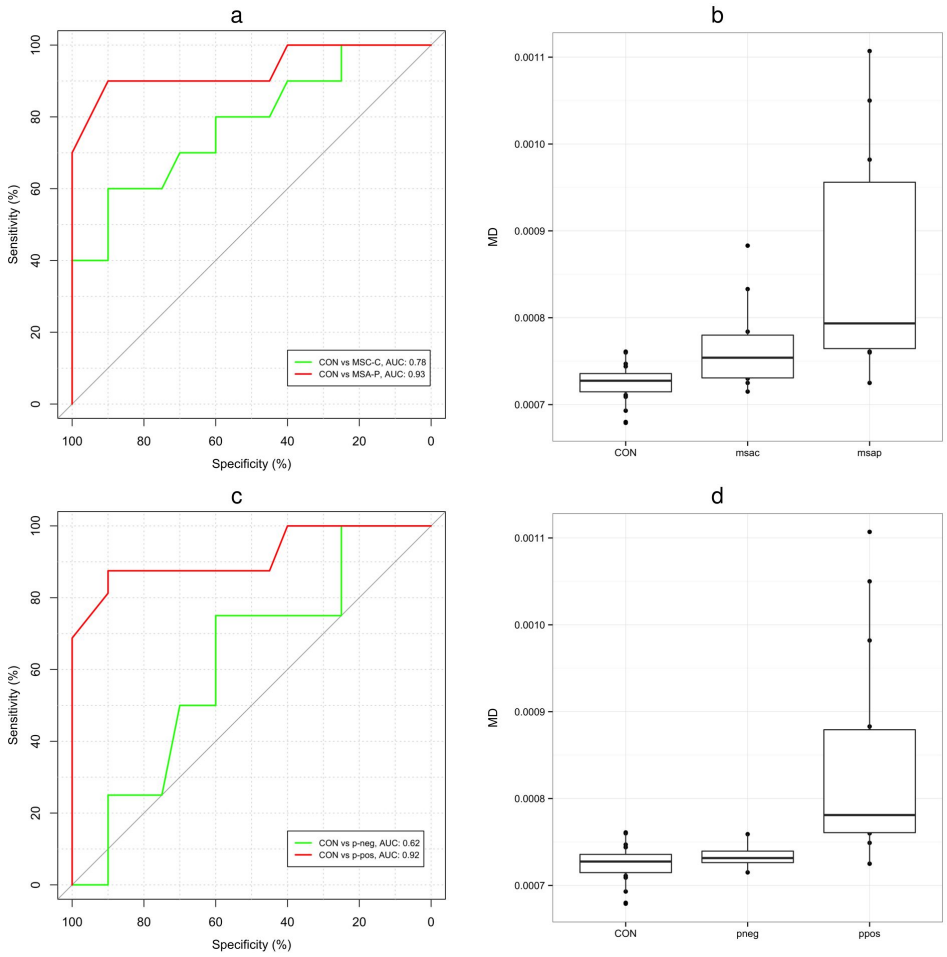


Figure 4.27: ROC results in the left putamen between patients and controls in MD: a) ROC curves between traditional MSA subgroups and controls, b) boxplot representation of the same data, c) ROC curves between phenotypic MSA subgroups and controls, d) boxplot representation of the same data. MD, mean diffusivity.

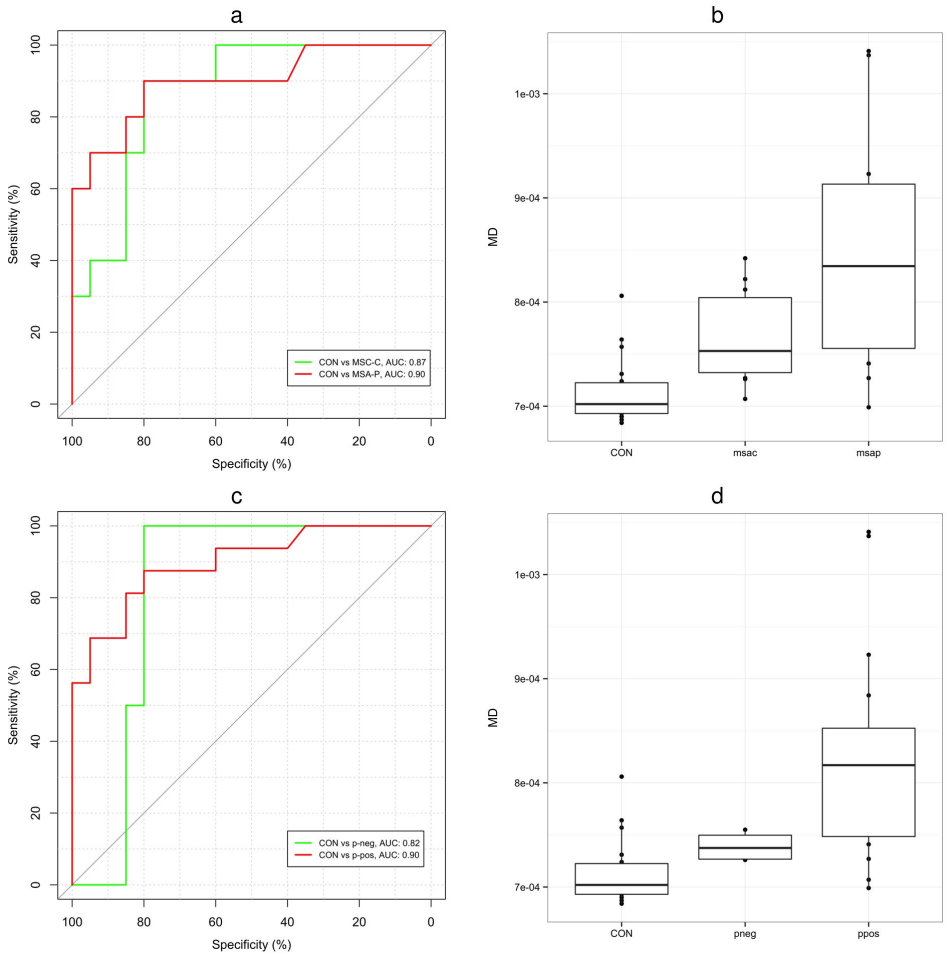


Figure 4.28: ROC results in the right putamen between patients and controls in MD: a) ROC curves between traditional MSA subgroups and controls, b) boxplot representation of the same data, c) ROC curves between phenotypic MSA subgroups and controls, d) boxplot representation of the same data. MD, mean diffusivity.

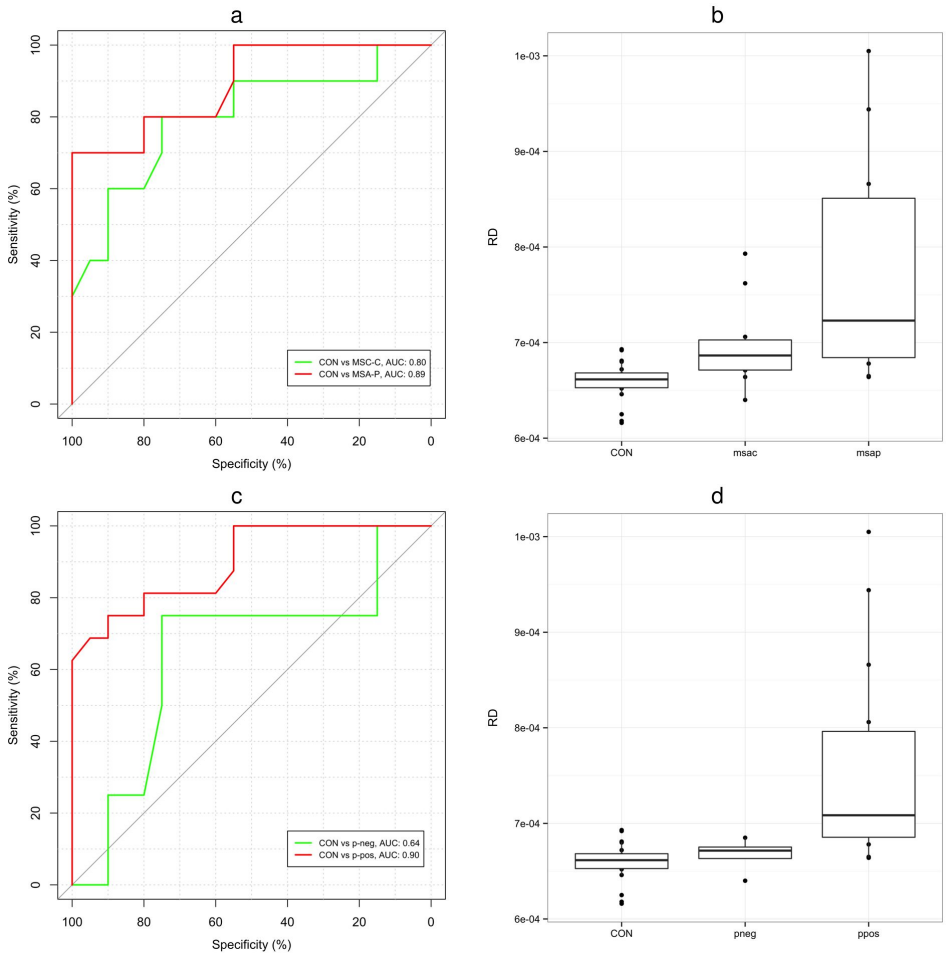


Figure 4.29: ROC results in the left putamen between patients and controls in RD: a) ROC curves between traditional MSA subgroups and controls, b) boxplot representation of the same data, c) ROC curves between phenotypic MSA subgroups and controls, d) boxplot representation of the same data. RD, radial diffusivity.

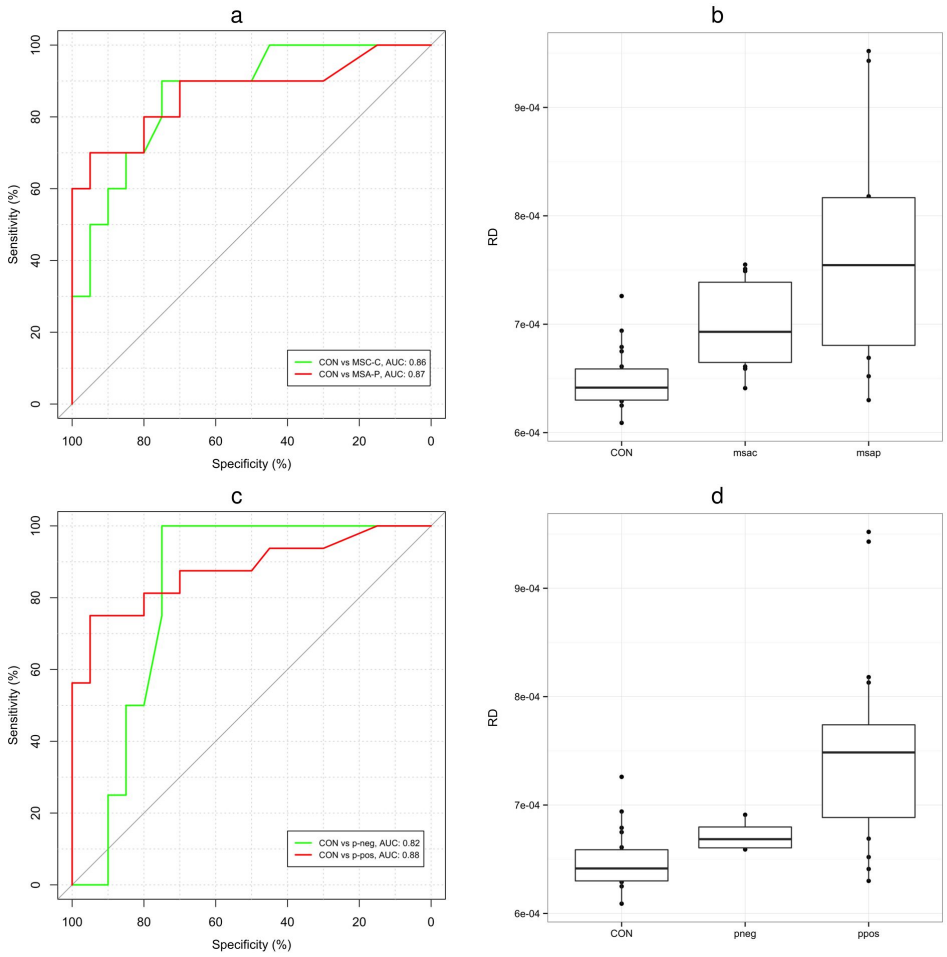


Figure 4.30: ROC results in the right putamen between patients and controls in RD: a) ROC curves between traditional MSA subgroups and controls, b) boxplot representation of the same data, c) ROC curves between phenotypic MSA subgroups and controls, d) boxplot representation of the same data. RD, radial diffusivity.

We also performed ROC analyses in the MCP to further explore the diagnostic utility of DTI in this region. Two patient classifications were again used: between the traditional MSA subgroups (MSA-C, MSA-P) and controls (traditional), and between cerebellar-positive MSA subjects (cPOS) and controls and cerebellar-negative MSA subjects (cNEG) and controls (phenotypic). The reclassification of patients according to phenotype was again performed due to phenotypical overlap between the traditional MSA subgroups, in an effort to improve the classification ability of DTI in this region. Reclassification of the data by phenotype again resulted in generally greater area between the two ROC curves (see Table 4.4, Figures 4.31-4.34).

Table 4.4: ROC results in the MCP

Traditional				Phenotypic			
		AUC				AUC	
Side	Metric	Con vs MSA-C	Con vs MSA-P	Side	Metric	Con vs cPOS	Con vs cNEG
L	RD	0.96	0.77	L	RD	0.97	0.61
L	MD	0.92	0.78	L	MD	0.94	0.63
L	FA	0.97	0.75	L	FA	0.98	0.58
L	$\lambda 1$	0.87	0.73	L	$\lambda 1$	0.85	0.68

Table 4.4: Results of ROC analyses of ROI data in the bilateral MCP between patients and controls. AUC, area under curve; MSA-C, multiple system atrophy, cerebellar subtype; MSA-P multiple system atrophy, parkinsonian subtype; cPOS, cerebellar-positive MSA; cNEG, cerebellar-negative MSA; L, left; R, right; RD, radial diffusivity; MD, mean diffusivity; FA, fractional anisotropy.

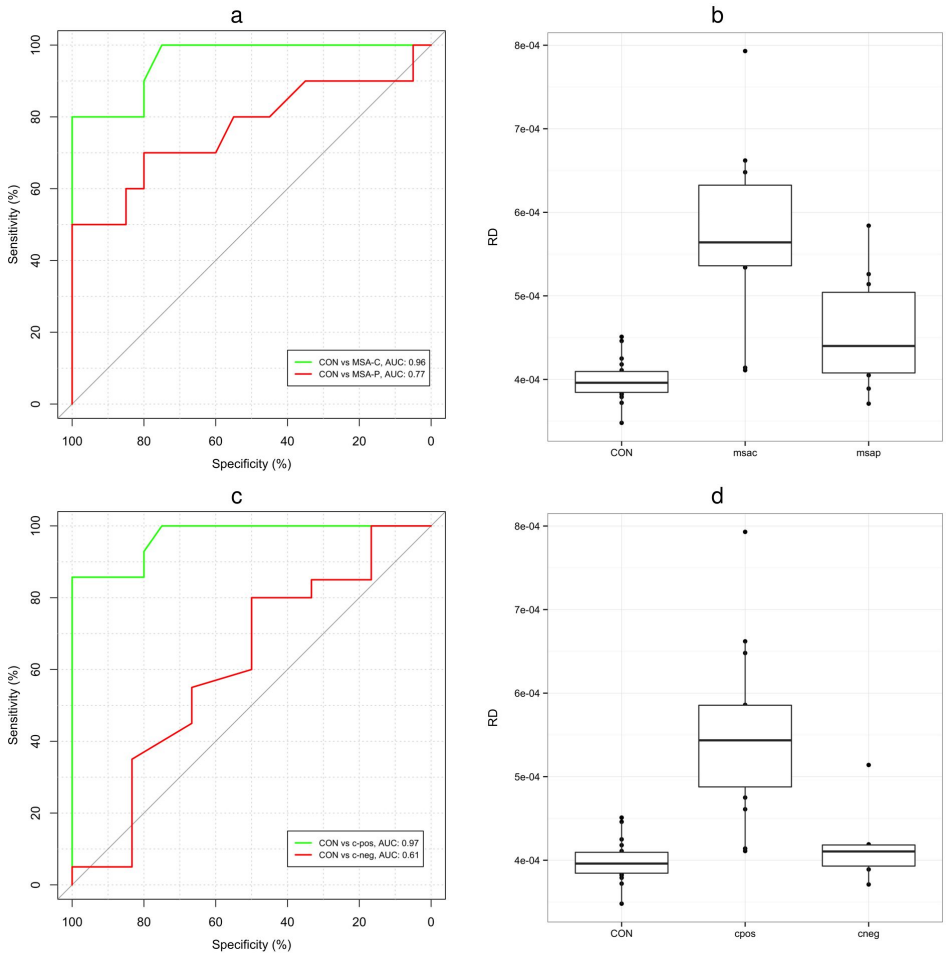


Figure 4.31: ROC results in the MCP between patients and controls in RD: a) ROC curves between traditional MSA subgroups and controls, b) boxplot representation of the same data, c) ROC curves between phenotypic MSA subgroups and controls, d) boxplot representation of the same data. MCP, middle cerebellar peduncle; RD, radial diffusivity.

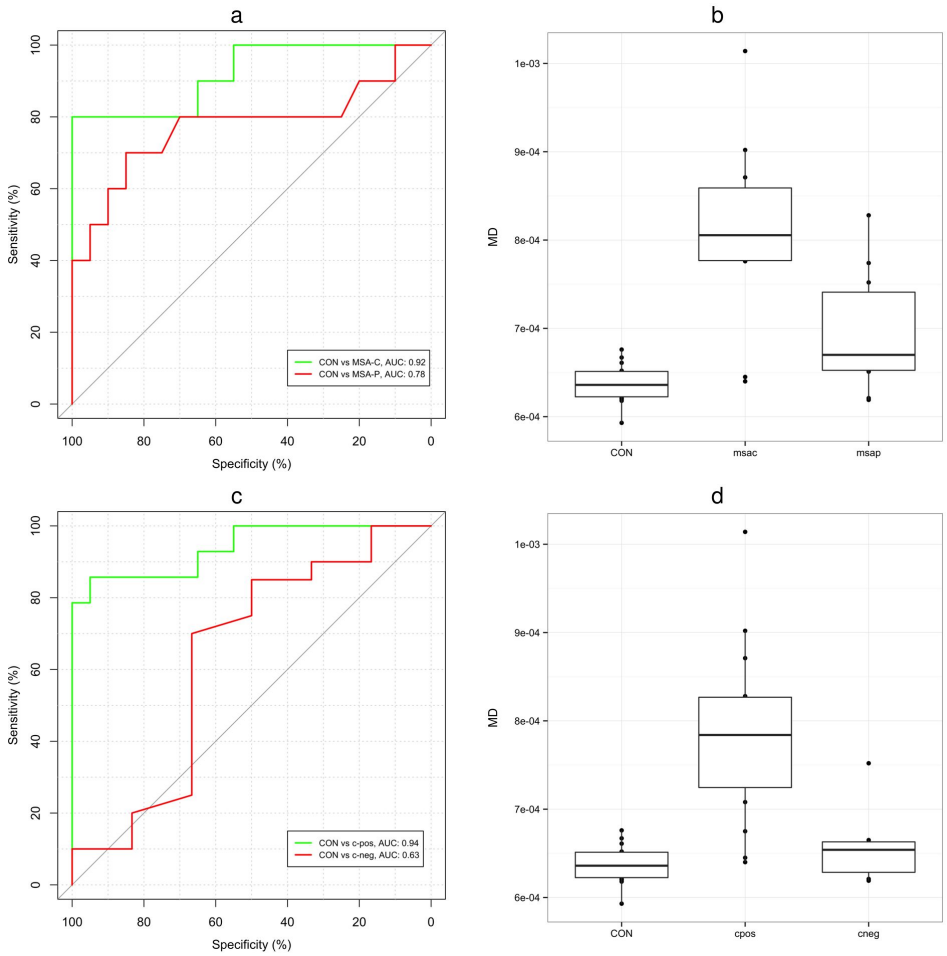


Figure 4.32: ROC results in the MCP between patients and controls in MD: a) ROC curves between traditional MSA subgroups and controls, b) boxplot representation of the same data, c) ROC curves between phenotypic MSA subgroups and controls, d) boxplot representation of the same data. MCP, middle cerebellar peduncle; MD, mean diffusivity.

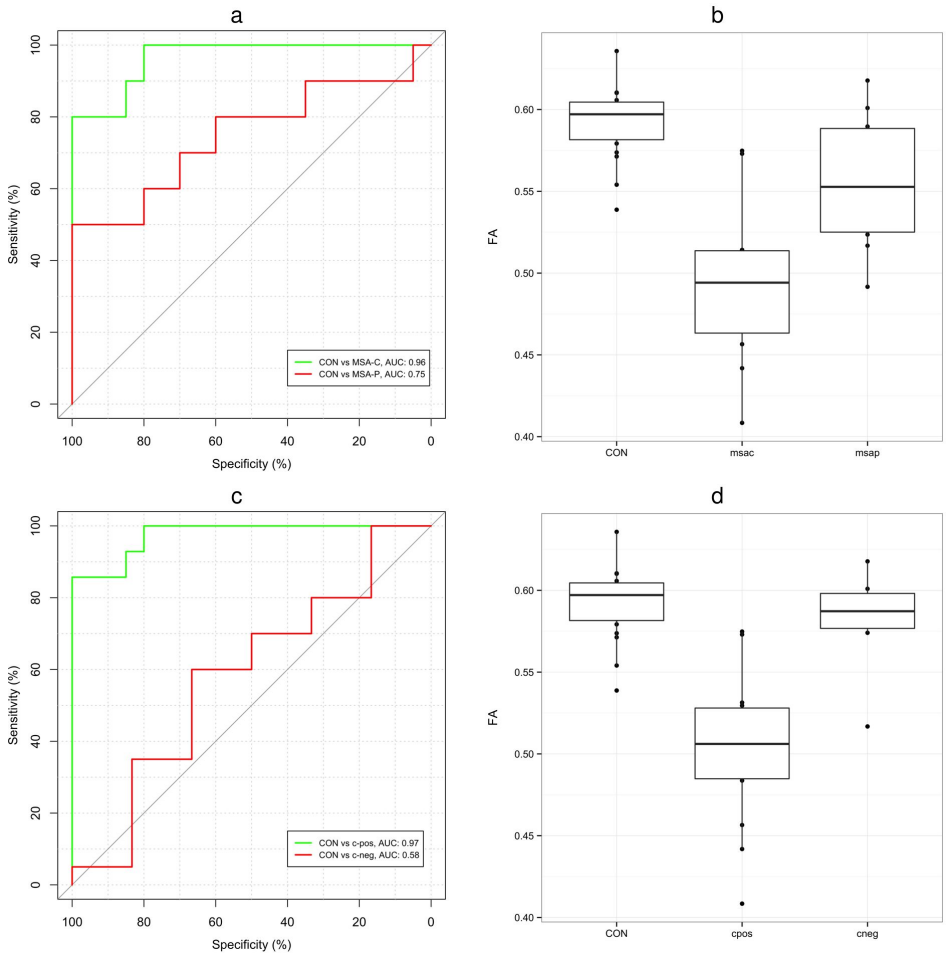


Figure 4.33: ROC results in the MCP between patients and controls in FA: a) ROC curves between traditional MSA subgroups and controls, b) boxplot representation of the same data, c) ROC curves between phenotypic MSA subgroups and controls, d) boxplot representation of the same data. MCP, middle cerebellar peduncle; FA, fractional anisotropy.

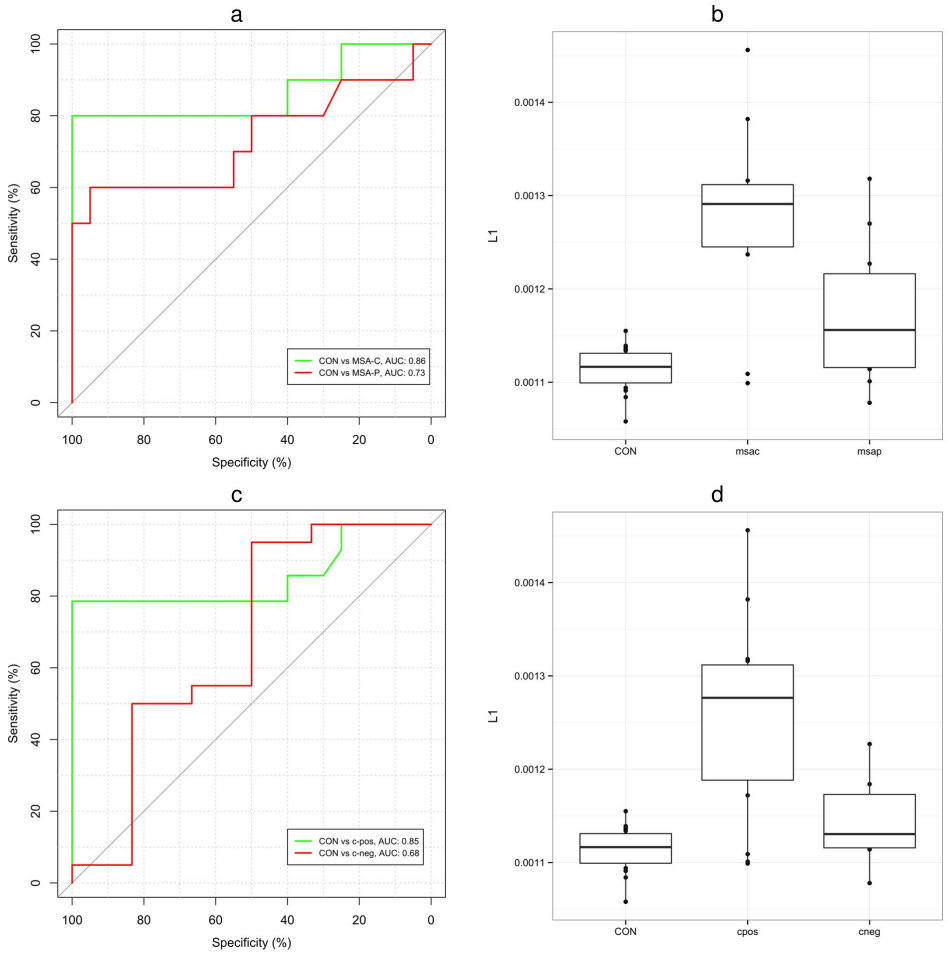


Figure 4.34: ROC results in the MCP between patients and controls in $\lambda 1$: a) ROC curves between traditional MSA subgroups and controls, b) boxplot representation of the same data, c) ROC curves between phenotypic MSA subgroups and controls, d) boxplot representation of the same data. MCP, middle cerebellar peduncle.

We additionally assessed qualitative radiological signs associated with MSA that are appreciable on traditional imaging sequences; signal changes in the lateral putamen, and the hot cross bun sign in the pons (see Table 4.5). Traditional classification and classification by phenotype (cPOS, pPOS) were performed. In general, we observed better performance when considering MSA by phenotypic expression, the only exception being a higher negative predictive value (NPV) of the hot cross bun test in the traditional classification.

Table 4.5: Qualitative radiological signs

	Traditional		Phenotypic	
	BUN	RIM	BUN	RIM
Sensitivity	.80	.73	.79	.94
Specificity	.50	.33	.67	.75
PPV	.62	.57	.85	.94
NPV	.71	.50	.57	.74

Table 4.5: Evaluation of qualitative radiological signs typically associated with multiple system atrophy. Phenotypic classifications were cerebellar-positive MSA (cPOS) in evaluation of the BUN sign, and parkinsonian-positive (pPOS) in assessment of the RIM sign. BUN, hot cross bun sign, RIM, signal changes in the lateral rim of the putamen, PPV, positive predictive value, NPV, negative predictive value.

In our endeavor to understand reality we are somewhat like a man trying to understand the mechanism of a closed watch. He sees the face and the moving hands, even hears its ticking, but he has no way of opening the case. If he is ingenious he may form some picture of a mechanism which could be responsible for all the things he observes, but he may never be quite sure his picture is the only one which could explain his observations.

Albert Einstein

5

Discussion

Application to gray matter

We have shown the applicability of DTI to both gray and white matter regions of the brain. While the correlates of DTI metrics in brain white matter are relatively well understood [117, 118, 119], DTI in the gray matter is more difficult to interpret. In the present work, we have demonstrated that metalloprotein-bound iron makes an important contribution to DTI metrics in low-signal, isotropic, iron-rich regions such as brain gray matter. We were prompted to investigate the effect of metalloprotein-bound iron on diffusion metrics by the initial observation that FA in gray matter regions measured *in vivo* appeared to roughly correlate with iron concentrations [65, 92] reported postmortem [44] (Figure 3.1). Ferritin-bound iron, R_2, and SNR were included as covariates as they represent a possible continuum of cause to effect, although these variables

are not strictly dependent on each other. As superparamagnetic iron decreases T_2 relaxation time (increases R_2) [126, 128], SNR decreases (1/SNR increases) on T_2-weighted SSSE-EPI data [21, 43, 75, 121].

Our *in vitro* data illustrate the isolated effect of ferritin-bound iron, mediated by iron-dependent signal attenuation. Eigenvalue repulsion with decreasing SNR has been previously reported [14, 95]. Although only changes in $\lambda 3$ were significant at 3T, there was a clear visual trend of eigenvalue repulsion that was reflected in FA changes. FA increased with increasing 1/SNR (decreasing SNR) and R_2, while MD was insensitive to these changes *in vitro*. These findings are supported by our *in vivo* data where similar correlations were observed. Linear dependencies between tensor-derived scalars and 1/SNR and R_2 were achieved in pooled data, with FA increasing and MD decreasing as 1/SNR and R_2 increased.

Differences between *in vivo* and *in vitro* results may be related to differences in the composition of agarose gel [4] in comparison to the underlying cytoarchitecture of the gray matter, as previous studies have demonstrated the dependence of eigenvalue repulsion on the inherent anisotropy of a medium [14, 95]. We arrived at the composition of our *in vitro* model after experimentally determining the concentration of agarose that approximates the anisotropy of gray matter free of artifactual contamination (see Figure 3.1, y-intercept). Although the agarose model is a close approximation to gray matter at the voxel scale, the behavior of individual eigenvalues is likely sensitive to subtle differences.

Other factors must be taken into consideration when attempting to interpret differences between the *in vivo* and *in vitro* results. The *in vivo* environment is more complex, with many factors that could contribute to DTI measurements such as the presence of myelinated fibers in gray matter structures and physiological noise. Furthermore, the clustering effect of ferritin *in vivo* increases magnetic inhomogeneity [41, 126]. R_2 is also not only dependent on iron content, but is affected by several factors such as temperature, tissue density, and water content [9, 14, 95]. PD was included to control for tissue density and water content, and that PD did not make a significant contribution to the results

supports the hypothesis that ferritin-bound iron played a key role the observed correlations. $\lambda 3$ showed the strongest correlation with R_2 both *in vitro* and *in vivo*, seemingly the least affected by confounding factors *in vivo*. $\lambda 3$ measurements within the individual nuclei followed R_2 values, while FA and MD values proved less specific. The pattern observed in FA values within the basal ganglia is in agreement with previously published data [49].

Several mechanisms have been proposed to DTI contrast in gray matter regions, such as the loss of myelinated fibers passing through gray matter structures [32, 102], neuronal and dendrite elimination with age [48] and the targeted loss of certain dendrite connections leading to increased anisotropy [47], as well as tissue compaction and gliosis associated with aging [134]. Our results show that ferritin-bound iron makes an important contribution to DTI metrics in low-signal, isotropic, iron-rich regions, which is an important consideration in studies examining the DTI characteristics of gray matter regions, especially in studies focused on adolescence as well as diseases associated with altered brain-iron load such as pantothenate kinase-associated neurodegeneration (PKAN), Huntington disease and MSA. Based on our *in vitro* findings, we would expect that a fifty percent increase in R_2 would result in a 75% increase in FA. This estimate is roughly in agreement with our *in vivo* observations and additional confounding factors *in vivo*, as discussed previously, would be expected to contributions as well.

It has been reported that the iron content of gray matter may be dependent on age [8, 11, 29, 44, 46, 47, 134]. Hallgren and Sourander reported increasing iron with age in several gray matter regions, plateauing at approximately age thirty [44]. That we only observed significant correlations with age in the putamen is not surprising for several reasons. Our volunteer group was composed of older adults in comparison to previous studies, and although iron does continue to accumulate throughout the lifespan, it occurs over a limited range beyond thirty years of age. Notably, the most gradual accumulation in the regions we examined occurs in the putamen. More subtle changes across the age range in our study would require a much larger sample to be appreciated.

Application to amyotrophic lateral sclerosis

We have shown T_2 relaxation rate differences in the head of caudate nucleus in ALS subjects in comparison to controls. Atrophy of the head of the left caudate was found in a subgroup of rapidly progressing ALS patients in another study [3]. Significant changes of T_2 relaxation rate in this region are of further importance as the caudate nucleus has been used as an internal reference in qualitative and quantitative studies of ALS patients [53, 54, 83]. It is interesting to note that the relaxation rate changes detected in this region were not dependent on disease duration. This suggests that decreased R_2 is already present in the earlier stages of the disease and could therefore serve as an early marker of disease activity. Future investigation should focus on quantifying changes in head of the caudate nuclei in a large group patients in the earliest stage of ALS.

Significant changes in the T_2 relaxation rate of the caudate nucleus are not surprising when considering that ALS is not limited to the motor system and that relaxometric changes in the basal ganglia have been observed in other neurodegenerative diseases [10]. T_2 contrast in the deep grey matter nuclei is predominantly determined by tissue iron in metalloproteins [127, 129]. A decrease in the metalloprotein-bound iron ("safe" iron) results in a relative decrease in R_2, and more iron in the low molecular forms ("toxic" iron) is available. We propose that the significant T_2 relaxation rate changes in the left caudate nucleus observed in our study are related to iron deposition in this region. The observed changes cannot be explained by a change in water content as the proton density did not differ between patients and controls.

We also detected significantly decreased R_2 in the bilateral FWM of ALS patients compared to controls. Therefore, we recommend that FWM (as well as head of caudate nuclei) should not be used as an internal reference for the assessment of increased signal intensity in various brain regions in ALS [53, 54]. The T_2 relaxation rate in the FWM was also found to correlate with age in both patients and controls. Bartzokis et al. demonstrated the age dependence of R_2 in the FWM at both 0.5T and 1.5T in healthy subjects [9]. A trend towards a steeper

decrease of T_2 relaxation rate with age in our group of ALS patients was observed, but the difference did not reach the statistical threshold. As age-related changes in the FWM were detected in both patients and controls, this may indicate that decreased R_2 in the FWM is age-dependent and that ALS does not influence this correlation significantly.

No statistically significant changes were detected in the PLIC, a region suspected of signal intensity changes in ALS. T2 hyperintensity in this area, labelled as CI3 in histological studies, was observed in nearly all subjects. A confocal microscopy study by Axer and Keyserlingk [5] revealed that fibers of the corticospinal tract (running superoinferior) cross fibers of the upper thalamic peduncle (running anteroposterior) in this region. In section, a pale area in the most posterior part of internal capsule was more difficult to discern and was less stained by silver than by myelin stain in ALS subjects. This area included thinner axons (> 0.8 μm), surrounded by "free space". The posterior aspect of the area was clearly delimited, and the anterior aspect disappeared gradually. In ALS patients, the loss of thin myelinated fibers in this area has been proven [56]. Even though these findings would suggest decreased R_2 in this area, our study quantitatively confirms earlier statements [23, 39] that the relatively hyperintense signal in this part of the internal capsule is a physiological variant and not disease related as was believed [57, 137].

Considering our work showing the dependance of DTI metrics on R_2 [104], investigation of DTI metrics in the basal ganglia would be of interest. However, due to the dual-slab nature of the diffusion data acquired by a work-in-progress package, we were unable to follow-up these relaxometry results with diffusion analyses. We did however investigate white matter changes in the upper slab by means of TBSS. TBSS revealed decreased FA in the corona radiata, and no changes were detected in the lower parts of the pyramidal tract. No changes in FA in the corticospinal tract were found using an ROI-based approach. This can be at least partially explained by the process of averaging the data on the skeleton in a voxel-wise manner, which, in contrast to an ROI-based approach, is not influenced by selection size or a priori knowledge. Moreover, an ROI positioned close to fine white fibers is more prone to noise.

No changes in the FWM were detected by means of TBSS or ROI-based methods. Decreased FA in the callosal body is in agreement with current knowledge of frontotemporal lobar degeneration. Therefore, future research should focus more on fine fibers. Changes in R_2 and not FA in this region can be explained by demyelinating changes in the white matter that precede changes in anisotropy. Thus, changes in T_2 relaxation rate may precede decreased diffusion anisotropy.

Application to multiple system atrophy

In the present study we investigated global white matter characteristics in MSA *in vivo*. Our TBSS results show widespread differences in the white matter of MSA subjects in comparison to controls, reflected primarily in increased RD and MD (see Figure 4.16). While MD is known to be a sensitive but non-specific marker of morphological changes in the white matter, RD has been shown to correlate with myelin integrity [117, 118]. Our findings therefore lend support to the hypothesis that MSA is a primary oligodendrogliopathy.

In examining DTI differences between the MSA-P and MSA-C subgroups and controls, we observed similar differences between MSA-C subjects and controls (Figure 4.18), and only supratentorial differences between MSA-P subjects and controls (Figure 4.17). MSA-C subjects would be expected to be more severely affected infratentorially than MSA-P subjects, and we did observe qualitatively on standard imaging sequences that infratentorial changes in MSA-C subjects were more striking than in their MSA-P counterparts. Similar to the results of all MSA subjects versus controls, the MSA-C (Figure 4.18) and MSA-P (Figure 4.17) subgroups showed the greatest differences in RD and MD. These observations are not in conflict with those reported previously [62, 89, 96, 113], however, due to methodological differences (TBSS versus other approaches) a direct comparison with previous studies is not possible.

Half of the patient participants in our study exhibited both cerebellar and parkinsonian manifestations, in agreement with previous studies [90, 108]. As

we did not observe any differences between the MSA-C and MSA-P diagnostic subgroups by TBSS, we hypothesized that the large degree of overlap was likely responsible. We therefore reclassified our patient group by phenotype, separating those subjects with only cerebellar (cMSA) or parkinsonian manifestations (pMSA) from those with a mixed presentation. TBSS was then performed on the restructured groups.

Differences between cMSA subjects and controls by TBSS were similar to those between MSA-C and controls. To our surprise, pMSA subjects did not differ significantly from controls in any region, by any DTI metric. This may indicate an alternate pathogenesis behind the parkinsonian component of MSA. In a large series of 100 definite MSA cases, Ozawa et al. [90] reported that pathological changes in striatonigral degeneration likely begin in the substantia nigra, where neuronal cell death appears to occur independent of GCI accumulation, and concluded that other factors contribute to this phenotype. The authors did not observe any cases of pure striatonigral or olivopontocerebellar pathology (corresponding to pMSA and cMSA in the present work), likely related to the postmortem nature of the study, i.e., at the terminus of the disease process it is likely that both striatonigral and olivopontocerebellar systems are effected. Our observations in pMSA and cMSA support the hypothesis that factors other than GCI accumulation may be responsible for striatonigral degeneration. The differences in DTI metrics detected by TBSS between patients and controls were driven by the cerebellar component of the disease, i.e., by patients with a positive cerebellar phenotype, supported by the finding that the pMSA subgroup did not differ from controls. The observation that pMSA is not detectable by DTI in the white matter is not surprising if the underlying pathology is isolated to the striatonigral system. However, that white matter changes related to the cerebellar phenotype are widespread, not only infratentorially but supratentorially as well, warrants further investigation.

In evaluating differences in DTI metrics in the basal ganglia between MSA subjects and controls, we explored differences between both the traditional MSA subgroups and controls, as well as between phenotypic MSA subgroups and controls. The reclassification by phenotype was performed in an attempt to

increase the utility of DTI in this setting, concordant with our hypothesis that parkinsonian-positive MSA subjects (pPOS) would likely show alterations in the basal ganglia, while parkinsonian-negative MSA subjects (pNEG) would likely not. The addition of $\lambda 3$ to the analysis was made to further clarify any diffusion changes noted, as iron accumulation in the putamen has been shown previously [130, 135], and we have shown that ferritin-bound iron results in eigenvalue repulsion [104]. We detected significant differences between the MSA-P group and others, and between the pMSA group and others, in RD, MD, $\lambda 1$ and $\lambda 3$ in the putamen only, with no differences observed in FA. Further ROC analyses were carried out to explore the classification potential of these metrics in the putamen. Similar results were seen between the MSA-P versus control and pPOS versus control tests. Performance was reduced however in the pNEG versus control tests in comparison to the MSA-C versus control tests. This reflects the transfer of parkinsonian-positive MSA-C subjects to the pPOS group when reclassified, and as their classification ability no longer contributed to the AUC, it decreased. Thus, the sensitivity and specificity improved with reclassification, as more subjects were correctly classified.

We applied similar ROC analyses to the MCP, to evaluate the diagnostic potential of this region in MSA subjects with positive cerebellar manifestations. The MCP was chosen in large part due to the robust results observed by TBSS and therefore ANOVA was not performed in this region. We again explored differences between both the traditional MSA subgroups and controls, as well as between phenotypic MSA subgroups and controls. The reclassification by phenotype was similarly performed in an attempt to increase the utility of DTI in this region, concordant with our hypothesis that cerebellar-positive MSA subjects (cPOS) would likely show alterations in the MCP, while cerebellar-negative MSA subjects (cNEG) would likely not. Similar to our results in the putamen, we observed better overall performance when the data were reclassified. The AUC in cNEG versus controls was lower than in MSA-P versus controls, again reflecting the reallocation of classification ability driven by phenotype. Therefore, classification by phenotype improved the sensitivity and specificity of the tests, allowing more patients to be correctly classified.

As a comparison and to provide complementary diagnostic information, we also evaluated the presence or absence of radiological signs associated with MSA that are appreciable on traditional imaging sequences; signal changes in the lateral putamen, and the hot cross bun sign in the pons. In general, we observed better performance when considering MSA by phenotypic expression, the only exception being a higher NPV ("rule out" performance) when considering the hot cross bun sign under the traditional classification. The reason for this paradoxically better result in the traditional classification is that one MSA-P subject with a positive cerebellar phenotype (MSA-P, cPOS) had more generalized cerebellar atrophy without an appreciable hot cross bun sign. Therefore, this subject was classified a true negative when considering the traditional classification, and as a false negative under the phenotypic classification. Thus, these two qualitative signs are not sufficient in the diagnostic process, however, we have shown that qualitative radiological signs may serve a complementary role to the more robust DTI evaluation in MSA patients, especially when considering the disease process from a phenotypical perspective.

Research is to see what everyone else has seen, and to think what nobody else has thought.

Albert Szent-Györgyi

6

Conclusions

We have shown the effect of ferritin-bound iron on DTI metrics *in vitro*, with correlation *in vivo*. Signal attenuation on SE-EPI data due to predominantly superparamagnetic ferritin-bound iron is reflected in increased R_2 and decreased SNR, resulting in systematic, artifactual changes in tensor-derived scalars. This effect has little consequence in brain white matter where the SNR is very high, but in low-signal regions such as the gray matter DTI metrics may be significantly affected. This observation has important implications for DTI studies targeting gray matter regions, especially in studies focused on adolescence as well as diseases associated with altered brain-iron load such as PKAN, Huntington disease and MSA.

In ALS, we found only non-specific changes in DTI metrics in the brain white matter. Additionally we found decreased R_2 in the left caudate and bilateral FWM, which may aid in the diagnostic process and disqualifies these regions as

internal controls in ALS studies. Furthermore, we demonstrated that the PLIC is not a reliable diagnostic marker of ALS. Considering these qualitative and quantitative measures, the evaluation of ALS subjects by MRI may be improved.

Finally in MSA, we detected widespread changes in the brain white matter, however only in MSA subjects with a positive clinical history of cerebellar manifestations. In MSA subjects with only parkinsonian features, no alterations in DTI metrics in the white matter were detected. This has important implications in the diagnosis of MSA. However, in MSA patients with a positive clinical history of Parkinsonism, we detected significantly altered tensor-derived scalars in the bilateral putamen. These changes included increased $\lambda 3$, and considering our *in vitro* results, indicates that DTI changes in the putamen are likely driven primarily by true changes in diffusion rather than changes in local iron status. In considering these observations together, we have shown that DTI in the MCP in cerebellar-positive MSA subjects and in the putamen in parkinsonian-positive MSA subjects may differentiate MSA from control subjects with very high accuracy, greatly improving existing methods. For this purpose, we propose the use of MD, which showed very high accuracy in all relevant tests, and is readily accessible in most commercial software packages furnished by manufacturers.

References

[1] The Amyotrophic Lateral Sclerosis Functional Rating Scale. Assessment of activities of daily living in patients with amyotrophic lateral sclerosis. The ALS CNTF treatment study (ACTS) phase I-II study group. *Arch Neurol*. 1996;53(2):141–147.

[2] Abe K, Hikita T, Yokoe M, Mihara M, and Sakoda S. The "cross" signs in patients with multiple system atrophy: a quantitative study. *J Neuroimaging*. 2006;16(1):73–77.

[3] Agosta F, Gorno-Tempini ML, Pagani E, Sala S, Caputo D, Perini M, Bartolomei I, Fruguglietti ME, and Filippi M. Longitudinal assessment of grey matter contraction in amyotrophic lateral sclerosis: A tensor based morphometry study. *Amyotroph Lateral Scler*. 2009;10(3):168–174.

[4] Arnott S, Fulmer A, Scott WE, Dea IC, Moorhouse R, and Rees DA. The agarose double helix and its function in agarose gel structure. *J Mol Biol*. 1974;90(2):269–284.

[5] Axer H and Keyserlingk DG. Mapping of fiber orientation in human internal capsule by means of polarized light and confocal scanning laser microscopy. *J Neurosci Methods*. 2000;94(2):165–175.

[6] Barnea-Goraly N, Menon V, Eckert M, Tamm L, Bammer R, Karchemskiy A, Dant CC, and Reiss AL. White matter development during childhood and adolescence: A cross-sectional diffusion tensor imaging study. *Cereb Cortex*. 2005;15(12):1848 –1854.

[7] Bartzokis G, Aravagiri M, Oldendorf WH, Mintz J, and Marder SR. Field dependent transverse relaxation rate increase may be a specific measure of tissue iron stores. *Magn Reson Med*. 1993;29(4):459–464.

[8] Bartzokis G, Beckson M, Hance DB, Marx P, Foster JA, and Marder SR. MR evaluation of age-related increase of brain iron in young adult and older normal males. *Magn Reson Imaging*. 1997;15(1):29–35.

[9] Bartzokis G, Mintz J, Sultzer D, Marx P, Herzberg JS, Phelan CK, and Marder SR. In vivo MR evaluation of age-related increases in brain iron. *AJNR Am J Neuroradiol*. 1994;15(6):1129–1138.

[10] Bartzokis G and Tishler TA. MRI evaluation of basal ganglia ferritin iron and neurotoxicity in Alzheimer's and Huntingon's disease. *Cell Mol Biol (Noisy-le-grand)*. 2000;46(4):821–833.

[11] Bartzokis G, Tishler TA, Lu PH, Villablanca P, Altshuler LL, Carter M, Huang D, Edwards N, and Mintz J. Brain ferritin iron may influence age- and gender-related risks of neurodegeneration. *Neurobiol Aging*. 2007; 28(3):414–423.

[12] Basser PJ, Mattiello J, and LeBihan D. Estimation of the effective self-diffusion tensor from the NMR spin echo. *J Magn Reson B*. 1994; 103(3):247–254.

[13] Basser PJ, Mattiello J, and LeBihan D. MR diffusion tensor spectroscopy and imaging. *Biophys J*. 1994;66(1):259–267.

[14] Bastin ME, Armitage PA, and Marshall I. A theoretical study of the effect of experimental noise on the measurement of anisotropy in diffusion imaging. *Magn Reson Imaging*. 1998;16(7):773–785.

[15] Bloch F. Nuclear induction. *Phys Rev*. 1946;70(7-8):460–474.

[16] Bratton CB, Hopkins AL, and Weinberg JW. Nuclear magnetic resonance studies of living muscle. *Science*. 1965;147(3659):738–739.

[17] Brooks BR. El escorial world federation of neurology criteria for the diagnosis of amyotrophic lateral sclerosis. *J Neurol Sci*. 1994;124 Suppl:96–107.

[18] Brooks RA, Vymazal J, Goldfarb RB, Bulte JW, and Aisen P. Relaxometry and magnetometry of ferritin. *Magn Reson Med*. 1998;40(2):227–235.

[19] Brown R. A brief account of microscopical observations made in the months of june, july and august, 1827, on the particles contained in the pollen of plants; and on the general existence of active molecules in organic and inorganic bodies. *Phil Mag*. 1828;4:161–173.

[20] Bürk K, Skalej M, and Dichgans J. Pontine MRI hyperintensities ("the cross sign") are not pathognomonic for multiple system atrophy (MSA). *Mov Disord*. 2001;16(3):535.

[21] Carr HY and Purcell EM. Effects of diffusion on free precession in nuclear magnetic resonance experiments. *Phys Rev*. 1954;94(3):630–638.

[22] Chenevert TL, Brunberg JA, and Pipe JG. Anisotropic diffusion in human white matter: demonstration with MR techniques in vivo. *Radiology*. 1990;177(2):401–405.

[23] Cheung G, Gawel MJ, Cooper PW, Farb RI, Ang LC, and Gawal MJ. Amyotrophic lateral sclerosis: correlation of clinical and MR imaging findings. *Radiology*. 1995;194(1):263–270.

[24] Connor JR and Menzies SL. Cellular management of iron in the brain. *J Neurol Sci*. 1995;134(Supplement 1):33–44.

[25] Connor JR, Menzies SL, Burdo JR, and Boyer PJ. Iron and iron management proteins in neurobiology. *Pediatr Neurol*. 2001; 25(2):118–129.

[26] Cooke R and Wien R. The state of water in muscle tissue as determined by proton nuclear magnetic resonance. *Biophys J*. 1971;11(12):1002–1017.

[27] Cortese S, Azoulay R, Castellanos FX, Chalard F, Lecendreux M, Chechin D, Delorme R, Sebag G, Sbarbati A, Mouren MC, Bernardina BD, and Konofal E. Brain iron levels in attention-deficit/hyperactivity disorder: A pilot MRI study. *World J Biol Psychiatry*. 2011;13(3):223–231.

[28] Cosottini M, Giannelli M, Siciliano G, Lazzarotti G, Michelassi MC, Del Corona A, Bartolozzi C, and Murri L. Diffusion-tensor MR imaging of corticospinal tract in amyotrophic lateral sclerosis and progressive muscular atrophy. *Radiology*. 2005;237(1):258–264.

[29] Càmara E, Bodammer N, Rodríguez-Fornells A, and Tempelmann C. Age-related water diffusion changes in human brain: a voxel-based approach. *Neuroimage*. 2007;34(4):1588–1599.

[30] Damadian R. Tumor detection by nuclear magnetic resonance. *Science*. 1971;171(3976):1151–1153.

[31] Damadian R, Goldsmith M, and Minkoff L. NMR in cancer: XVI. FONAR image of the live human body. *Physiol Chem Phys*. 1977; 9(1):97–100, 108.

[32] Douaud G, Behrens TE, Poupon C, Cointepas Y, Jbabdi S, Gaura V, Golestani N, Krystkowiak P, Verny C, Damier P, Bachoud-Lévi AC, Hantraye P, and Remy P. In vivo evidence for the selective subcortical degeneration in Huntington's disease. *Neuroimage*. 2009;46(4):958–966.

[33] Earley CJ, B Barker P, Horská A, and Allen RP. MRI-determined regional brain iron concentrations in early- and late-onset restless legs syndrome. *Sleep Med*. 2006;7(5):458–461.

[34] Edelstein WA, Bottomley PA, and Pfeifer LM. A signal-to-noise calibration procedure for NMR imaging systems. *Med Phys*. 1984; 11(2):180–185.

[35] Einstein A. Über die von der molekularkinetischen theorie der wärme geforderte bewegung von in ruhenden flüssigkeiten suspendierten teilchen. *Ann Phys*. 1905;322(8):549–560.

[36] Fick A. Ueber diffusion. *Ann Phys*. 1855;170(1):59–86.

[37] Gerlach W and Stern O. Über die richtungsquantelung im magnetfeld. *Ann Phys*. 1924;379(16):673–699.

[38] Gilman S, Wenning GK, Low PA, Brooks DJ, Mathias CJ, Trojanowski JQ, Wood NW, Colosimo C, Dürr A, Fowler CJ, Kaufmann H, Klockgether T, Lees A, Poewe W, Quinn N, Revesz T, Robertson D, Sandroni P, Seppi K, and Vidailhet M. Second consensus statement on the diagnosis of multiple system atrophy. *Neurology*. 2008;71(9):670–676.

[39] Goodin DS, Rowley HA, and Olney RK. Magnetic resonance imaging in amyotrophic lateral sclerosis. *Ann Neurol*. 1988;23(4):418–420.

[40] Gorter C and Broer L. Negative result of an attempt to observe nuclear magnetic resonance in solids. *Physica*. 1942;9(6):591–596.

[41] Gossuin Y, Gillis P, Muller RN, and Hocq A. Relaxation by clustered ferritin: a model for ferritin-induced relaxation in vivo. *NMR Biomed*. 2007;20(8):749–756.

[42] Haacke EM, Cheng NYC, House MJ, Liu Q, Neelavalli J, Ogg RJ, Khan A, Ayaz M, Kirsch W, and Obenaus A. Imaging iron stores in the brain using magnetic resonance imaging. *Magn Reson Imaging*. 2005;23(1):1–25.

[43] Hahn EL. Spin echoes. *Phys Rev*. 1950;80(4):580–594.

[44] Hallgren B and Sourander P. The effect of age on the non-haemin iron in the human brain. *J Neurochem*. 1958;3(1):41–51.

[45] Hansen JR. Pulsed NMR study of water mobility in muscle and brain tissue. *Biochim Biophys Acta*. 1971;230(3):482–486.

[46] Hasan KM and Frye RE. Diffusion tensor-based regional gray matter tissue segmentation using the international consortium for brain mapping atlases. *Hum Brain Mapp*. 2011;32(1):107–117.

[47] Hasan KM, Halphen C, Boska MD, and Narayana PA. Diffusion tensor metrics, T2 relaxation, and volumetry of the naturally aging human caudate nuclei in healthy young and middle-aged adults: possible implications for the neurobiology of human brain aging and disease. *Magn Reson Med*. 2008;59(1):7–13.

[48] Hasan KM, Halphen C, Kamali A, Nelson FM, Wolinsky JS, and Narayana PA. Caudate nuclei volume, diffusion tensor metrics, and T2 relaxation in healthy adults and relapsing-remitting multiple sclerosis patients: Implications to understanding gray matter degeneration. *J Magn Reson Imaging*. 2009;29(1):70–77.

[49] Hasan KM, Walimuni IS, Abid H, Kramer LA, Frye RE, Fletcher JM, and Ewing-Cobbs L. DTI, T2 relaxation and volumetry of the human brain corpus striatum across the lifespan. In: *Proceedings of the International Society for Magnetic Resonance in Medicine*. 2010; Abstract 606.

[50] Hazlewood CF, Nichols BL, and Chamberlain NF. Evidence for the existence of a minimum of two phases of ordered water in skeletal muscle. *Nature*. 1969;222(5195):747–750.

[51] Hazlewood CF, Nichols BL, Chang DC, and Brown B. On the state of water in developing muscle: a study of the major phase of ordered water in skeletal muscle and its relationship to sodium concentration. *Johns Hopkins Med J*. 1971;128(3):117–131.

[52] Head D, Buckner RL, Shimony JS, Williams LE, Akbudak E, Conturo TE, McAvoy M, Morris JC, and Snyder AZ. Differential vulnerability of anterior white matter in nondemented aging with minimal acceleration in dementia of the Alzheimer type: Evidence from diffusion tensor imaging. *Cereb Cortex*. 2004;14(4):410 –423.

[53] Hecht MJ, Fellner F, Fellner C, Hilz MJ, Heuss D, and Neundörfer B. MRI-FLAIR images of the head show corticospinal tract alterations in

ALS patients more frequently than T2-, T1- and proton-density-weighted images. *J Neurol Sci*. 2001;186(1-2):37–44.

[54] Hecht MJ, Fellner F, Fellner C, Hilz MJ, Neundörfer B, and Heuss D. Hyperintense and hypointense MRI signals of the precentral gyrus and corticospinal tract in ALS: a follow-up examination including FLAIR images. *J Neurol Sci*. 2002;199(1-2):59–65.

[55] Hinshaw WS, Bottomley PA, and Holland GN. Radiographic thin-section image of the human wrist by nuclear magnetic resonance. *Nature*. 1977; 270(5639):722–723.

[56] Hirayama K, Tsubaki T, Toyokura Y, and Okinaka S. The representation of the pyramidal tract in the internal capsule and basis pedunculi. a study based on three cases of amyotrophic lateral sclerosis. *Neurology*. 1962; 12:337–342.

[57] Hofmann E, Ochs G, Pelzl A, and Warmuth-Metz M. The corticospinal tract in amyotrophic lateral sclerosis: an MRI study. *Neuroradiology*. 1998; 40(2):71–75.

[58] Holland D, Kuperman JM, and Dale AM. Efficient correction of inhomogeneous static magnetic field-induced distortion in echo planar imaging. *Neuroimage*. 2010;50(1):175–183.

[59] Hollis DP, Economou JS, Parks LC, Eggleston JC, Saryan LA, and Czeister JL. Nuclear magnetic resonance studies of several experimental and human malignant tumors. *Cancer Res*. 1973;33(9):2156–2160.

[60] Horimoto Y, Aiba I, Yasuda T, Ohkawa Y, Katayama T, Yokokawa Y, Goto A, and Ito Y. Longitudinal MRI study of multiple system atrophy - when do the findings appear, and what is the course? *J Neurol*. 2002; 249(7):847–854.

[61] Ishizawa K, Komori T, Arai N, Mizutani T, and Hirose T. Glial cytoplasmic inclusions and tissue injury in multiple system atrophy: A quantitative study in white matter (olivopontocerebellar system) and gray matter (nigrostriatal system). *Neuropathology*. 2008;28(3):249–257.

[62] Ito M, Watanabe H, Atsuta N, Senda J, Kawai Y, Tanaka F, Naganawa S, Fukatsu H, and Sobue G. Fractional anisotropy values detect pyramidal tract involvement in multiple system atrophy. *J Neurol Sci*. 2008; 271(1-2):40–46.

[63] Jackson JA and Langham WH. Whole-body NMR spectrometer. *Rev Sci Instrum*. 1968;39(4):510–513.

[64] Jezzard P and Balaban RS. Correction for geometric distortion in echo planar images from B0 field variations. *Magn Reson Med*. 1995; 34(1):65–73.

[65] Keller J, Rulseh AM, Syka M, and Vymazal J. Fractional anisotropy in various white and gray matter regions in adulthood: dependence on age and comparison of two DTI sequences. In: *Proceedings of the International Society for Magnetic Resonance in Medicine*. 2010; Abstract 1560.

[66] Kitamura K, Nakayama K, Kosaka S, Yamada E, Shimada H, Miki T, and Inoue Y. Diffusion tensor imaging of the cortico-ponto-cerebellar pathway in patients with adult-onset ataxic neurodegenerative disease. *Neuroradiology*. 2008;50(4):285.

[67] Kraft E, Schwarz J, Trenkwalder C, Vogl T, Pfluger T, and Oertel WH. The combination of hypointense and hyperintense signal changes on T2-weighted magnetic resonance imaging sequences: a specific marker of multiple system atrophy? *Arch Neurol*. 1999;56(2):225–228.

[68] Lauterbur PC. Image formation by induced local interactions: examples employing nuclear magnetic resonance. *Nature*. 1973; 242(5394):190–191.

[69] Le Bihan D, Breton E, Lallemand D, Grenier P, Cabanis E, and Laval-Jeantet M. MR imaging of intravoxel incoherent motions: application to diffusion and perfusion in neurologic disorders. *Radiology*. 1986;161(2):401–407.

[70] Lebel C, Walker L, Leemans A, Phillips L, and Beaulieu C. Microstructural maturation of the human brain from childhood to adulthood. *Neuroimage*. 2008;40(3):1044–1055.

[71] Lee EA, Cho HI, Kim SS, and Lee WY. Comparison of magnetic resonance imaging in subtypes of multiple system atrophy. *Parkinsonism Relat Disord*. 2004;10(6):363–368.

[72] Lee YC, Liu CS, Wu HM, Wang PS, Chang MH, and Soong BW. The 'hot cross bun' sign in the patients with spinocerebellar ataxia. *Eur J Neurol*. 2009;16(4):513–516.

[73] Lomen-Hoerth C, Murphy J, Langmore S, Kramer JH, Olney RK, and Miller B. Are amyotrophic lateral sclerosis patients cognitively normal? *Neurology*. 2003;60(7):1094–1097.

[74] Magelhaes PJ, Ram SJ, and Abramoff MD. Image processing with ImageJ. *Biophotonics International*. 2004;11(7):36–42.

[75] Mansfield P. Multi-planar image formation using NMR spin echoes. *J Phys C: Solid State Phys*. 1977;10(3):L55.

[76] Mansfield P and Grannell PK. NMR 'diffraction' in solids? *J Phys C: Solid State Phys*. 1973;6(22):L422.

[77] Mansfield P and Pykett I. Biological and medical imaging by NMR. *Journal of Magnetic Resonance (1969)*. 1978;29(2):355–373.

[78] Massey LA, Micallef C, Paviour DC, O'Sullivan SS, Ling H, Williams DR, Kallis C, Holton JL, Revesz T, Burn DJ, Yousry T, Lees AJ, Fox NC, and Jäger HR. Conventional magnetic resonance imaging in confirmed progressive supranuclear palsy and multiple system atrophy. *Mov Disord*. 2012;27(14):1754–1762.

[79] Meiboom S and Gill D. Modified Spin-Echo method for measuring nuclear relaxation times. *Rev Sci Instrum*. 1958;29(8):688–691.

[80] Moseley ME, Cohen Y, Kucharczyk J, Mintorovitch J, Asgari HS, Wendland MF, Tsuruda J, and Norman D. Diffusion-weighted MR imaging of anisotropic water diffusion in cat central nervous system. *Radiology*. 1990;176(2):439–445.

[81] Moseley ME, Cohen Y, Mintorovitch J, Chileuitt L, Shimizu H, Kucharczyk J, Wendland MF, and Weinstein PR. Early detection of regional cerebral ischemia in cats: comparison of diffusion- and T2-weighted MRI and spectroscopy. *Magn Reson Med*. 1990; 14(2):330–346.

[82] Murphy J, Henry R, and Lomen-Hoerth C. Establishing subtypes of the continuum of frontal lobe impairment in amyotrophic lateral sclerosis. *Arch Neurol*. 2007;64(3):330–334.

[83] Ngai S, Tang YM, Du L, and Stuckey S. Hyperintensity of the precentral gyral subcortical white matter and hypointensity of the precentral gyrus on fluid-attenuated inversion recovery: variation with age and implications for the diagnosis of amyotrophic lateral sclerosis. *AJNR Am J Neuroradiol*. 2007;28(2):250–254.

[84] Nicoletti G, Fera F, Condino F, Auteri W, Gallo O, Pugliese P, Arabia G, Morgante L, Barone P, Zappia M, and Quattrone A. MR imaging of middle cerebellar peduncle width: Differentiation of multiple system atrophy from parkinson disease. *Radiology*. 2006;239(3):825–830.

[85] Nilsson C, Bloch KM, Brockstedt S, Lätt J, Widner H, and Larsson E. Tracking the neurodegeneration of parkinsonian disorders–a pilot study. *Neuroradiology*. 2007;49(2):111–119.

[86] Oba H, Araki T, Ohtomo K, Monzawa S, Uchiyama G, Koizumi K, Nogata Y, Kachi K, Shiozawa Z, and Kobayashi M. Amyotrophic lateral sclerosis: T2 shortening in motor cortex at MR imaging. *Radiology*. 1993; 189(3):843–846.

[87] Odeblad E and Lindstrom G. Some preliminary observations on the proton magnetic resonance in biologic samples. *Acta radiol*. 1955; 43(6):469–476.

[88] Oishi K, Faria A, Jiang H, Li X, Akhter K, Zhang J, Hsu JT, Miller MI, van Zijl PCM, Albert M, Lyketsos CG, Woods R, Toga AW, Pike GB, Rosa-Neto P, Evans A, Mazziotta J, and Mori S. Atlas-based whole brain white matter analysis using large deformation diffeomorphic metric mapping: application to normal elderly and Alzheimer's disease participants. *Neuroimage*. 2009;46(2):486–499.

[89] Oishi K, Konishi J, Mori S, Ishihara H, Kawamitsu H, Fujii M, and Kanda F. Reduced fractional anisotropy in early-stage cerebellar variant of multiple system atrophy. *J Neuroimaging*. 2009;19(2):127–131.

[90] Ozawa T, Paviour D, Quinn NP, Josephs KA, Sangha H, Kilford L, Healy DG, Wood NW, Lees AJ, Holton JL, and Revesz T. The spectrum of pathological involvement of the striatonigral and olivopontocerebellar systems in multiple system atrophy: clinicopathological correlations. *Brain*. 2004;127(Pt 12):2657–2671.

[91] Papp MI, Kahn JE, and Lantos PL. Glial cytoplasmic inclusions in the CNS of patients with multiple system atrophy (striatonigral degeneration, olivopontocerebellar atrophy and Shy-Drager syndrome). *J Neurol Sci*. 1989;94(1-3):79–100.

[92] Pfefferbaum A, Adalsteinsson E, Rohlfing T, and Sullivan EV. Diffusion tensor imaging of deep gray matter brain structures: Effects of age and iron concentration. *Neurobiol Aging*. 2010;31(3):482–493.

[93] Phukan J, Pender NP, and Hardiman O. Cognitive impairment in amyotrophic lateral sclerosis. *Lancet Neurol*. 2007;6(11):994–1003.

[94] Pierpaoli C, Barnett A, Pajevic S, Chen R, Penix LR, Virta A, and Basser P. Water diffusion changes in wallerian degeneration and their dependence on white matter architecture. *Neuroimage*. 2001;13(6 Pt 1):1174–1185.

[95] Pierpaoli C and Basser PJ. Toward a quantitative assessment of diffusion anisotropy. *Magn Reson Med*. 1996;36(6):893–906.

[96] Prakash N, Hageman N, Hua X, Toga AW, Perlman SL, and Salamon N. Patterns of fractional anisotropy changes in white matter of cerebellar peduncles distinguish spinocerebellar ataxia-1 from multiple system atrophy and other ataxia syndromes. *Neuroimage*. 2009;47 Suppl 2:T72–81.

[97] Purcell EM, Torrey HC, and Pound RV. Resonance absorption by nuclear magnetic moments in a solid. *Phys Rev*. 1946;69(1-2):37–38.

[98] Rabi II, Zacharias JR, Millman S, and Kusch P. A new method of measuring nuclear magnetic moment. *Phys Rev*. 1938;53(4):318–318.

[99] Reber PJ, Wong EC, Buxton RB, and Frank LR. Correction of off resonance-related distortion in echo-planar imaging using EPI-based field maps. *Magn Reson Med*. 1998;39(2):328–330.

[100] Rippon GA, Scarmeas N, Gordon PH, Murphy PL, Albert SM, Mitsumoto H, Marder K, Rowland LP, and Stern Y. An observational study of cognitive impairment in amyotrophic lateral sclerosis. *Arch Neurol*. 2006;63(3):345–352.

[101] Robin X, Turck N, Hainard A, Tiberti N, Lisacek F, Sanchez JC, and Müller M. pROC: an open-source package for R and S+ to analyze and compare ROC curves. *BMC Bioinformatics*. 2011;12(1):77.

[102] Rosas HD, Tuch DS, Hevelone ND, Zaleta AK, Vangel M, Hersch SM, and Salat DH. Diffusion tensor imaging in presymptomatic and early Huntington's disease: Selective white matter pathology and its relationship to clinical measures. *Mov Disord*. 2006;21(9):1317–1325.

[103] Rose SE, Chen F, Chalk JB, Zelaya FO, Strugnell WE, Benson M, Semple J, and Doddrell DM. Loss of connectivity in Alzheimer's disease: an evaluation of white matter tract integrity with colour coded MR diffusion tensor imaging. *J Neurol Neurosurg Psychiatr*. 2000;69(4):528–530.

[104] Rulseh AM, Keller J, Tintěra J, Kožíšek M, and Vymazal J. Chasing shadows: What determines DTI metrics in gray matter regions? An in vitro and in vivo study. *J Magn Reson Imaging*. 2013; Doi: 10.1002/jmri.24065.

[105] Rusina R, Ridzon P, Kulist'ák P, Keller O, Bartos A, Buncová M, Fialová L, Koukolík F, and Matej R. Relationship between ALS and the degree of cognitive impairment, markers of neurodegeneration and predictors for poor outcome. a prospective study. *Eur J Neurol*. 2010;17(1):23–30.

[106] Sage CA, Van Hecke W, Peeters R, Sijbers J, Robberecht W, Parizel P, Marchal G, Leemans A, and Sunaert S. Quantitative diffusion tensor imaging in amyotrophic lateral sclerosis: revisited. *Hum Brain Mapp*. 2009;30(11):3657–3675.

[107] Sankoh AJ, Huque MF, and Dubey SD. Some comments on frequently used multiple endpoint adjustment methods in clinical trials. *Stat Med*. 1997;16(22):2529–2542.

[108] Schrag A, Good CD, Miszkiel K, Morris HR, Mathias CJ, Lees AJ, and Quinn NP. Differentiation of atypical parkinsonian syndromes with routine MRI. *Neurology*. 2000;54(3):697–702.

[109] Schrag A, Kingsley D, Phatouros C, Mathias CJ, Lees AJ, Daniel SE, and Quinn NP. Clinical usefulness of magnetic resonance imaging in multiple system atrophy. *J Neurol Neurosurg Psychiatry*. 1998;65(1):65–71.

[110] Schwarz J, Weis S, Kraft E, Tatsch K, Bandmann O, Mehraein P, Vogl T, and Oertel WH. Signal changes on MRI and increases in reactive microgliosis, astrogliosis, and iron in the putamen of two patients with multiple system atrophy. *J Neurol Neurosurg Psychiatry*. 1996; 60(1):98–101.

[111] Seppi K, Schocke MF, Mair KJ, Esterhammer R, Scherfler C, Geser F, Kremser C, Boesch S, Jaschke W, Poewe W, and Wenning GK. Progression of putaminal degeneration in multiple system atrophy: A serial diffusion MR study. *Neuroimage*. 2006;31(1):240–245.

[112] Shampo MA, Kyle RA, and Steensma DP. Isidor Rabi–1944 Nobel laureate in physics. *Mayo Clin Proc*. 2012;87(2):e11.

[113] Shiga K, Yamada K, Yoshikawa K, Mizuno T, Nishimura T, and Nakagawa M. Local tissue anisotropy decreases in cerebellopetal fibers and

pyramidal tract in multiple system atrophy. *J Neurol*. 2005; 252(5):589–596.

[114] Smith SM. Fast robust automated brain extraction. *Human Brain Mapping*. 2002;17(3):143–155.

[115] Smith SM, Jenkinson M, Johansen-Berg H, Rueckert D, Nichols TE, Mackay CE, Watkins KE, Ciccarelli O, Cader MZ, Matthews PM, and Behrens TEJ. Tract-based spatial statistics: voxelwise analysis of multi-subject diffusion data. *Neuroimage*. 2006;31(4):1487–1505.

[116] Smith SM, Jenkinson M, Woolrich MW, Beckmann CF, Behrens TEJ, Johansen-Berg H, Bannister PR, Luca MD, Drobnjak I, Flitney DE, Niazy RK, Saunders J, Vickers J, Zhang Y, Stefano ND, Brady JM, and Matthews PM. Advances in functional and structural MR image analysis and implementation as FSL. *Neuroimage*. 2004;23 Suppl 1:S208–219.

[117] Song S, Sun S, Ju W, Lin S, Cross AH, and Neufeld AH. Diffusion tensor imaging detects and differentiates axon and myelin degeneration in mouse optic nerve after retinal ischemia. *Neuroimage*. 2003;20(3):1714–1722.

[118] Song S, Sun S, Ramsbottom MJ, Chang C, Russell J, and Cross AH. Dysmyelination revealed through MRI as increased radial (but unchanged axial) diffusion of water. *Neuroimage*. 2002;17(3):1429–1436.

[119] Song S, Yoshino J, Le TQ, Lin S, Sun S, Cross AH, and Armstrong RC. Demyelination increases radial diffusivity in corpus callosum of mouse brain. *Neuroimage*. 2005;26(1):132–140.

[120] Song YJC, Lundvig DMS, Huang Y, Gai WP, Blumbergs PC, Højrup P, Otzen D, Halliday GM, and Jensen PH. p25alpha relocalizes in oligodendroglia from myelin to cytoplasmic inclusions in multiple system atrophy. *Am J Pathol*. 2007;171(4):1291–1303.

[121] Stejskal EO and Tanner JE. Spin diffusion measurements: Spin echoes in the presence of a time-dependent field gradient. *J Chem Phys*. 1965; 42(1):288–292.

[122] Sun SW, Liang HF, Cross AH, and Song SK. Evolving Wallerian degeneration after transient retinal ischemia in mice characterized by diffusion tensor imaging. *Neuroimage*. 2008;40(1):1–10.

[123] Sutton R, Kanal E, Wilkoff BL, Bello D, Luechinger R, Jenniskens I, Hull M, and Sommer T. Safety of magnetic resonance imaging of patients with

a new medtronic EnRhythm MRI SureScan pacing system: clinical study design. *Trials*. 2008;9:68.

[124] Taoka T, Kin T, Nakagawa H, Hirano M, Sakamoto M, Wada T, Takayama K, Wuttikul C, Iwasaki S, Ueno S, and Kichikawa K. Diffusivity and diffusion anisotropy of cerebellar peduncles in cases of spinocerebellar degenerative disease. *Neuroimage*. 2007;37(2):387–393.

[125] Tir M, Delmaire C, le Thuc V, Duhamel A, Destée A, Pruvo J, and Defebvre L. Motor-related circuit dysfunction in MSA-P: usefulness of combined whole-brain imaging analysis. *Mov Disord*. 2009; 24(6):863–870.

[126] Vymazal J, Brooks RA, Baumgarner C, Tran V, Katz D, Bulte JW, Bauminger R, and Di Chiro G. The relation between brain iron and NMR relaxation times: an in vitro study. *Magn Reson Med*. 1996;35(1):56–61.

[127] Vymazal J, Brooks RA, Patronas N, Hajek M, Bulte JW, and Di Chiro G. Magnetic resonance imaging of brain iron in health and disease. *J Neurol Sci*. 1995;134 Suppl:19–26.

[128] Vymazal J, Brooks RA, Zak O, McRill C, Shen C, and Di Chiro G. T1 and T2 of ferritin at different field strengths: effect on MRI. *Magn Reson Med*. 1992;27(2):368–374.

[129] Vymazal J, Hajek M, Patronas N, Giedd JN, Bulte JW, Baumgarner C, Tran V, and Brooks RA. The quantitative relation between T1-weighted and T2-weighted MRI of normal gray matter and iron concentration. *J Magn Reson Imaging*. 1995;5(5):554–560.

[130] Vymazal J, Righini A, Brooks RA, Canesi M, Mariani C, Leonardi M, and Pezzoli G. T1 and T2 in the brain of healthy subjects, patients with Parkinson disease, and patients with multiple system atrophy: relation to iron content. *Radiology*. 1999;211(2):489–495.

[131] Vymazal J, Urgosík D, and Bulte JW. Differentiation between hemosiderin- and ferritin-bound brain iron using nuclear magnetic resonance and magnetic resonance imaging. *Cell Mol Biol (Noisy-le-grand)*. 2000;46(4):835–842.

[132] Wang J, Wai Y, Lin WY, Ng S, Wang CH, Hsieh R, Hsieh C, Chen RS, and Lu CS. Microstructural changes in patients with progressive supranuclear palsy: a diffusion tensor imaging study. *J Magn Reson Imaging*. 2010; 32(1):69–75.

[133] Wang P, Wu H, Lin C, and Soong B. Use of diffusion tensor imaging to identify similarities and differences between cerebellar and parkinsonism forms of multiple system atrophy. *Neuroradiology*. 2010;53(7):471–481.

[134] Wang Q, Xu X, and Zhang M. Normal aging in the basal ganglia evaluated by eigenvalues of diffusion tensor imaging. *AJNR Am J Neuroradiol*. 2010; 31(3):516–520.

[135] Wang Y, Butros SR, Shuai X, Dai Y, Chen C, Liu M, Haacke EM, Hu J, and Xu H. Different iron-deposition patterns of multiple system atrophy with predominant parkinsonism and idiopathetic Parkinson diseases demonstrated by phase-corrected susceptibility-weighted imaging. *AJNR Am J Neuroradiol*. 2012;33(2):266–273.

[136] Wenning GK, Stefanova N, Jellinger KA, Poewe W, and Schlossmacher MG. Multiple system atrophy: a primary oligodendrogliopathy. *Annals of Neurology*. 2008;64(3):239–246.

[137] Yagishita A, Nakano I, Oda M, and Hirano A. Location of the corticospinal tract in the internal capsule at MR imaging. *Radiology*. 1994; 191(2):455–460.

[138] Zecca L, Youdim MBH, Riederer P, Connor JR, and Crichton RR. Iron, brain ageing and neurodegenerative disorders. *Nat Rev Neurosci*. 2004; 5(11):863–873.

[139] Zhan W, Kang GA, Glass GA, Zhang Y, Shirley C, Millin R, Possin KL, Nezamzadeh M, Weiner MW, Marks William J J, and Schuff N. Regional alterations of brain microstructure in Parkinson's disease using diffusion tensor imaging. *Mov Disord*. 2012;27(1):90–97.

[140] Zhao DD, Zhou HY, Wu QZ, Liu J, Chen XY, He D, He XF, Han WJ, and Gong QY. Diffusion tensor imaging characterization of occult brain damage in relapsing neuromyelitis optica using 3.0T magnetic resonance imaging techniques. *Neuroimage*. 2012;59(4):3173–3177.

[141] Zivadinov R, Brown MH, Schirda CV, Poloni GU, Bergsland N, Magnano CR, Durfee J, Kennedy C, Carl E, Hagemeier J, Benedict RH, Weinstock-Guttman B, and Dwyer MG. Abnormal subcortical deep-gray matter susceptibility-weighted imaging filtered phase measurements in patients with multiple sclerosis: A case-control study. *Neuroimage*. 2012; 59(1):331–339.

Appendix A

Herein we present two impacted publications directly related to the work in this dissertation. The first, published in *JMRI*, describes our work in investigating the effect of superparamagnetic ferritin-bound on diffusion tensor-derived scalars. We present our *in vitro* results, validated *in vivo* in healthy control subjects. The second paper, published in *Magma*, covers our work in evaluating qualitative and quantitative MRI measures, including DTI, in ALS subjects and healthy controls.

Original Research

Chasing Shadows: What Determines DTI Metrics in Gray Matter Regions? An In Vitro and In Vivo Study

Aaron M. Rulseh, MD,[1] Jiří Keller, MD,[1,2] Jaroslav Tintěra, PhD,[3] Milan Kožíšek, PhD,[4] and Josef Vymazal, MD, DSc[1,5*]

Purpose: To characterize the relationship between superparamagnetic ferritin-bound iron and diffusion tensor scalars in vitro, and validate the results in vivo.

Materials and Methods: The in vitro model consisted of a series of 40-mL 1.1% agarose gels doped with ferritin covering and exceeding those concentrations normally found within healthy human gray matter. Additionally, regions of interest were placed in the caudate, putamen, and globus pallidus of 29 healthy volunteer subjects 19–80 years of age. Carr-Purcell-Meiboom-Gill sequence (CPMG) and diffusion tensor imaging (DTI) data were collected at 1.5 Tesla (T) and 3T in vitro, and at 1.5T in vivo.

Results: In vitro, linear relationships were observed between ferritin-bound iron concentration, R_2 ($1/T_2$) and 1/SNR. Eigenvalue repulsion with increasing R_2 (decreasing SNR) was reflected in an artifactual increase of fractional anisotropy. In vivo, similar relationships were observed, with mean diffusivity also decreasing linearly with increasing R_2. Lambda 3 showed the strongest correlation with R_2 both in vitro and in vivo.

Conclusion: The observation that DTI metrics correlate with ferritin-bound iron is an important consideration in the design and interpretation of studies exploring the diffusion characteristics of gray matter regions, especially in studies focused on adolescence as well as diseases associated with altered brain-iron load such as pantothenate kinase-associated neurodegeneration, Huntington disease and multiple system atrophy.

Key Words: diffusion tensor imaging; brain iron; T_2 relaxation; basal ganglia; fractional anisotropy; mean diffusivity
J. Magn. Reson. Imaging 2013; 000:000–000.
© 2013 Wiley Periodicals, Inc.

DIFFUSION TENSOR IMAGING (DTI) has become an invaluable tool in probing the morphological and functional characteristics of the brain in both clinical and research settings. Several scalar invariants may be derived from the diffusion tensor to characterize proton diffusion, with fractional anisotropy (FA) and mean diffusivity (MD) being most commonly reported. DTI studies most often target the white matter of the brain due to its highly anisotropic structure, and have shown clinical utility in monitoring disease progression and improving the diagnostic process (e.g., 1–3). The gray matter of the brain is relatively isotropic on the voxel scale; therefore, DTI is not ideally suited to characterize proton diffusion in this tissue. However, some investigators have reported changes in gray matter DTI metrics and have proposed various mechanisms to explain their observations involving hypothetical structural changes (e.g., 4–14). The presence of iron in the gray matter has also been suggested to affect DTI measurements (15,16).

Healthy gray matter is characterized by age-related iron accumulation, with the greatest accrual occurring before 30 years of age (17). The highest amount of iron per tissue weight is found in the globus pallidus where its level exceeds that in the liver by almost a factor of 2. Other gray matter regions high in iron, in decreasing order, are the red nucleus, substantia nigra, putamen, dentate nucleus, caudate nucleus, thalamus, and various cortical regions (17,18). Iron is also found in the white matter in amounts comparable to or less than cortical regions (17) and is not distributed evenly, but aggregated in patches of iron-rich cells myelinating the subcortical U-fibers at the border of the cortex and white matter (19). In addition to changes associated with healthy aging, the concentration and form of iron may change in several chronic neurological diseases, most notably

[1]Department of Radiology, Na Homolce Hospital, Prague, Czech Republic.
[2]Department of Neurology, Charles University in Prague, 3rd Faculty of Medicine, Prague, Czech Republic.
[3]Department of Radiology, Institute for Clinical and Experimental Medicine, Prague, Czech Republic.
[4]Institute of Organic Chemistry and Biochemistry, Academy of Sciences of the Czech Republic, Gilead Sciences and IOCB Research Center, Prague, Czech Republic.
[5]Department of Neurology and Center of Clinical Neuroscience, Charles University in Prague, 1st Faculty of Medicine, Prague, Czech Republic.
Contract grant sponsor: IGA; Contract grant numbers: NT11328-4/2010, NT12094-5/2011; Contract grant sponsor: Research Project MSM; Contract grant number: 0021620849; Contract grant sponsor: Research Project Charles University in Prague; Contract grant number: PRVOUK P34; Contract grant sponsor: Grant Agency of the Czech Republic; Contract grant number: P207/11/1798.
*Address reprint requests to: J.V., Na Homolce Hospital, Roentgenova 2, 15030 Prague 5, Czech Republic. E-mail: josef.vymazal@homolka.cz
Received February 1, 2012; Accepted January 10, 2013.
DOI 10.1002/jmri.24065
View this article online at wileyonlinelibrary.com.

© 2013 Wiley Periodicals, Inc.

in those of neurodegenerative origin (20,21). Abnormal brain-iron status has also been observed in other diseases such as multiple sclerosis (22), restless legs syndrome (23), and attention deficit hyperactivity disorder (24).

Ferritin-bound iron is the principal storage form of physiologic brain iron (25), and exhibits superparamagnetic behavior at room and body temperatures (26). Ferritin is a large water-soluble molecule with a molecular weight of approximately 450,000 g/mol, and is a spherical assembly of 24 peptide subunits approximately 80 Å in diameter. One molecule of ferritin is able to scavenge up to 4500 atoms of iron (the loading factor). The loading factors in vivo are usually lower at approximately 2500 atoms of iron. Ferritin is found primarily in oligodendrocytes, and to a lesser extent in microglia, astrocytes, and neurons (19,27). The degradation product of ferritin is hemosiderin, which is water-insoluble and can be distinguished from ferritin to a certain extent by magnetic resonance imaging (MRI) (28).

MRI is sensitive to the presence of superparamagnetic iron as it shortens T_2 relaxation time. This effect, which is dependent on the strength of a given field, has been exploited for many years to quantify brain iron. The Carr-Purcell-Meiboom-Gill sequence (CPMG) and the field dependent R_2 increase (FDRI) are two such methods used in clinical and research settings that take advantage of the effect of iron on T_2 relaxation time. Spin-echo echo-planar imaging (SE-EPI) is the most frequently used sequence in acquiring data for DTI, and as it is T_2-weighted, the attenuation of signal in iron-rich areas of the brain can be readily appreciated in these images by visual inspection.

Considering the observation that DTI measurements in the iron-rich extrapyramidal nuclei correlate with iron levels reported in postmortem studies (16), we hypothesized that ferritin molecules loaded with iron may change the diffusion-scalar values in a systematic way. To test our hypothesis, we created an in vitro model consisting of agarose gel phantoms doped with ferritin, and validated our results in vivo on healthy volunteers.

MATERIALS AND METHODS

Agarose Gel Phantoms

A series of 40-mL 1.1% agarose gels were prepared at physiologic pH (7.4). The 1.1% concentration of agarose was chosen to approximate the FA characteristics brain gray matter. Agarose (Serva, Germany) was dissolved when boiled in a 50-mM Tris-HCL buffer (pH 7.4) in individual falcon tubes 115 mm in length and 26 mm in diameter. As the gels cooled to 50°C, horse-spleen ferritin (Sigma-Aldrich, St. Louis, MO) was added to the individual falcon tubes and allowed to distribute evenly. Ferritin was added in 5 mg iron/100 mL increments up to 50 mg iron/100 mL, covering and exceeding those concentrations normally found within healthy human gray matter (composition of ferritin solution: 56 mg/mL ferritin, 7.1 mg/mL iron). One gel was left as a control and was allowed to cool without the addition of ferritin. The phantoms were positioned perpendicular to the B0 field and scanned in a climate-controlled environment at 23°C.

Volunteer Subjects

A total of 29 volunteer subjects, 19–80 years of age (14 male, 15 female; mean age 53.2 years ± 17 SD) were enrolled in the study. All volunteers were recruited from the community and determined to be free of neurological disease, with no lesions detected on structural MR images. The study was approved by the local ethics committee and all participants provided signed, informed consent.

MR Protocol

In vitro images were acquired on Siemens Avanto 1.5 Tesla (T) and Siemens Trio 3-Tesla systems equipped with Quantum gradients (Erlangen, Germany), with a standard 12-channel head coil. Single shot SE-EPI diffusion weighted imaging (DWI) was performed with 30 noncollinear gradient directions at 1.5T (b = 1100 s/mm^2; repetition time [TR] = 8800 ms, echo time [TE] = 98 ms; number of excitations [NEX] = 2; Matrix = 128 × 128; field of view [FOV] = 280 × 280 mm; Phase encode = AP/PA; Bandwidth = 1345 Hz/px; Parallel acquisition [GRAPPA] acceleration factor = 2; Voxel size 2.2 mm isotropic) and 3T (b = 1100 s/mm^2; TR = 10100 ms, TE = 98 ms; NEX = 1; Matrix = 146 × 146; FOV = 252 × 252 mm; Phase encode = AP/PA; Bandwidth = 1370 Hz/px; Parallel acquisition [GRAPPA] acceleration factor = 2; Voxel size 1.9 mm isotropic). The voxel size in the 3T SE-EPI sequence was reduced to compensate for higher signal-to-noise ratio (SNR) at 3T. In vivo SE-EPI was performed on the same 1.5-Tesla System with the parameters stated above, but only data in the AP phase encode direction were collected. Structural MR images were acquired in volunteer subjects using standard T_2-weighted, FLAIR, and T_2*-weighted sequences, and were used to exclude pathology.

All volunteers and phantoms were also scanned with a single-slice Carr-Purcell-Meiboom-Gill (CPMG) sequence (32 interecho times of 12.5, 25.0, 37.5 to 400.0 ms; TR = 3000 ms; In-plane resolution 0.9 × 0.9 mm; Slice thickness 4 mm). In human subjects placement was guided by the slice position of the whole-head T2 sequence, and the CPMG slice was placed in the axial plane approximately parallel to the plane passing through the anterior/posterior commissures to optimally cover the basal ganglia. In phantoms the slice was placed in approximately the middle of the tube, perpendicular to the long axis.

Postprocessing and Data Evaluation

All diffusion weighted images were processed offline in FSL 4.1 (29). In vivo data were subjected to EPI correction, followed by brain extraction using BET (30). Dtifit was then used to calculate the tensor scalars by the default least squares method, producing

λ1-3, FA, and MD volumes that were used in further analyses. A single-slice CPMG image of corresponding TE was used for 2D coregistration of CPMG to T_2. The raw T_2 image without diffusion weighting generated by dtifit was then linearly coregistered to the whole-head T_2, and the transform was applied to the tensor maps created by dtifit. A single slice (corresponding to CPMG) was then extracted from the resulting volumes. This approach produced single coregistered slices (λ1-3/FA/MD/T_2/CPMG). In FSLView, masks of the globus pallidus, putamen, and caudate were created on the CPMG data by a single observer (JV) and placed well within the nuclei to avoid partial-volume effects (Fig. 1). In one subject the caudate nuclei, and in seven subjects the globus pallidi were not sufficiently covered by the CPMG slice and were, therefore, not included. The average signal data for each echo time were stored, generating 32 intensity values for each mask. We performed nonlinear regression of CPMG data selected by each mask using a plateau followed by monoexponential decay model for average signal intensity and interecho time with GraphPad Prism 5 (GraphPad Software Inc., La Jolla, CA). The masks created on the CPMG data were also projected to the coregistered λ1-3/FA/MD maps. Proton density (PD) was calculated for each echo-time 0 per ROI. SNR was determined on a per-ROI basis by dividing mean intra-ROI signal intensity by the SD in a noise ROI, and multiplying by 0.655 to correct for the Rician distribution of noise in magnitude images (31). ROIs were evaluated in both hemispheres and then averaged.

In vitro SE-EPI data were corrected by applying a displacement field generated by estimating the displacement in each voxel from data acquired in opposite phase-encode directions (32). Dtifit was then used to calculate the tensor scalars and produce λ1-3/FA/MD maps as above (Fig. 2). Measurements were performed in ImageJ viewer (33), with ROIs of equal size placed directly on the diffusion-weighted and CPMG data, selecting a narrow column in the center of the tube. ROIs created on the diffusion-weighted data were then projected on the λ1-3/FA/MD maps, and SNR was determined as above. CPMG measurements were processed in the same manner as the in vivo data.

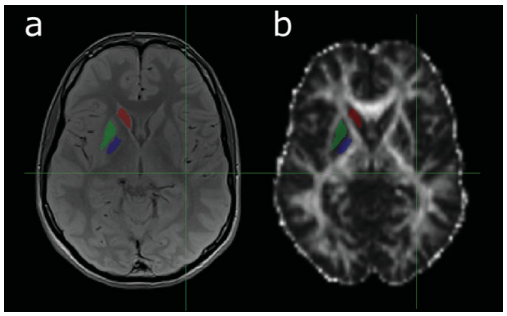


Figure 1. CPMG data from one healthy volunteer showing ROIs placed in the right caudate, putamen and globus pallidus(**a**), and corresponding coregistered FA data (**b**).

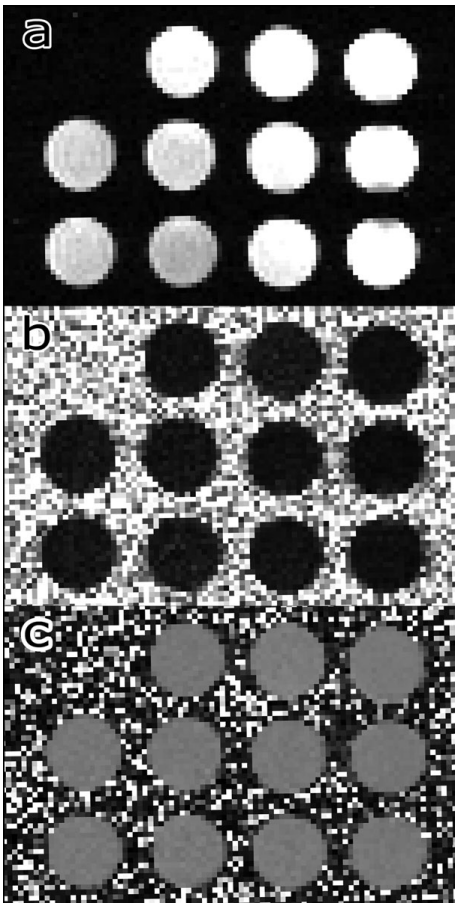


Figure 2. In vitro (1.5T) images: B0 (**a**), fractional anisotropy (**b**), and mean diffusivity (**c**) maps.

Statistical Analysis

Statistical analyses were performed in R (34). Handedness information was not available for all volunteers, therefore the mean of right and left measurements was used in the in vivo analyses. The Sidak correction for multiple comparisons (D/AP procedure) was applied to maintain an alpha level of $P < 0.05$. A power analysis was performed to ensure statistical power of at least 80%. A reciprocal transformation was applied to SNR data to achieve a linear relationship with other variables, and was used in all analyses. Analysis of variance (ANOVA) analysis of successive linear, quadratic and cubic models was used in determining the best model to fit the data. The Wilcoxon rank-sum test was used to examine gender differences.

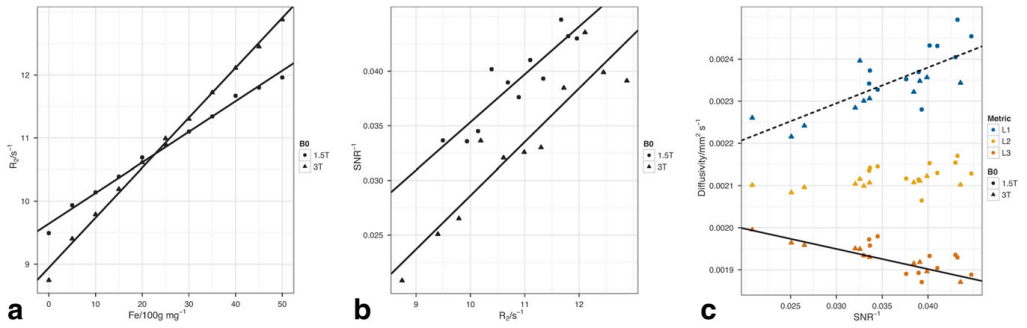


Figure 3. In vitro results: Linear dependence of R_2 on ferritin-bound iron at 1.5T and 3T (**a**); linear dependence of 1/SNR on R_2 at 1.5T and 3T (**b**); Eigenvalues (λ1–λ3) as a function of 1/SNR (**c**). Fe, ferritin-bound iron; SNR, signal-to-noise ratio.

RESULTS

In Vitro Results

A linear dependence of R_2 ($1/T_2$) on ferritin-bound iron concentration was observed in vitro at 1.5T and 3T (Fig. 3a; 1.5T: $R^2 = 0.99$, $P < 0.001$; 3T: $R^2 = 0.99$, $P < 0.001$). 1/SNR was observed to increase linearly with increasing iron concentration and R_2 (Fig. 3b; 1.5T: $R^2 = 0.80$, $P < 0.001$; 3T: $R^2 = 0.86$, $P < 0.001$). In examining the linear relationship between the Eigenvalues (λ1–3) and 1/SNR (Fig. 3c), only the fit between λ3 and 1/SNR at 3T was significant ($R^2 = 0.92$, $P < 0.001$), although there was a trend between λ1 and 1/SNR (3T: $R^2 = 0.49$, $P = 0.08$). Correlation between the Eigenvalues and R_2 was similar (Fig. 4a), with the fit between λ3 and R_2 significant at 3T ($R^2 = 0.70$, $P = 0.006$) and a trend between λ1 and R_2 (3T: $R^2 = 0.53$, $P = 0.06$). A linear correlation was observed between FA and 1/SNR at both field strengths (1.5T: $R^2 = 0.74$, $P = 0.004$; 3T: $R^2 = 0.84$, $P < 0.001$), and between FA and R_2 at 3T only (Fig. 4b; 1.5T: $R^2 = 0.40$, $P = 0.17$; 3T: $R^2 = 0.76$, $P = 0.002$). No changes in MD were detected (Fig. 4c).

In Vivo Results

A linear dependence of 1/SNR on R_2 was observed in vivo ($R^2 = 0.67$, $P < 0.001$). The Eigenvalues decreased linearly with increasing R_2 (Fig. 5a; λ1: $R^2 = 0.10$, $P = 0.03$; λ2: $R^2 = 0.36$, $P < 0.001$; λ3: $R^2 = 0.58$, $P < 0.001$), and a similar pattern was seen between the Eigenvalues and 1/SNR, although the fit with λ1 was not significant (λ1: $R^2 = 0.02$, $P = 0.56$; λ2: $R^2 = 0.17$, $P < 0.001$; λ3: $R^2 = 0.34$, $P < 0.001$). As in vitro, FA increased with increasing 1/SNR ($R^2 = 0.34$, $P < 0.001$) and R_2 (Fig. 5b; $R^2 = 0.51$, $P < 0.001$), with stronger correlation between FA and R_2. MD decreased with increasing 1/SNR ($R^2 = 0.19$, $P < 0.001$) and R_2 (Fig. 5c; $R^2 = 0.39$, $P < 0.001$), again with stronger correlations between MD and R_2. PD correlated only weakly with R_2 ($R^2 = 0.15$, $P = 0.003$), FA ($R^2 = 0.22$, $P < 0.001$), and λ3 ($R^2 = 0.13$, $P = 0.006$). In individual nuclei, correlations were only observed in the globus pallidus between diffusion metrics and R_2 (λ1: $R^2 = 0.46$, $P = 0.004$; λ2: $R^2 = 0.39$, $P = 0.013$; λ3: $R^2 = 0.43$, $P = 0.006$; MD: $R^2 = 0.53$, $P < 0.001$). Correlation between age and

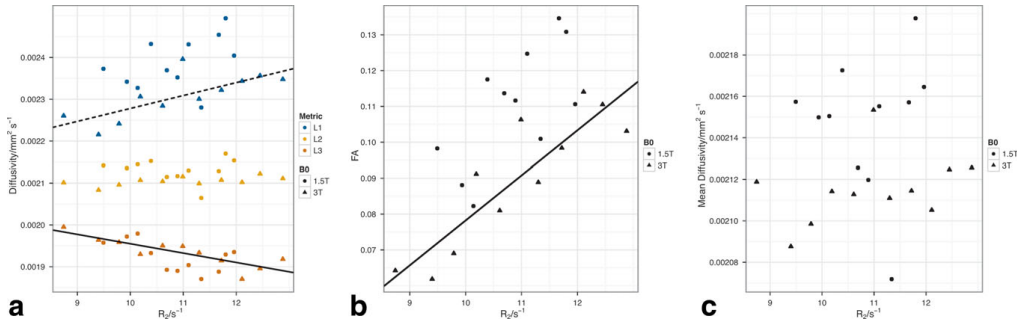


Figure 4. In vitro results: Eigenvalues (λ1–λ3) plotted as a function of R_2 (**a**); FA as a function of R_2 (**b**); MD as a function of R_2 (**c**). FA, fractional anisotropy; MD, mean diffusivity.

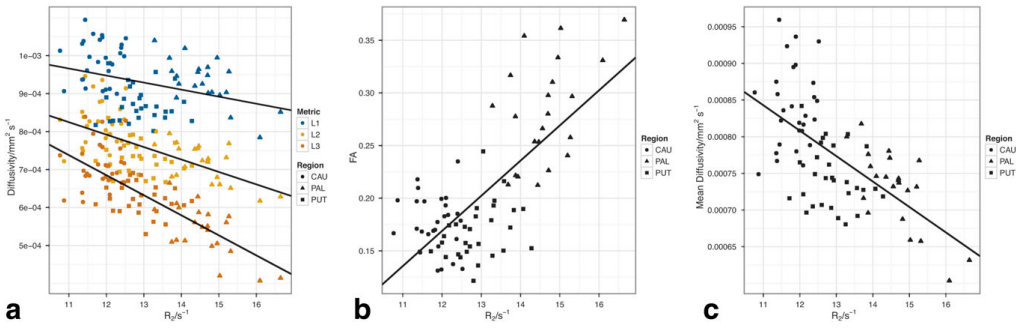


Figure 5. In vivo results: Eigenvalues (λ1–λ3) plotted as a function of R_2 (**a**); linear dependence of FA on R_2 (**b**); linear dependence of MD on R_2 (**c**). FA, fractional anisotropy; MD, mean diffusivity; CAU, caudate; PUT, putamen; PAL, globus pallidus.

tensor-derived scalars was only observed in the putamen (λ1: $R^2 = 0.42$, $P = 0.001$; λ2: $R^2 = 0.25$, $P = 0.036$; MD: $R^2 = 0.29$, $P = 0.019$). No correlations between age and other covariates were observed in pooled data, nor were any group-wise differences between genders detected.

DISCUSSION

To the best of our knowledge, this is the first study showing both the in vitro and in vivo influence of metalloprotein-bound iron on DTI metrics. Our investigation was prompted by the initial observation that FA in gray matter regions measured in vivo appeared to roughly correlate with iron concentrations (15,16) reported in postmortem studies (17). Ferritin-bound iron, R_2, and 1/SNR were included as covariates as they represent a possible continuum of cause to effect, although these variables are not strictly dependent on each other. As superparamagnetic iron decreases T_2 relaxation time (increases R_2), SNR decreases (1/SNR increases) on SE-EPI data.

Our in vitro data illustrate the isolated effect of ferritin-bound iron, mediated by iron-dependent signal attenuation. Eigenvalue repulsion with decreasing SNR has been well documented (e.g., 35,36), and although only changes in λ3 were significant at 3T, there was a clear visual trend of Eigenvalue repulsion that was reflected in FA changes. FA increased with increasing 1/SNR (decreasing SNR) and R_2, while MD was shown to be insensitive to these changes in vitro. These findings are supported by our in vivo data where similar correlations were observed. Linear dependencies between tensor-derived scalars and 1/SNR and R_2 were achieved in pooled data, with FA increasing and MD decreasing as 1/SNR and R_2 increased.

Differences between in vivo and in vitro results may be related to differences in the composition of agarose gel in comparison to the underlying cytoarchitecture of the gray matter. Previous studies have demonstrated the dependence of Eigenvalue repulsion on the inherent anisotropy of a medium (35,36). We arrived at the composition of our in vitro model after experimentally determining the concentration of agarose that approximates the anisotropy of gray matter free of artifactual contamination. Although the agarose model is a close approximation to gray matter, the behavior of individual Eigenvalues is likely sensitive to even subtle differences.

Other factors must be taken into consideration when attempting to interpret differences between the in vivo and in vitro results. The in vivo environment is more complex, with many factors that could contribute to DTI measurements such as the presence of myelinated fibers in gray matter structures and physiological noise. Furthermore, the clustering effect of ferritin in vivo increases magnetic inhomogeneity. R_2 is also not only dependent on iron content, but is affected by several factors such as temperature, tissue density, and water content (35–37). We included PD in our study to control for tissue density and water content, and that PD did not make a significant contribution to the results supports the hypothesis that ferritin-bound iron played a key role the observed correlations. λ3 showed the strongest correlation with R_2 both in vitro and in vivo (Figs. 4 and 5), seemingly the least affected by confounding factors in vivo. λ3 measurements within the individual nuclei followed R_2 values (Fig. 6), while FA and MD values proved less specific. The pattern observed in FA values within the basal ganglia is in agreement with previously published data (38).

Several studies examining the DTI characteristics of gray matter regions have been published in recent years, with various mechanisms proposed to explain their observations involving hypothetical structural changes (e.g., 4–14). More specific examples include the loss of myelinated fibers passing through gray matter structures (5,9), neuronal and dendrite elimination with age (10) and the targeted loss of certain dendrite connections leading to increased anisotropy (7), as well as tissue compaction and gliosis associated with aging (12). Our results show that ferritin-bound iron makes an important contribution to DTI metrics in low-signal, isotropic, iron-rich regions, which is an important consideration in studies examining the DTI characteristics of gray matter regions, especially in studies focused on adolescence as well

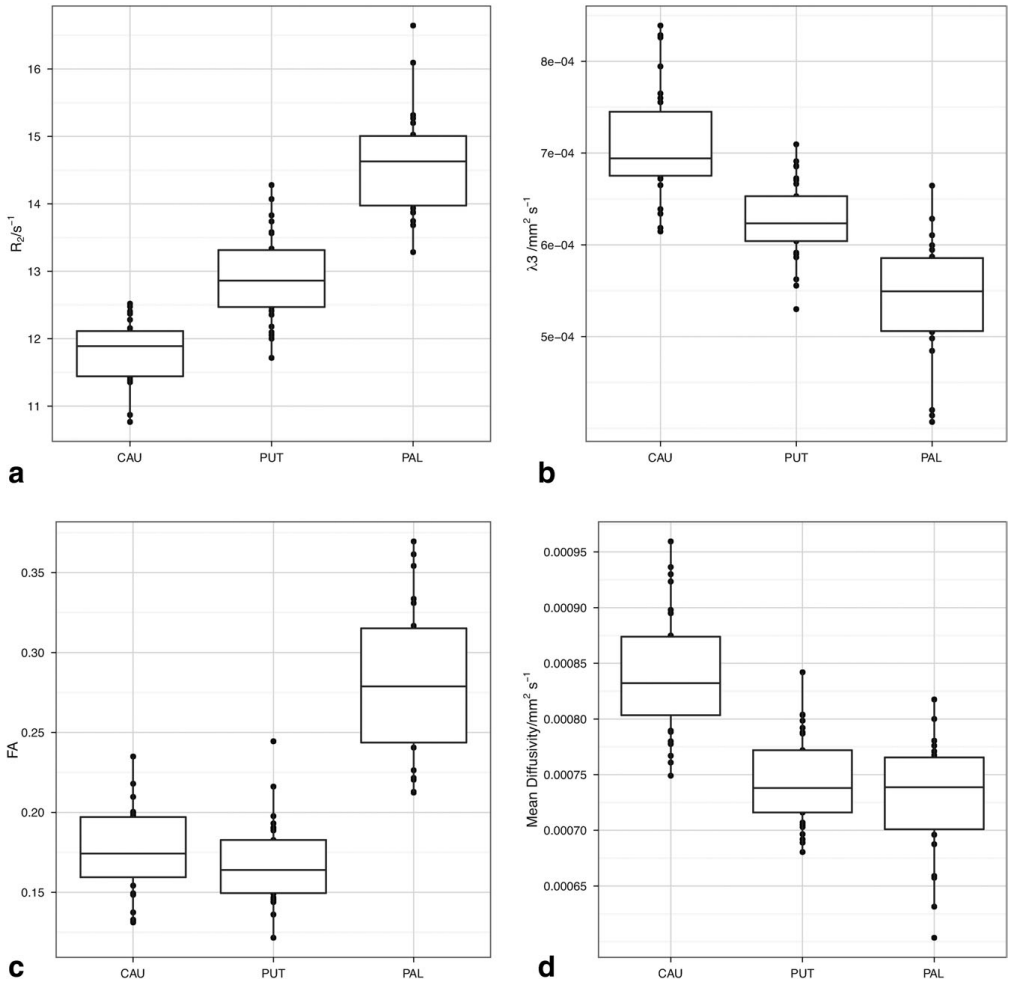


Figure 6. In vivo results: Box plots showing values of R_2 (**a**), λ3 (**b**), FA (**C**), and MD (**d**) in individual nuclei. FA, fractional anisotropy; MD, mean diffusivity; CAU, caudate; PUT, putamen; PAL, globus pallidus.

as diseases associated with altered brain-iron load such as pantothenate kinase-associated neurodegeneration (PKAN), Huntington disease and multiple system atrophy (MSA). Based on our in vitro findings, we would expect that a fifty percent increase in R_2 would result in a 75% increase in FA. This estimate is roughly in agreement with our in vivo observations. As a practical example, the globus pallidus has a mean R_2 of 14–15 and a mean FA of approximately .28 in healthy adults. In Huntington disease, R_2 in the globus pallidus may reach 21 (J. Vymazal, unpublished data), and in such a patient we would expect a corresponding FA of approximately .50. Additional confounding factors, as discussed previously, would be expected to make further contributions.

It has been reported that the iron content of gray matter may be dependent on age (6,7,12,17,39–41). Hallgren and Sourander reported increasing iron with age in several gray matter regions, plateauing at approximately age thirty (17). That we only observed significant correlations with age in the putamen is not surprising for several reasons. Our volunteer group was composed of older adults in comparison to previous studies, and although iron does continue to accumulate throughout the lifespan, it occurs over a limited range beyond 30 years of age. Notably, the most gradual accumulation in the regions we examined occurs in the putamen. Most importantly, our study is only sufficiently powered to detect large changes in the individual regions examined. More subtle changes

across the age range in our study would require a much larger sample to be appreciated.

In conclusion, ferritin-bound iron in the gray matter of the brain affects DTI metrics in vivo. Iron-dependent signal attenuation reflected in increased R_2 and decreased SNR results in systematic, artifactual changes in tensor-derived scalars. This observation has important implications for DTI studies targeting gray matter regions, especially in studies focused on adolescence as well as diseases associated with altered brain-iron load such as PKAN, Huntington disease and MSA. The influence of superparamagnetic iron on DTI metrics should be considered when interpreting and planning DTI studies that target gray matter regions.

ACKNOWLEDGMENTS

The authors thank Prof. Jan Konvalinka, PhD for guidance in preparing the in vitro model, and Peter van Gelderen, PhD for insightful methodological suggestions. M.K. was supported by the Center for New Antivirals and Antineoplastics from the Ministry of Education of the Czech Republic.

REFERENCES

1. Rose SE, Chen F, Chalk JB, et al. Loss of connectivity in Alzheimer's disease: an evaluation of white matter tract integrity with colour coded MR diffusion tensor imaging. J Neurol Neurosurg Psychiatry 2000;69:528–530.
2. Head D, Buckner RL, Shimony JS, et al. Differential vulnerability of anterior white matter in nondemented aging with minimal acceleration in dementia of the Alzheimer type: Evidence from diffusion tensor imaging. Cereb Cortex 2004;14:410–423.
3. Prakash N, Hageman N, Hua X, Toga AW, Perlman SL, Salamon N. Patterns of fractional anisotropy changes in white matter of cerebellar peduncles distinguish spinocerebellar ataxia-1 from multiple system atrophy and other ataxia syndromes. Neuroimage 2009;47(Suppl);2:T72–T81.
4. Barnea-Goraly N, Menon V, Eckert M, et al. White matter development during childhood and adolescence: A cross-sectional diffusion tensor imaging study. Cereb Cortex 2005;15:1848–1854.
5. Rosas HD, Tuch DS, Hevelone ND, et al. Diffusion tensor imaging in presymptomatic and early Huntington's disease: selective white matter pathology and its relationship to clinical measures. Mov Disord 2006;21:1317–1325.
6. Càmara E, Bodammer N, Rodraíguez-Fornells A, Tempelmann C. Age-related water diffusion changes in human brain: a voxel-based approach. Neuroimage 2007;34:1588–1599.
7. Hasan KM, Halphen C, Boska MD, Narayana PA. Diffusion tensor metrics, T2 relaxation, and volumetry of the naturally aging human caudate nuclei in healthy young and middle-aged adults: possible implications for the neurobiology of human brain aging and disease. Magn Reson Med 2008;59:7–13.
8. Lebel C, Walker L, Leemans A, Phillips L, Beaulieu C. Microstructural maturation of the human brain from childhood to adulthood. Neuroimage 2008;40:1044–1055.
9. Douaud G, Behrens TE, Poupon C, et al. In vivo evidence for the selective subcortical degeneration in Huntington's disease. Neuroimage 2009;46:958–966.
10. Hasan KM, Halphen C, Kamali A, Nelson FM, Wolinsky JS, Narayana PA. Caudate nuclei volume, diffusion tensor metrics, and T2 relaxation in healthy adults and relapsing-remitting multiple sclerosis patients: Implications to understanding gray matter degeneration. J Magn Reson Imaging 2009;29:70–77.
11. Wang J, Wai Y, Lin W, et al. Microstructural changes in patients with progressive supranuclear palsy: A diffusion tensor imaging study. J Magn Reson Imaging 2010;32:69–75.
12. Wang Q, Xu X, Zhang M. Normal aging in the basal ganglia evaluated by eigenvalues of diffusion tensor imaging. AJNR Am J Neuroradiol 2010;31:516–520.
13. Zhao D, Zhou H, Wu Q, et al. Diffusion tensor imaging characterization of occult brain damage in relapsing neuromyelitis optica using 3.0T magnetic resonance imaging techniques. Neuroimage 2012;59:3173–3177.
14. Zhan W, Kang GA, Glass GA, et al. Regional alterations of brain microstructure in Parkinson's disease using diffusion tensor imaging. Mov Disord 2012;27:90–97.
15. Pfefferbaum A, Adalsteinsson E, Rohlfing T, Sullivan EV. Diffusion tensor imaging of deep gray matter brain structures: effects of age and iron concentration. Neurobiol Aging 2010;31:482–493.
16. Keller J, Rulseh AM, Syka M, Vymazal J. Fractional anisotropy in various white and gray matter regions in adulthood. Dependence on age and comparison of two DTI sequences. In: Proceedings of the 18th Annual Meeting of ISMRM, Stockholm, 2010. (abstract 1560).
17. Hallgren B, Sourander P. The effect of age on the non-haemin iron in the human brain. J Neurochem 1958;3:41–51.
18. Haacke EM, Cheng NYC, House MJ, et al. Imaging iron stores in the brain using magnetic resonance imaging. Magn Reson Imaging 2005;23:1–25.
19. Connor JR, Menzies SL, Burdo JR, Boyer PJ. Iron and iron management proteins in neurobiology. Pediatr Neurol 2001;25: 118–129.
20. Zecca L, Youdim MBH, Riederer P, Connor JR, Crichton RR. Iron, brain ageing and neurodegenerative disorders. Nat Rev Neurosci 2004;5:863–873.
21. Vymazal J, Righini A, Brooks RA, et al. T1 and T2 in the brain of healthy subjects, patients with Parkinson disease, and patients with multiple system atrophy: relation to iron content. Radiology 1999;211:489–495.
22. Zivadinov R, Heininen-Brown M, Schirda CV, et al. Abnormal subcortical deep-gray matter susceptibility-weighted imaging filtered phase measurements in patients with multiple sclerosis: A case-control study. Neuroimage 2012;59:331–339.
23. Earley CJ, Barker PB, Horská A, Allen RP. MRI-determined regional brain iron concentrations in early- and late-onset restless legs syndrome. Sleep Med 2006;7:458–461.
24. Cortese S, Azoulay R, Castellanos FX, et al. Brain iron levels in attention-deficit/hyperactivity disorder: A pilot MRI study. World J Biol Psychiatry 2012;13:223–231.
25. Vymazal J, Brooks RA, Baumgarner C, et al. The relation between brain iron and NMR relaxation times: An in vitro study. Magn Reson Med 1996;35:56–61.
26. Brooks RA, Vymazal J, Goldfarb RB, Bulte JW, Aisen P. Relaxometry and magnetometry of ferritin. Magn Reson Med 1998;40: 227–235.
27. Connor JR, Menzies SL. Cellular management of iron in the brain. J Neurol Sci 1995;134:33–44.
28. Vymazal J, Urgošík D, Bulte JWM. Differentiation between hemosiderin- and ferritin-bound brain iron using nuclear magnetic resonance and magnetic resonance imaging. Cell Mol Biol (Noisy-le-grand) 2000;46:835–842.
29. Smith SM, Jenkinson M, Woolrich MW, et al. Advances in functional and structural MR image analysis and implementation as FSL. Neuroimage 2004;23(Suppl):S208–S219.
30. Smith SM Fast robust automated brain extraction. Hum Brain Mapp 2002;17:143–155.
31. Edelstein WA, Bottomley PA, Pfeifer LM. A signal-to-noise calibration procedure for NMR imaging systems. Med Phys 1984;11: 180–185.
32. Holland D, Kuperman JM, Dale AM. Efficient correction of inhomogeneous static magnetic field-induced distortion in echo planar imaging. Neuroimage 2010;50:175–183.
33. Magelhaes PJ, Ram SJ, Abramoff MD. Image processing with ImageJ. Biophotonics International 2004;11:36–42.
34. R Development Core Team. R: a language and environment for statistical computing.Vienna, Austria: R foundation for statistical computing; 2011.
35. Pierpaoli C, Basser PJ. Toward a quantitative assessment of diffusion anisotropy. Magn Reson Med 1996;36:893–906.
36. Bastin ME, Armitage PA, Marshall I. A theoretical study of the effect of experimental noise on the measurement of anisotropy in diffusion imaging. Magn Reson Imaging 1998;16:773–785.

37. Bartzokis G, Mintz J, Sultzer D, et al. In vivo MR evaluation of age-related increases in brain iron. AJNR Am J Neuroradiol 1994;15:1129–1138.
38. Hasan KM, Walimuni IS, Abid H, et al. DTI, T2 relaxation and volumetry of the human brain corpus striatum across the life-span. In: Proceedings of the 18th Annual Meeting of ISMRM, Stockholm, 2010. (abstract 606).
39. Bartzokis G, Beckson M, Hance DB, Marx P, Foster JA, Marder SR. MR evaluation of age-related increase of brain iron in young adult and older normal males. Magn Reson Imaging 1997;15: 29–35.
40. Bartzokis G, Tishler TA, Lu PH, et al. Brain ferritin iron may influence age- and gender-related risks of neurodegeneration. Neurobiol Aging 2007;28:414–423.
41. Hasan KM, Frye RE. Diffusion tensor-based regional gray matter tissue segmentation using the international consortium for brain mapping atlases. Hum Brain Mapp 2011;32:107–117.

Magn Reson Mater Phy
DOI 10.1007/s10334-010-0237-4

RESEARCH ARTICLE

Quantitative brain MR imaging in amyotrophic lateral sclerosis

Jiří Keller · Josef Vymazal · Petr Ridzoň · Robert Rusina · Petr Kulišťák · Hana Malíková · Aaron M. Rulseh · Otakar Keller · Robert Jech

Received: 8 July 2010 / Revised: 26 November 2010 / Accepted: 29 November 2010
© The Author(s) 2011. This article is published with open access at Springerlink.com

Abstract
Object To evaluate the potential of quantitative MR techniques [voxel-based morphometry (VBM), T2-relaxometry, mean diffusivity (MD), fractional anisotropy (FA)] in the diagnostics of amyotrophic lateral sclerosis (ALS).
Materials and methods Thirty-three ALS patients and thirty age- and sex-matched healthy volunteers were included in the cross-sectional study. T1WI, T2WI and T2 relaxometry sequences were performed at 1.5T. DWI was performed in a subgroup of 12 patients. Disease severity was estimated with the ALS Functional Rating Scale (ALS-FRS).
Results We detected decreased T2 relaxation rate (R2) in the frontal white matter (FWM) (left and right $P < 0.005$) and caudate nucleus (left $P < 0.005$) in ALS patients. R2 in the FWM correlated with age in patients and controls. A correlation ($P < 0.01$, cluster-level corrected) between atrophy in the corona radiata and the limb ALS-FRS subset was found, as well as a difference between patients and controls in this area. No correlation between FA/MD and ALS-FRS was observed in the T2 hyperintense region of the posterior limb of the internal capsule (PLIC), or in the site of atrophy detected by VBM. No R2 or PD changes in the PLIC were detected. TBSS revealed decreased FA in the corona radiata and callosal body.
Conclusions Decreased R2 in the left caudate and bilateral FWM may help in the diagnostic process and disqualifies these regions as internal controls in ALS studies. The PLIC is not a reliable diagnostic marker of ALS.

Keywords Amyotrophic lateral sclerosis · T2 relaxation time · Fractional anisotropy · Voxel-based morphometry · ALS-FRS · Caudate · Frontal white matter · R2

Introduction

Amyotrophic lateral sclerosis (ALS) is the most common motor neuron disease (MND)—a group of neurological disorders which selectively affect upper and lower motor neurons. This disease carries a fatal prognosis, its aetiology is still little understood, and no specific treatment yet exists. Traditionally, ALS has been described as a neurodegenerative disorder primarily affecting motor neurons in the anterior horns of the spinal cord, bulbar nuclei and cerebral motor cortex [1–3], with secondary degeneration of the emerging tracts of both the central and peripheral nervous systems [4]. Clinically, two forms of ALS may be distinguished according to the site of dominant involvement: a limb-onset and a bulbar-onset form. During the span of the disease, both forms include progressive muscle weakness, including the muscles needed for speech, swallowing and breathing.

Preliminary data were presented on ESMRMB meeting in Antalya in 2009 as a lecture (abstract: Keller J, Vymazal J, Jech R, Ridzoň P, Rusina R, Keller O: Quantitative MR Imaging in amyotrophic lateral sclerosis. Magma Magn Reson Mater Phys Biol Med, 2009, 22, Suppl. 1, p.131).

J. Keller
Third Faculty of Medicine, Charles University in Prague, Prague, Czech Republic

J. Keller · J. Vymazal (✉) · H. Malíková · A. M. Rulseh
Department of Radiology, Na Homolce Hospital, 150 30 Prague 5, Czech Republic
e-mail: josef.vymazal@homolka.cz

J. Vymazal · R. Jech
Department of Neurology and Center of Clinical Neuroscience, First Faculty of Medicine, Charles University in Prague, Prague, Czech Republic

P. Ridzoň · R. Rusina · P. Kulišťák · O. Keller
Department of Neurology, Thomayer Teaching Hospital, Prague, Czech Republic

Published online: 15 March 2011

Based on recent studies [5,6], the perspective regarding ALS has evolved to include the broader involvement of central nervous system regions beyond the motor system. Frontal lobe involvement has been detected in ALS, and together with the cognitive impairment of approximately one-third [7] to one-half [5,6] of patients, a link between ALS and frontotemporal lobar degeneration (FTLD) has been made. Following the discovery of the CHMP2B gene mutation in both FTLD and ALS, some authors [8] have suggested that ALS and FTLD may be part of a pathological continuum and the term FTLD-MND has been introduced.

The diagnosis of ALS is primarily clinical and is confirmed by the demonstration of lower motor neuron loss on electromyography (EMG). It often takes months to establish the final clinical diagnosis of ALS and to merely express the suspicion of this fatal disease is a stressful event for the patient and his family, as well as for the physician. Therefore, any technique that supports or opposes the diagnosis of ALS or helps to improve the understanding of its origin and development is highly desirable.

Standard MR imaging of ALS patients has not revealed any unique imaging features apart from cortical atrophy, which is also characteristic to other neurodegenerative diseases. Some MR characteristics, such as increased signal intensity on FLAIR and T2-weighted images in the pyramidal tract (e.g., in the posterior limb of the internal capsule, PLIC) [4,9,10], and T2-hypointensity in the motor cortex (precentral gyrus, "low signal rim") [3,10], have been attributed to ALS, but their diagnostic relevance is equivocal.

Quantitative MR imaging includes volumetric and morphometric techniques, measurements of proton T1 and T2 relaxation times (T1 and T2 relaxometry), and quantitative aspects of water diffusion such as the apparent diffusion coefficient (ADC), mean diffusivity (MD), fractional anisotropy (FA) and proton MR spectroscopy (pMRS). Recent MRI studies [11,12] have shown the potential of quantitative MRI to improve the diagnostic process of ALS.

Thus, we elected to perform a cross-sectional imaging study in order to further evaluate the potential of quantitative MR techniques (voxel-based morphometry (VBM), T2-relaxometry, FA, MD) in the diagnostic process of ALS and to further investigate the extent to which other brain regions are affected in ALS, especially the basal ganglia and non-motor areas.

Materials and methods

Participants

A total of thirty-three subjects fulfilling the El-Escorial criteria [13] for clinically definite ALS were included in the study (18 men, 15 women; mean age 62.0 ± 8.0 SD; disease duration 3–59 months); twenty subjects diagnosed with a limb-onset form of ALS, and thirteen diagnosed with a bulbar-onset form (Table 1). Disease severity was assessed with the ALS Functional Rating Scale (ALS-FRS), producing a score between 0 (worst) and 40 (best) [14]. As the total ALS-FRS score results from a mixture of both bulbar and limb origin impairment, we elected to split the scale to limb and bulbar components (Table 2) to allow the correlation of motor system morphology with clinical signs of motor disability. All subjects were further evaluated for the presence or absence of dementia by a series of neuropsychological tests [15]. Nineteen subjects exhibited a predominantly frontal-type cognitive impairment and behavioural disturbances consistent with FTLD, while twelve subjects were found to be cognitively normal. The results of neuropsychological examination were not available for two subjects.

Thirty healthy, age-matched volunteers (16 men, 14 women; mean age 59.7 ± 10.0 SD) were also included in the study as a control group. All volunteers underwent an examination to exclude neurological disease. The study was approved by the local ethics committee and all participants provided signed informed consent.

MR protocol

Imaging was performed on a Siemens Symphony 1.5-Tesla System (Erlangen, Germany). Structural MR images were acquired using a T1-weighted magnetization-prepared rapid acquisition gradient echo (MP-RAGE) sequence (TR = 2140 ms, TE = 3.93 ms, flip angle = 15 degrees, TI = 1100 ms, 160 axial slices, 1.65 mm slice thickness, x–y resolution 0.9 × 0.9 mm, FOV 238 mm) and a standard TSE T2-weighted sequence covering the entire brain and cerebellum. T2 relaxometry data were acquired by a single slice Carr-Purcell-Meiboom-Gill (CPMG) sequence (32 interecho times of 14.4, 24.8, 37.2 to 396.8 ms; TR = 3000 ms; in-plane resolution 0.89 × 0.89 mm; slice thickness 4 mm) in the region of the basal ganglia. Diffusion data were obtained using a Siemens work in progress (WIP) package with b-factors of 0, 400, and 1100 measured along 30 non-collinear directions (TR = 7900 ms, TE = 101 ms, 70 axial slices, NEX = 2, 1.25 × 1.25 × 2.5 mm).

MR data evaluation

T2-weighted images covering the whole brain as well as raw data for quantitative analysis were evaluated to exclude other significant pathologies. VBM and T2 relaxometry studies were performed in thirty-one subjects (16 men, 15 women; mean age 61.6 ± 8.0 SD). CPMG and VBM sequences were either incomplete or affected by artefacts in two subjects, and were excluded from VBM and T2 analysis. VBM analysis was performed using SPM2 (Wellcome Department

Table 1 Demographic data for ALS patients

Case no.	Age[a]	Sex	FRS	FRS-Limb	FRS-Bulbar	Form	Dementia	Duration[b]	Scan
ALS patient group									
1	66.1	M	31	18	13	Limb	yes	13	R
2	58.5	M	31	15	16	Limb	yes	7	R
3	67.5	M	33	24	9	Bulbar	yes	13	R, D
4	39.5	M	32	18	14	Limb	yes	54	R, D
5	56.6	M	37	21	16	Limb	no	9	R
6	76.2	M	36	24	12	Limb	yes	21	R
7	67.1	F	35	24	11	Bulbar	yes	24	R
8	68.8	M	31	15	16	Limb	yes	13	R
9	61.0	F	24	9	15	Limb	yes	14	R
10	61.9	F	33	20	13	Bulbar	yes	8	R
11	49.2	M	37	21	16	Limb	no	9	R, D
12	65.6	M	38	24	14	Bulbar	yes	4	R
13	68.4	M	36	23	13	Bulbar	yes	7	R, D
14	65.5	F	36	24	12	Bulbar	yes	17	R
15	56.7	M	38	24	14	Bulbar	no	21	R
16	61.1	M	30	15	15	Limb	yes	8	R
17	63.3	F	30	16	14	Limb	yes	12	R
18	58.9	M	29	13	16	Limb	yes	11	R
19	59.0	F	39	24	15	Bulbar	no	8	R
20	52.0	F	34	21	13	Bulbar	no	9	R
21	59.7	F	37	24	13	Bulbar	no	12	R
22	52.9	M	38	22	16	Limb	no	59	R, D
23	66.1	F	32	16	16	Limb	yes	15	R
24	64.8	M	40	24	16	Limb	[c]	5	R
25	70.9	M	37	21	16	Limb	yes	14	R, D
26	47.3	F	32	19	13	Limb	no	8	R
27	53.0	M	38	24	14	Bulbar	no	13	R
28	78.6	F	36	24	12	Bulbar	yes	14	R, D
29	73.3	F	33	24	9	Bulbar	no	25	R, D
30	60.3	M	39	23	16	Limb	no	29	D
31	65.2	F	37	21	16	Limb	yes	25	R, D
32	71.6	M	38	22	16	Limb	no	41	D
33	57.6	M	31	22	9	Limb	[c]	13	R, D

ALS Amyotrophic lateral sclerosis, *Y* years, *FRS* Functional rating scale, *FRS-Limb* Limb component of FRS, *FRS-Bulbar* Bulbar component of FRS, *R* Relaxometry, *D* Dementia
[a] in years; [b] in months; [c] not reported

of Cognitive Neurology, London, UK) in the Matlab 6.5.1 environment (MathWorks, Natick, MA, USA) as previously described [16]. To suppress differences in image quality in comparison with the SPM T1-template, customized whole-brain T1 and tissue probability templates were used. The tissue probability templates were prepared by spatial normalization of the native T1 images to the SPM T1-template using both the patient and healthy volunteer groups, followed by segmentation into grey matter, white matter, and CSF compartments. The images were then blurred using an 8- mm full width at half maximum (FWHM) filter, averaged, and finally processed according to an optimized VBM protocol [16–18]. The original native T1 images were segmented, and the grey matter maps were normalized to the customized grey matter template. The normalization was processed by means of a 12-parameter affine transformation compensated for non-linear shape differences [19,20]. The resulting normalization parameters were used to normalize the native T1 images before final segmentation. Simultaneously, inhomogeneities in the intensity of different grey and white matter regions were corrected for. All spatially normalized, segmented volumes were checked visually to identify any obvious tissue misclassification. Voxel values were then modulated by the Jacobian determinants derived from the normalization

Table 2 ALS-FRS questionnaire divided into limb and bulbar components

Bulbar	Limb
ALS-FRS components	
Speech	Handwriting
Salivation	Cutting food, handling utensils[a]
Swallowing	Dressing and hygiene
Dyspnoea	Turning in bed and adjusting bedclothes
	Walking
	Climbing stairs

ALS Amyotrophic lateral sclerosis, *FRS* Functional rating scale
[a] Patients without gastrostomy

process to provide local intensity correction due to regional volumetric signal expansion/reduction, thus preserving the volumes altered by nonlinear deformation [19]. Modulated grey and white matter maps were subsequently blurred isotropically using a 10- mm FWHM filter.

To verify the negative patient-control *t*-test, SPM8 with DARTEL [21] was used, correcting for age, sex, and intracranial volume. DARTEL is based on a fast diffeomorphic image registration algorithm using a "flow field" that is exponentiated to generate both forward and backward deformations. Segmentation is first performed followed by rigid transformation of the tissue class images, such that they are in as close alignment as possible with the tissue probability maps. Registration is then performed, which involves the simultaneous registration of grey and white matter. The mean of all images is used as an initial template, and the deformation each of the individual images to the template is computed. The template is then re-generated by applying the inverse of the deformation to each image and averaging. This procedure is repeated a number of times, and finally warped versions of the images are stored. The result of this process is better data coregistration in comparison with the optimized VBM approach using SPM2.

T2 relaxometry data were analysed using ImageJ viewer, placing circular regions of interest (ROIs) measuring twenty-one square millimetres in the bilateral frontal white matter (FWM), frontal grey matter (FGM, cingulate gyrus) and PLIC. The basal ganglia (head of caudate nucleus, globus pallidus and putamen) were manually outlined bilaterally using freehand selection (Fig. 1). ROI placement was determined on the highest contrast T2 image, and the average signal data for each echo time were stored [22], generating 32 intensity values for each ROI. We performed nonlinear regression for each ROI using a monoexponential decay model for average signal intensity and interecho time with GraphPad Prism 4 (GraphPad Software Inc., La Jolla, CA, USA). PD values were individually calculated for echo time 0 in each ROI. T2 relaxation rate (R2, R2 = 1/T2) and proton density (PD) signal were statistically analysed using R-project version 2.4.1 [23] as described further.

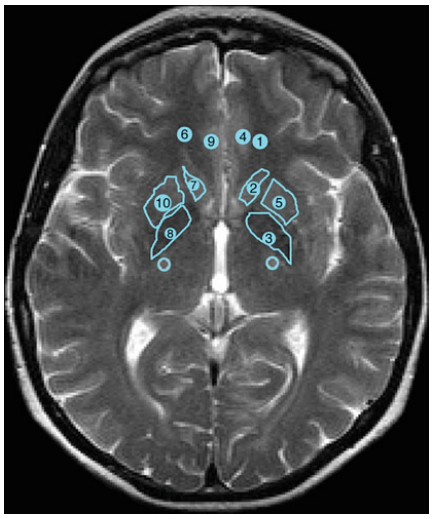


Fig. 1 Outlined regions of interest bilaterally: frontal white matter (1,6), frontal grey matter (4, 9), head of caudate nucleus (2,7), putamen (5,10), globus pallidus (3, 8), and internal capsule (not numbered)

Twelve subjects (9 men, 3 women; mean age 62.97 ± 11.0 SD) and twelve healthy volunteers (9 men, 3 women; mean age 63.22 ± 10.7 SD) were included in the DTI study. Diffusion weighted images were processed off-line in FSL (FMRIB Software Library [24]). After eddy-current and motion correction, brain extraction was performed using BET (brain extraction tool [25]) and DTIFit was then used to calculate the scalar invariants of the tensor. DTIFit generates 3D images at the same matrix size and resolution as the original diffusion images, including a raw T2-signal image with the same distortions as the diffusion weighted images. FA and MD were measured using ImageJ viewer, with circular ROIs measuring twenty-one square millimetres placed by a single observer (J.K.) in both the relaxometry and DTI studies. When analysing the CST region corresponding to the atrophy detected by VBM, ROIs were placed directly on the FA/MD maps (see Results). All other ROIs were placed directly on the T2 maps created by DTIFit, and then projected on the corresponding FA/MD map.

To validate the ROI approach, voxelwise statistical analysis of the FA data was carried out using TBSS (Tract-Based Spatial Statistics, [26]), part of FSL [24]. TBSS projects the FA data of all subjects onto a mean FA tract skeleton derived from the whole data set before applying voxelwise cross-subject statistics. For this analysis, only the upper slab covering the brain from the vertex to mesencephalon was used. The skeleton was built using an FA threshold >0.3. An unpaired

t-test was then used to compare FA values in the patient and control group.

Statistical analysis

VBM data were statistically analysed by group comparison between patients and controls. Linear regression of local grey and white matter values in each voxel and the limb ALS-FRS score was performed. Montreal Neurological Institute (MNI) coordinates were used for the topographical description of results. Results were thresholded at a corrected cluster-level of $P < 0.01$.

The R2 for each ROI was calculated as stated earlier. Normality was tested by the Shapiro test at a P-value threshold of <0.05. Linear regression analysis of R2 over age and ALS-FRS was performed and P-values were calculated. As normality of R2 in patients and controls was not confirmed by the Shapiro test in any region, a single-tailed Wilcoxon two-sample test was used for intergroup comparisons using an a priori hypothesis of decreased R2 in the patient group. Initially a P-value threshold of <0.05 was used, then Bonferonni correction was applied to decrease the alpha value threshold to 0.007. The same methodology was used to evaluate the correlation between FA/MD, age, and clinical scale.

Results

VBM analysis of 31 ALS patients (confounding covariates: age, sex, intracranial volume as reported by SPM2) revealed a statistically significant correlation between decreased white matter intensity in the corona radiata and the limb component of ALS-FRS (Fig. 2a). The region of this correlation ($x = 22, y = -27, z = 51$; $T = 3.48$; $P < 0.01$ cluster-level corrected) is shown in Fig. 2b. This region was further investigated by diffusion analysis in a subgroup of twelve patients, and no correlation between clinical scale/age and FA/MD was observed.

An unpaired t-test corrected for age, sex and brain volume was used for comparison of both white and grey matter intensities. In SPM2 no significant correlations were observed. SPM8 (using DARTEL, $P < 0.05$ family-wise error (FWE) corrected) revealed decreased white matter intensity in the corona radiata bilaterally (Fig. 3). One of the blobs is very near the correlation site in the precentral gyrus (position $x = 28, y = -23, z = 54$; $T = 5.89$; $P < 0.05$ FWE). Using a threshold of $P < 0.0001$ uncorrected, the site of correlation with the limb component of FRS is included in the resulting statistical map.

We detected significantly decreased R2 in the head of the caudate nuclei (left $P < 0.005$, right $P < 0.05$, uncorrected) in ALS patients in comparison with healthy volunteers (Table 3). No dependence of R2 on the duration of disease was observed, with a similar increase in R2 observed across the range of disease duration present in our cross-sectional study. Lower R2 was also present in the deep FWM in ALS patients in comparison with controls (left and right $P < 0.005$). No statistically significant differences in the head of the caudate nuclei or FWM were found between the subgroups of ALS patients with/without cognitive deficit. After Bonferroni correction (corrected alpha value 0.007), the statistically significant differences between patients and controls in the head of the left caudate nucleus and bilateral FWM remained. R2 in the FWM correlated with age in both patients and controls (Fig. 4). Changes of R2 in the FGM did not exceed the statistical threshold.

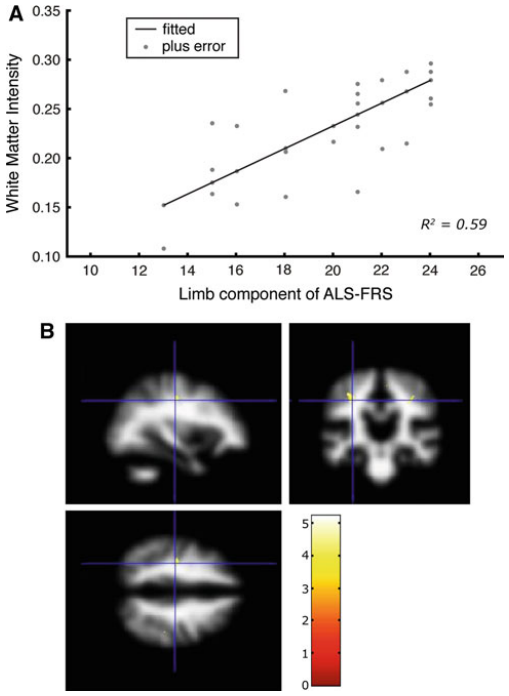


Fig. 2 **a** Voxel-based morphometry (VBM) fitted white matter intensity in correlation with the limb component of the ALS Functional Rating Scale (ALS-FRS). **b** Region of statistically significant correlation between white matter atrophy and the limb component of ALS Functional Rating Scale (ALS-FRS). T-value represented by colour gradient

No statistically significant changes were detected in the PLIC, a region suspected of signal intensity changes in ALS. Changes in R2 in this region did not exceed the statistical threshold nor did any differences in PD (Figs. 5 and 6). T2 hyperintensity in the PLIC was qualitatively appreciated at least unilaterally in all patients and controls (Fig. 7).

Using an ROI-based approach, no correlation between clinical scale/age and FA/MD was observed in the PLIC.

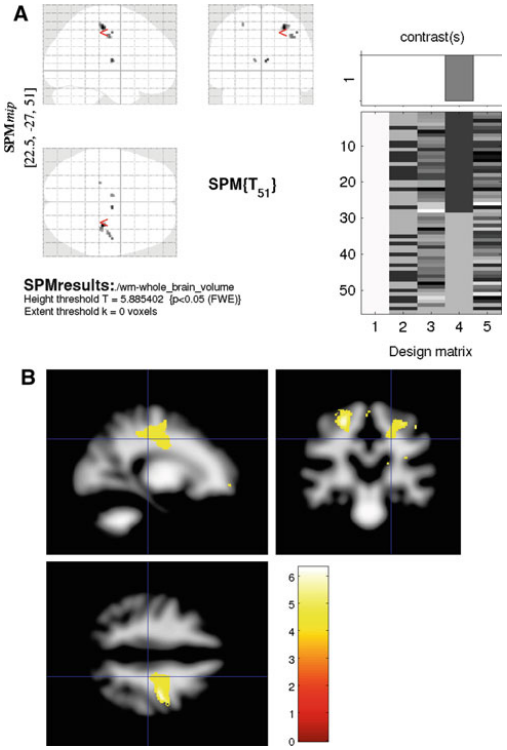


Fig. 3 Voxel-based morphometry using DARTEL (fast diffeomorphic image registration algorithm). Difference between white matter intensity in patients and controls. **a** $P < 0.05$ family-wise error corrected, crosshair indicates correlation site with the limb component of ALS Functional Rating Scale (ALS-FRS) (for details see Fig. 2). **b** $P < 0.0001$ uncorrected

Furthermore, no significant differences in FA were detected between patients and healthy volunteers in the PLIC or FWM. We therefore elected to perform TBSS on the upper slab of diffusion data. No correlation with FRS was found, but a significant difference ($P < 0.05$ corrected) between the patient group and control group was present in the corona radiata (Fig. 5).

Discussion

We found a statistically significant correlation between decreased white matter intensity in the corona radiata and ALS-FRS (Fig. 2) in ALS patients. White matter analysis using DARTEL further revealed lower white matter intensity in ALS patients compared to healthy controls in the same anatomical location. Our findings suggest that as in other neurodegenerative diseases, FWM atrophy may be a surrogate

Table 3 T2 relaxation time in milliseconds for patients and controls

Region	Patients	SD	Controls	SD	*P*-value
ALS relaxometry results					
Head CN, L*	99.7	6.4	95.6	3.4	0.0018
Head CN, R	99.0	7.1	96.6	4.5	0.0232
FWM, L*	88.8	7.8	84.0	4.9	0.0019
FWM, R*	88.2	6.3	84.4	4.5	0.0044
GP, L	72.0	5.4	73.0	5.7	
GP, R	72.2	5.9	73.7	6.6	
CG, L	107.9	8.6	107.1	4.0	
CG, R	105.2	10.6	107.6	5.4	
Putamen, L	88.8	5.9	87.8	5.6	
Putamen, R	88.4	6.9	88.7	6.3	
CST, L	107.3	7.0	106.5	4.4	
CST, R	107.6	6.6	108.0	5.2	

ALS Amyotrophic lateral sclerosis, *SD* Standard deviation, *L* Left, *R* Right, *CN* Caudate Nucleus, *FWM* Frontal white matter, *GP* Globus pallidus, *CG* Cingulate gyrus, *CST* Corticospinal tract
Significant difference as reported by single-tailed Wilcoxon test marked as * $P < 0.05$ after Bonferroni correction

marker of ALS pathology on MRI rather than cortical grey matter involvement. A similar observation was made by Sage et al. [27], where a correlation between the entire ALS-FRS scale and FA in the same region was found. The demographic data of our study and the study of Sage et al. are similar in the number of patients included as well as in the post-processing algorithm.

VBM in ALS has been performed in various studies, often with controversial results. For instance, Mezzapesa et al. [28] described signs of frontotemporal atrophy in ALS patients compared to controls. Kassubek et al. reported similar results [29]. Agosta et al. [30] found lower grey matter density in the superior temporal gyri bilaterally, as well as in the right precentral and left inferior frontal gyri. Chang et al. [31] reported atrophy of the medial frontal gyrus. These studies differ in the number of patients included and the methodology used. This may, at least in part, explain the discrepancies in their results.

The use of an "optimized" VBM protocol as suggested by SPM2 and used by default in SPM5 resulted in false-negative results in the group comparison, contrary to DARTEL implemented in SPM8. These differences are not widely appreciated and should be taken in account when planning or interpreting VBM studies.

To the best of our knowledge, this is the first published account of changes in T2 relaxation rate in the head of caudate nucleus in ALS. Atrophy of the head of the left caudate was found in a subgroup of rapidly progressing ALS patients in another study [32]. These observations support the hypothesis that subcortical grey matter areas may be significantly involved in the pathogenesis of ALS. Significant changes of

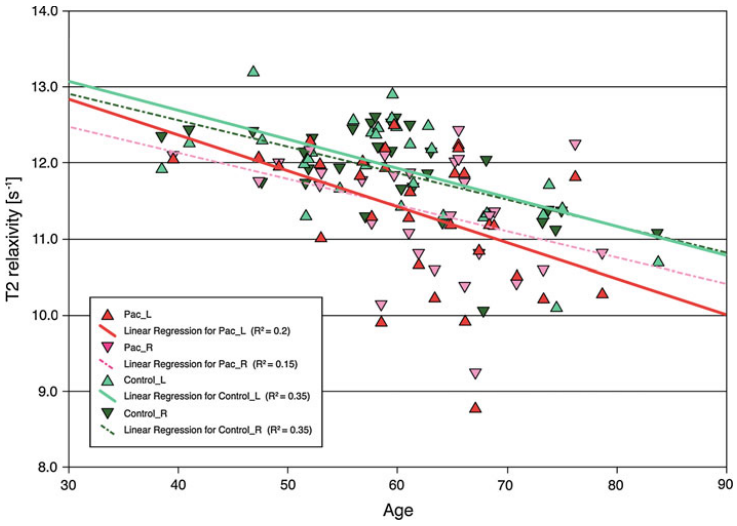


Fig. 4 Correlation between T2 relaxation rate (inverse seconds) and age (years)

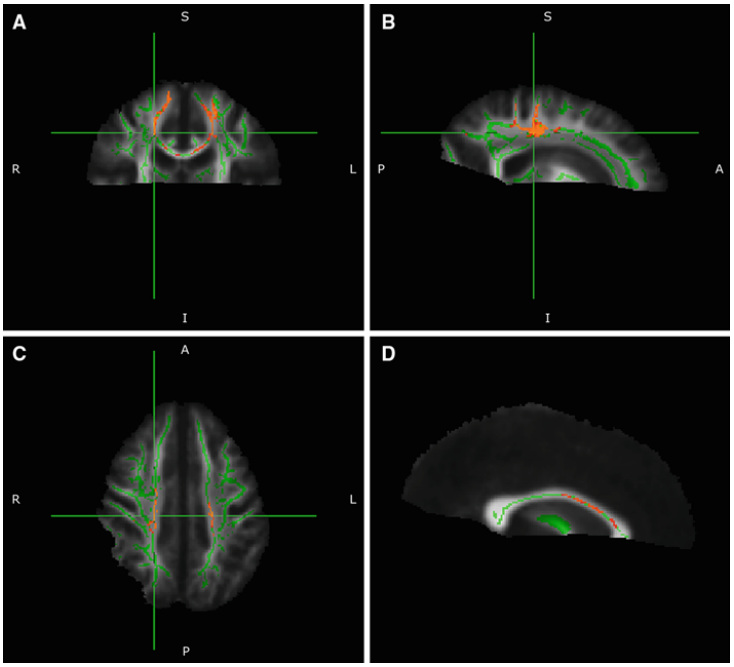


Fig. 5 Tract-based spatial statistics (TBSS) comparison of FA between patients and controls (*t*-test patient < control, $P < 0.05$ corrected, skeleton threshold 0.3)

T2 relaxation rate in this region are of further importance as the caudate nucleus has been used as an internal reference in qualitative and quantitative studies of ALS patients [33–35]. It is interesting to note that the relaxation rate changes detected in this region were not dependent on disease duration. This suggests that decreased R2 is already present

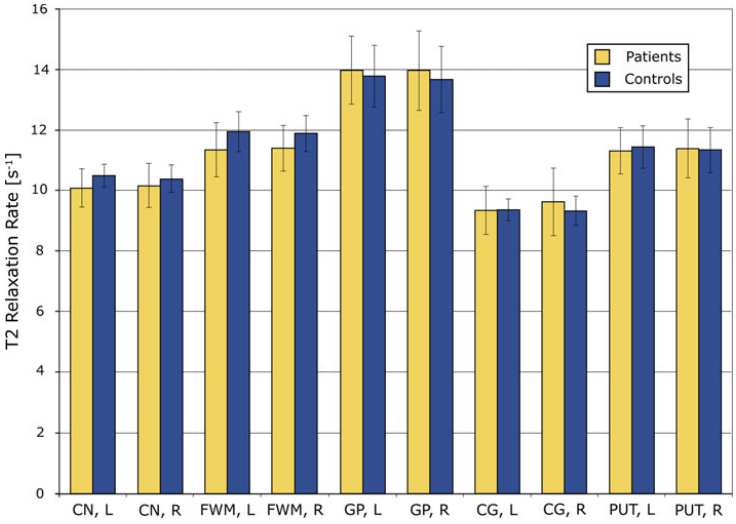


Fig. 6 Comparison of R2 (inverse seconds) between patients and controls in various brain regions. *Bars* represent the mean and *error bars* represent standard deviation. *L* left, *R* right, *CN* head of caudate nucleus, *FWM* frontal white matter, *GP* globus pallidus, *CG* cingulate gyrus, *PUT* putamen

in the earlier stages of the disease and could therefore serve as an early marker of disease activity. Future investigation should focus on quantifying changes in head of the caudate nuclei in a large group patients in the earliest stage of ALS.

Significant changes in the T2 relaxation rate of the caudate nucleus are not surprising when considering that ALS is not limited to the motor system and that relaxometric changes in the basal ganglia have been observed in other neurodegenerative diseases [36]. T2 contrast in the deep grey matter nuclei is predominantly determined by tissue iron in metalloproteins [37,38]. A decrease in the metalloprotein-bound iron ("safe" iron) results in a relative decrease in R2, and more iron in the low molecular forms ("toxic" iron) is available. We propose that the significant T2 relaxation rate changes in the left caudate nucleus observed in our study are related to iron deposition in this region. The observed changes cannot be explained by a change in water content as the proton density did not differ between patients and controls.

We also detected significantly decreased R2 in the bilateral FWM of ALS patients compared to controls. Therefore, we recommend that FWM (as well as head of caudate nuclei, see above) should not be used as an internal reference for the assessment of increased signal intensity in various brain regions in ALS [34,35]. The T2 relaxation rate in the FWM was also found to correlate with age in both patients and controls. Bartzokis et al. demonstrated the age dependence of R2 in the FWM at both 0.5 and 1.5 Tesla field strengths in healthy subjects [39]. A trend towards a steeper decrease of T2 relaxation rate with age in our group of ALS patients was observed, but the difference did not reach the statistical threshold. As age-related changes in the FWM were detected in both patients and controls, this may indicate that decreased R2 in the FWM is age-dependent and that ALS does not influence this correlation significantly.

No statistically significant changes were detected in the PLIC, a region suspected of signal intensity changes in ALS. T2 hyperintensity in this area, labelled as CI3 in histological studies, was observed in nearly all subjects. A confocal microscopy study by Axer [40] revealed that fibres of the corticospinal tract (running superoinferior) cross fibres of the upper thalamic peduncle (running anteroposterior) in this region. In section, a pale area in the most posterior part of internal capsule was more difficult to discern and was less stained by silver than by myelin stain in ALS subjects. This area included thinner axons ($> 0.8\,\mu m$), surrounded by "free space". The posterior aspect of the area was clearly delimited, and the anterior aspect disappeared gradually. In ALS patients, the loss of thin myelinated fibres in this area has been proven [41]. Even though these findings would suggest decreased R2 in this area, our study quantitatively confirms earlier statements [9,10] that the relatively hyperintense signal in this part of the internal capsule is a physiological variant and not disease related as was believed [4,42].

TBSS revealed decreased FA in the area corresponding to the site of atrophy detected by VBM in ALS patients compared to healthy volunteers. These changes were observed in the corona radiata, and no changes were detected in the lower parts of the pyramidal tract. No changes in FA in the corticospinal tract were found using an ROI-based approach. This can be at least partially explained by the process of averaging the data on the skeleton in a voxel-wise manner, which, in contrast to an ROI-based approach, is not influenced by selection size or a priori knowledge. Moreover, an ROI positioned close to fine white fibres is more prone to noise.

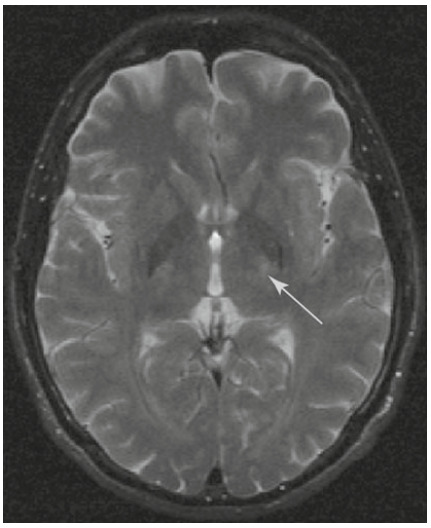


Fig. 7 T2 hyperintensity in the posterior limb of the internal capsule (*arrow*) in a healthy volunteer

No changes in the FWM were detected by means of TBSS or ROI-based methods. Decreased FA in the callosal body is in agreement with current knowledge of fronto-temporal lobar degeneration. Therefore, future research should focus more on fine fibres. Changes in R2 and not FA in this region can be explained by demyelinating changes in the white matter that precede changes in anisotropy. Thus, changes in T2 relaxation rate may precede decreased diffusion anisotropy.

Although a direct comparison of the quantitative MR methods used in our study is not fair as the sequences used differ in slice thickness (ranging from 1.65 to 4 mm) and in-plane resolution, thereby exhibiting various signal-to-noise ratios, our data suggest that a combination of several quantitative methods may be the key to improving the role of MRI in the diagnostic process.

Conclusions

We have demonstrated that pathological changes in ALS are widespread and not limited to only the motor system. R2 in the head of the left caudate and bilateral FWM differs between ALS patients and controls, and these regions cannot be used as an internal reference of "healthy tissue" as in previous studies. A significant correlation was also observed between white matter intensity in the corona radiata and the limb component of ALS-FRS, suggesting that FWM atrophy rather than cortical grey matter involvement may be a surrogate marker of ALS pathology on MRI. TBSS further revealed decreased FA in ALS patients in the corona radiata and callosal body, reflecting pathological changes in the motor pathway and white matter of the frontal and temporal lobes. These findings indicate regions that may be important in the future diagnostic process of ALS.

Although T2 hyperintensity in the PLIC has been considered a marker of ALS, our quantitative analysis of the pyramidal tract passing through the PLIC did not reveal any significant differences between ALS patients and healthy volunteers. This indicates that T2 hyperintensity in the PLIC should no longer be considered a marker of ALS on MRI.

Acknowledgments Supported from grants IGA MZ ČR, NS9654-4/2008, NR8491-3/2007, NR8937-4/2006 and research programs MŠM 0021620849 and MŠM 0021620816.

Open Access This article is distributed under the terms of the Creative Commons Attribution Noncommercial License which permits any noncommercial use, distribution, and reproduction in any medium, provided the original author(s) and source are credited.

References

1. Adams V, Victor M (1993) Principles of neurology. 5th edn. McGraw-Hill Inc, New York
2. Atlas S (2001) Magnetic resonance imaging of the brain and spine. 3rd edn. Lippincott Williams and Wilkins, Philadelphia
3. Oba H, Araki T, Ohtomo K, Monzawa S, Uchiyama G, Koizumi K, Nogata Y, Kachi K, Shiozawa Z, Kobayashi M (1993) Amyotrophic lateral sclerosis: T2 shortening in motor cortex at MR imaging. Radiology 189(3):843–846
4. Hofmann E, Ochs G, Pelzl A, Warmuth-Metz M (1998) The corticospinal tract in amyotrophic lateral sclerosis: an MRI study. Neuroradiology 40(2):71–75
5. Phukan J, Pender NP, Hardiman O (2007) Cognitive impairment in amyotrophic lateral sclerosis. Lancet Neurol 6(11):994–1003
6. Murphy J, Henry R, Lomen-Hoerth C (2007) Establishing subtypes of the continuum of frontal lobe impairment in amyotrophic lateral sclerosis. Arch Neurol 64(3):330–334
7. Rippon GA, Scarmeas N, Gordon PH, Murphy PL, Albert SM, Mitsumoto H, Marder K, Rowland LP, Stern Y (2006) An observational study of cognitive impairment in amyotrophic lateral sclerosis. Arch Neurol 63(3):345–352
8. Lomen-Hoerth C, Murphy J, Langmore S, Kramer JH, Olney RK, Miller B (2003) Are amyotrophic lateral sclerosis patients cognitively normal. Neurology 60(7):1094–1097
9. Goodin DS, Rowley HA, Olney RK (1988) Magnetic resonance imaging in amyotrophic lateral sclerosis. Ann Neurol 23(4):418–420
10. Cheung G, Gawel MJ, Cooper PW, Farb RI, Ang LC, Gawal MJ (1995) Amyotrophic lateral sclerosis: correlation of clinical and MR imaging findings. Radiology 194(1):263–270
11. Sage CA, Van Hecke W, Peeters R, Sijbers J, Robberecht W, Parizel P, Marchal G, Leemans A, Sunaert S (2009) Quantitative diffusion tensor imaging in amyotrophic lateral sclerosis: revisited. Hum Brain Mapp 30(11):3657–3675
12. Cosottini M, Giannelli M, Siciliano G, Lazzarotti G, Michelassi MC, Del Corona A, Bartolozzi C, Murri L (2005) Diffusion-tensor MR imaging of corticospinal tract in amyotrophic lateral sclerosis and progressive muscular atrophy. Radiology 237(1):258–264

13. Brooks BR (1994) El escorial world federation of neurology criteria for the diagnosis of amyotrophic lateral sclerosis, subcommittee on Motor Neuron Diseases/Amyotrophic Lateral Sclerosis of the World Federation of Neurology Research Group on Neuromuscular Diseases and the El Escorial "Clinical limits of amyotrophic lateral sclerosis" workshop contributors. J Neurol Sci 144 (Suppl):96–107
14. The ALS CNTF treatment study (ACTS) phase I-II Study Group (1996) The amyotrophic lateral sclerosis functional rating scale. Assessment of activities of daily living in patients with amyotrophic lateral sclerosis. Arch Neurol 53(2):141–147
15. Rusina R, Ridzoň P, Kulišťák P, Keller O, Bartoš A, Buncová M, Fialová L, Koukolík F, Matěj R (2010) Relationship between ALS and the degree of cognitive impairment, markers of neurodegeneration and predictors for poor outcome. A prospective study. Eur J Neurol 17(1):23–30
16. Jech R, Klempíř J, Vymazal J, Židovská J, Klempířová O, Růžička E, Roth J (2007) Variation of selective gray and white matter atrophy in Huntington's disease. Movement Disorders 22(12):1783–1789
17. Good CD, Johnsrude IS, Ashburner J, Henson RN, Friston KJ, Frackowiak RS (2001) A voxel-based morphometric study of ageing in 465 normal adult human brains. Neuroimage 14(1 Pt 1): 21–36
18. Good CD, Johnsrude IS, Ashburner J, Henson RN, Friston KJ, Frackowiak RS (2001) Cerebral asymmetry and the effects of sex and handedness on brain structure: a voxel-based morphometric analysis of 465 normal adult human brains. Neuroimage 14: 685–700
19. Ashburner J, Friston KJ (2000) Voxel-based morphometry—the methods. Neuroimage 11(6 Pt 1):805–821
20. Ashburner J, Friston KJ (2001) Why voxel-based morphometry should be used. Neuroimage 14:1238–1243
21. Ashburner J (2007) A fast diffeomorphic image registration algorithm. NeuroImage 38(1):95–113
22. Rasband W (1997–2008) ImageJ. http://rsb.info.nih.gov/ij/
23. R Development Core Team (2009) R: a language and environment for statistical computing. R Foundation for Statistical Computing, Vienna, Austria, URL http://www.R-project.org, ISBN 3-900051-07-0
24. Smith SM, Jenkinson M, Woolrich MW, Beckmann CF, Behrens TEJ, Johansen-Berg H, Bannister PR, De Luca M, Drobnjak I, Flitney DE, Niazy RK, Saunders J, Vickers J, Zhang Y, De Stefano N, Brady JM, Matthews PM (2004) Advances in functional and structural MR image analysis and implementation as FSL. Neuroimage 23(1):S208–S219
25. Smith SM (2002) Fast robust automated brain extraction. Hum Brain Mapp 17(3):143–155
26. Smith SM, Jenkinson M, Johansen-Berg H, Rueckert D, Nichols TE, Mackay CE, Watkins KE, Ciccarelli O, Cader MZ, Matthews PM, Behrens TEJ (2006) Tract-based spatial statistics: Voxelwise analysis of multi-subject diffusion data. NeuroImage 31:1487–1505
27. Sage CA, Peeters RR, Görner A, Robberecht W, Sunaert S (2007) Quantitative diffusion tensor imaging in amyotrophic lateral sclerosis. Neuroimage 34(2):486–499
28. Mezzapesa DM, Ceccarelli A, Dicuonzo F, Carella A, De Caro MR, Lopez M, Samarelli V, Livrea P, Simone IL (2007) Whole-brain and regional brain atrophy in amyotrophic lateral sclerosis. AJNR Am J Neuroradiol 28(2):255–259
29. Kassubek J, Unrath A, Huppertz HJ, Lule D, Ethofer T, Sperfeld AD, Ludolph AC (2005) Global brain atrophy and corticospinal tract alterations in ALS, as investigated by voxel-based morphometry of 3-D MRI, Amyotrophic lateral sclerosis and other motor neuron disorders: official publication of the World Federation of Neurology. Res Group Motor Neuron Diseases 6(4):213–220
30. Agosta F, Pagani E, Rocca MA, Caputo D, Perini M, Salvi F, Prelle A, Filippi M (2007) Voxel-based morphometry study of brain volumetry and diffusivity in amyotrophic lateral sclerosis patients with mild disability. Hum Brain Mapp 28(12):1430–1438
31. Chang JL, Lomen-Hoerth C, Murphy J, Henry RG, Kramer JH, Miller BL, Gorno-Tempini ML (2005) A voxel-based morphometry study of patterns of brain atrophy in ALS and ALS/FTLD. Neurology 65(1):75–80
32. Agosta F, Gorno-Tempini ML, Pagani E, Sala S, Caputo D, Perini M, Bartolomei I, Frugulietti ME, Filippi M (2009) Longitudinal assessment of grey matter contraction in amyotrophic lateral sclerosis: a tensor based morphometry study. Amyotroph Lateral Scler 10(3):168–174
33. Ngai S, Tang YM, Du L, Stuckey S (2007) Hyperintensity of the precentral gyral subcortical white matter and hypointensity of the precentral gyrus on fluid-attenuated inversion recovery: variation with age and implications for the diagnosis of amyotrophic lateral sclerosis. AJNR Am J Neuroradiol 28(2):250–254
34. Hecht MJ, Fellner F, Fellner C, Hilz MJ, Heuss D, Neundörfer B (2001) MRI-FLAIR images of the head show corticospinal tract alterations in ALS patients more frequently than T2-, T1- and proton-density-weighted images. J Neurol Sci 186(1–2):37–44
35. Hecht MJ, Fellner F, Fellner C, Hilz MJ, Neundörfer B, Heuss D (2002) Hyperintense and hypointense MRI signals of the precentral gyrus and corticospinal tract in ALS: a follow-up examination including FLAIR images. J Neurol Sci 199(1–2):59–65
36. Bartzokis G, Tishler TA (2000) MRI evaluation of basal ganglia ferritin iron and neurotoxicity in Alzheimer's and Huntingon's disease. Cell Mol Biol 46(4):821–833
37. Vymazal J, Hájek M, Patronas N, Giedd JN, Bulte JW, Baumgarner C, Tran V, Brooks RA (1995) The quantitative relation between T1-weighted and T2-weighted MRI of normal gray matter and iron concentration. J Magn Reson Imaging 5(5):554–560
38. Vymazal J, Brooks RA, Patronas N, Hájek M, Bulte JW, Di Chiro G (1995) Magnetic resonance imaging of brain iron in health and disease. J Neurol Sci 134(Suppl):19–26
39. Bartzokis G, Mintz J, Sultzer D, Marx P, Herzberg JS, Phelan CK, Marder SR (1994) In vivo MR evaluation of age-related increases in brain iron. AJNR Am J Neuroradiol 15(6):1129–1138
40. Axer H, Keyserlingk DG (2000) Mapping of fiber orientation in human internal capsule by means of polarized light and confocal scanning laser microscopy. J Neurosci Methods 94(2):165–175
41. Hirayama K, Tsubaki T, Toyokura Y, Okinaka S (1962) The representation of the pyramidal tract in the internal capsule and basis pedunculi. A study based on three cases of amyotrophic lateral sclerosis. Neurology 12:337–342
42. Yagishita A, Nakano I, Oda M, Hirano A (1994) Location of the corticospinal tract in the internal capsule at MR imaging. Radiology 191(2):455–460

Appendix B

```
#!/bin/bash

#######################################################
## dap - adjust alpha or p-values according       ##
## to D/AP method (Sankoh, Stat Med 1997)         ##
##                                                ##
## A.M. Rulseh - aarulseh@gmail.com               ##
## licensed under a Creative Commons Attribution- ##
## NonCommercial-ShareAlike 3.0 Unported License. ##
#######################################################

NO_ARGS=0
E_OPTERROR=85
usage() {
cat << EOF

Usage: `basename $0` <-a|-p> [options]

Default behavior: D/AP procedure applied to Sidak, return
   either corrected alpha or p-value.

required (one):
 -a : return corrected alpha level
 -p : return corrected p-value
options:
 -b : use bonferroni (sidak by default)
 -n : nominal alpha
 -u : uncorrected p-value
 -t : number of tests (n(n-1)/2)
 -c : mean correlation (0-1) (see also meanCor script)
 -q : quiet, just return the requested value
 -h : display usage and exit

EOF
}

if [ $# -eq "$NO_ARGS" ]; then  # no args?
```

```
37    usage
38    exit $E_OPTERROR
39  fi
40
41  while getopts ":hapqbn:u:t:c:" opts; do
42    case $opts in
43      h) usage; exit 0;;
44      a) ALPHA="yes";;
45      p) PVAL="yes";;
46      q) QUIET="yes";;
47      b) BONF="yes";;
48      n) NOMI="${OPTARG}";;
49      u) UNPV="${OPTARG}";;
50      t) TEST="${OPTARG}";;
51      c) CORR="${OPTARG}";;
52      \?) echo "Invalid option: -$OPTARG"; exit 1;;
53      :) echo "Option -$OPTARG requires an argument."; exit
            1;;
54    esac
55  done
56  shift $(($OPTIND - 1))
57
58  if [[ ! "$ALPHA" && ! "$PVAL" ]]; then
59    usage
60    exit 1
61  elif [[ "$ALPHA" && "$PVAL" ]]; then
62    usage
63    exit 1
64  fi
65
66  if [[ "$ALPHA" && ! "$NOMI" ]]; then
67    echo -n "enter alpha level: "
68    read alpha
69  elif [[ "$ALPHA" && "$NOMI" ]]; then
70    alpha="$NOMI"
71  elif [[ "$PVAL" && ! "$UNPV" ]]; then
72    echo -n "enter uncorrected p-value: "
73    read pval
74  elif [[ "$PVAL" && "$UNPV" ]]; then
75    pval="$UNPV"
76  fi
77
78  if [[ "$TEST" ]]; then
79    tests="$TEST"
80  else
81    echo -n "enter number of tests: "
82    read tests
83  fi
84  if [[ "$CORR" ]]; then
```

```
85    corr="$CORR"
86  else
87    echo -n "enter mean correlation: "
88    read corr
89  fi
90
91  if [[ "$ALPHA" && ! "$BONF" ]]; then
92    aalpha=$(perl -e "{print (1-((1-$(echo
          "$alpha"))**(1/($(echo "$tests")**(1-($(echo
          "$corr"))))))}")
93  elif [[ "$ALPHA" && "$BONF" ]]; then
94    aalpha=$(perl -e "{print ($(echo "$alpha")/($(echo
          "$tests")**(1-($(echo "$corr")))))}")
95  fi
96
97  if [[ "$ALPHA" ]]; then
98    if [[ ! "$QUIET" ]]; then
99      echo "adjusted alpha is: "$aalpha""
100   else
101     echo "$aalpha"
102   fi
103 fi
104
105 if [[ "$PVAL" && ! "$BONF" ]]; then
106   a_p=$(perl -e "{print (1-((1-$(echo "$pval"))**(($(echo
          "$tests")**(1-($(echo "$corr")))))))}")
107 elif [[ "$PVAL" && "$BONF" ]]; then
108   a_p=$(perl -e "{print ($(echo "$pval")*($(echo
          "$tests")**(1-($(echo "$corr")))))}")
109 fi
110
111 if [[ "$PVAL" ]]; then
112   if [[ ! "$QUIET" ]]; then
113     echo "adjusted p-value is: "$a_p""
114   else
115     echo "$a_p"
116   fi
117 fi
```

```
#!/bin/bash

#######################################################
## meanCor - get the mean correlation of off-     ##
## diagonal elements in one or more correlation   ##
## matrices                                       ##
##                                                ##
## A.M. Rulseh - aarulseh@gmail.com               ##
## licensed under a Creative Commons Attribution- ##
## NonCommercial-ShareAlike 3.0 Unported License. ##
#######################################################

usage() {
cat << EOF

Usage: `basename $0` [options] <files>

Default behavior: return mean intra- and inter-correlation
   of one or more matrices. Requires raw, numerical data
   as input, correlation matrices are generated by the
   script.

required:
 <files>: one or more csvs
options:
 -c : comma-separated columns to use (e.g., "1,4,5,6")
 -h : display usage and exit

EOF
}

while getopts ":hc:" opts; do
  case $opts in
    h) usage; exit 0;;
    c) COL="${OPTARG}";;
    \?) echo "Invalid option: -$OPTARG"; exit 1;;
    :) echo "Option -$OPTARG requires an argument."; exit
       1;;
  esac
done
shift $(($OPTIND - 1))
wd="$PWD"

if [[ ! "$@" ]]; then
  usage
  exit 1
fi

if [[ ! "$COL" ]]; then
```

```
46    COL='1:ncol(main)'
47  fi
48
49  count=0
50  for v in "$@"; do
51    R --slave --vanilla --no-save <<-CORR
52      setwd("$wd")
53      main <- read.csv("${v}")
54      attach(main)
55      main_cbind <- cbind(main[,c($(echo "$COL"))])
56      A <- cor(main_cbind)
57      sink("/tmp/tmpR")
58      mean(A[row(A)!=col(A)])
59      sink()
60    CORR
61    if [ $? -gt 0 ]; then
62      echo "R error"
63      exit $?
64    fi
65    corr[$count]=$(cat /tmp/tmpR|cut -d' ' -f2)
66    echo "$v,${corr[$count]}"
67          (( count++ ))
68  done
69
70  count=0
71  sum=0
72  for i in ${corr[@]}; do
73    sum="$(echo "$sum + $i"|bc)"
74    (( count++ ))
75  done
76  echo "avgCor = $(echo "scale=3; $sum / $#"|bc)"
```

Colophon

This dissertation was typeset using LaTeX, originally developed by Leslie Lamport and based on Donald Knuth's TeX, and compiled using the XeTeX typesetting engine, developed by Jonathan Kew. The body text is set in 11 point Arno Pro, designed by Robert Slimbach in the style of book types from the Aldine Press in Venice, and issued by Adobe in 2007. Figures illustrating the results of statistical tests were generated in the R programming environment, using the ggplot2 and pROC packages. All figures were additionally processed using the open source imagemagick command-line tools.